Final Technical Report
submitted to

Department of Energy
National Energy Technology Laboratory

Award No. DEFG2611FE0006947

IN-SITU ACOUSTIC MEASUREMENTS OF TEMPERATURE PROFILE IN EXTREME ENVIRONMENTS

Principal Investigator: Mikhail Skliar
(801) 581-6918, (801) 585-9291 (fax)
mikhail.skliar@utah.edu

Organizational DUNS: 009095365
University of Utah
50 South Central Campus Drive
Salt Lake City, UT 84112

Project Period: 10/01/2011– 3/31/2015

July 30, 2015

Disclaimer

Executive Summary

A gasifier's temperature is the primary characteristic that must be monitored to ensure its performance and the longevity of its refractory. One of the key technological challenges impacting the reliability and economics of coal and biomass gasification is the lack of temperature sensors that are capable of providing accurate, reliable, and long-life performance in an extreme gasification environment.

This research has proposed, demonstrated, and validated a novel approach that uses a noninvasive ultrasound method that provides real-time temperature distribution monitoring across the refractory, especially the hot face temperature of the refractory.

The essential idea of the ultrasound measurements of segmental temperature distribution is to use an ultrasound propagation waveguide across a refractory that has been engineered to contain multiple internal partial reflectors at known locations. When an ultrasound excitation pulse is introduced on the cold side of the refractory, it will be partially reflected from each scatterer in the US propagation path in the refractory wall and returned to the receiver as a train of partial echoes. The temperature in the corresponding segment can be determined based on recorded ultrasonic waveform and experimentally defined relationship between the speed of sound and temperature.

The ultrasound measurement method offers a powerful solution to provide continuous real time temperature monitoring for the occasions that conventional thermal, optical and other sensors are infeasible, such as the impossibility of insertion of temperature sensor, harsh environment, unavailable optical path, and more. Our developed ultrasound system consists of an ultrasound engineered waveguide, ultrasound transducer/receiver, and data acquisition, logging, interpretation, and online display system, which is simple to install on the existing units with minimal modification on the gasifier or use with new units.

This system has been successfully tested with a 100 kW pilot scale down flow oxyfuel combustor, capturing in real time temperature changes during all relevant combustion process changes. The ultrasound measurements have excellent agreement with thermocouple measurements, and appear to be more sensitive to temperature changes before the thermocouples response, which is believed to be the first demonstration of ultrasound measurements segmental temperature distribution across refractories.

List of Figures

2.1 Block diagram of basic components of an ultrasonic measurement system used to generate and detect ultrasonic signals. 21
2.2 The method for ultrasound measurements of segmental temperature distribution (US-MSTD) in solids: An excitation pulse created by an US transducer propagates through the structured containment and encounters n echogenic features along the way, which produce a train of echoes acquired by the receiver. The TOF difference between consecutive echoes is used to estimate the temperature distribution in the corresponding segment of the containment. By sequentially estimating the temperature of each segment, the temperature distribution along the entire path of ultrasound propagation is obtained. 30
2.3 The ΔTOF between echo waveforms at different temperatures is calculated by cross-correlation with a reference waveform acquired at 20°C. 32

3.1 Acoustic measurements of temperature distribution in the refractory. (A) Refractory material contains embedded planes of scattering material. (B) Layered refractory. (C) Refractory insert with geometric changes in the ultrasound propagation path creates partial back scattering. *Left panel* shows an ultrasound excitation pulse and the train of partial echoes produced by internal partial ultrasound reflectors. *Right panel* illustrates an engineered ultrasound waveguide/insert – with internal back scatterers, layers structure, or geometrical changes – embedded into the gasifier refractory. 39
3.2 Ultrasound pulse-echo response for the samples with echogenic features. (A) The pulse-echo ultrasound response of two samples fabricated from the identical cementitious material. One of the samples (Sample B; shown in inserted photograph) contains embedded ultrasound scatterers at the midpoint of ultrasound propagation path, which produces partial reflection (red line). (B) Ultrasound pulse-echo response for the sample with two internal interfaces obtained by sequentially casting three layers of identical formulation and allowing time for a partial cure to occur prior to pouring the next layer. 40

3.3 Ultrasound response of samples with the single internal interface obtained by allowing the first cementitious layer to cure for 1 hour. Inserts schematically depict the locations producing the acquired echoes: The first echo is the partial internal reflection from the interface between the two layers; the second echo is from the distal end of the sample. Round-trip echoes from partial internal reflection and the distal end were also seen. 42
3.4 Ultrasound response of samples obtained by sequential casting of two 1" layers of cement. The single internal interface between the layers is obtained by allowing the first cementitious layer to cure for 45 minutes (A) or 15 minutes (B). Inserts schematically depict the locations creating the acquired echoes. In (A), both, the partial internal reflections and the reflection from the distal end of the sample are clearly visible. In (B), the reflection from the interface is not well defined and varies with the change in the transducer position relative to the centerline of the sample. 43
3.5 Ultrasound response of samples with two internal interfaces obtained by allowing the first cementitious layer to cure for 15 minutes, 1 day for the second layer, and at least 1 day for the final third layer. Water-cement ratio was equal to 0.36. Inserts schematically depict the locations at which the acquired echoes were created. Three echoes are clearly visible, of which the first two are from the internal interfaces created by multiple layers cast sequentially. 44
3.6 Ultrasound response for samples with the two internal interfaces obtained by allowing the first cementitious layer to cure for 45 minutes (A) or 1 hour (B). For both samples, the second and third layers were cured for al least 1 day. Water-cement ratio was equal to 0.36. Echoes from the second interface and the end of the sample are clearly visible. However, the signal from the first interface is rather complex, likely indicating entrapment of air at the interface or other unidentified features. 45
3.7 Ultrasound response for samples with two internal interfaces obtained by allowing the two initial cementitious layers to cure for 1 day each. The last layer was cured for at least 1 day. Water-cement ratio was equal to 0.44. Echoes from both interfaces are well defined, with relatively high SNR. . . . 47
3.8 Ultrasound response for a sample with a single internal interface obtained by allowing the first cementitious layer to cure for 1 (A) or 2 days (B). Water-cement ratio equal to 0.44 was used. Echoes from the interface and the end of the sample are well defined, with a relatively high SNR. 48
3.9 Ultrasound waveforms obtained with samples of different formulations. Panel (A) shows the results obtained with Portland Fortified cement. The results for the Rapid Set® cement sample is shown in (B). In both cases, the echoes from internal interfaces are well defined and have a relatively high SNR. 49

3.10 Setup used during experiments with the waveguide structured by four layers, L1...L4. During calibration experiments, layers L2–L4 were maintained at a uniform temperature controlled by the side heater. Nonuniform temperature distribution was created by using the base heater only. 52
3.11 (A) Typical waveforms of ultrasound echoes created by the interface between different layers Li of the cementitious sample (insert) and the sample-air interface at its distal end. The measurements were acquired at the reference temperature of 20 °C. (B) Envelopes of echo waveforms collected at different temperatures. 53
3.12 Ultrasound waveforms acquired at different temperatures illustrate the change in the TOF and the corresponding SOS with temperature. 54
3.13 Comparison of the estimated ΔTOF (offsets) at different temperatures obtained by cross-correlating the waveforms (panel (A)) or envelopes of the waveforms (panel (B)). 56
3.14 Calibration results for the speed of sound as a function of temperature. The SOS in different segments (layers of the waveguide) was calculated from the measurements of the change in the time of flight of the four echoes produced by the structured waveguide, relative to their TOF at the reference temperature $T_{ref} = 20\,^{\circ}\mathrm{C}$. The shown linear fit $c = f(T)$ is based on the data for all layers. The shaded area gives the 95% confidence interval for the obtained linear fit. 60
3.15 The speed of sound as the function of temperature for six cementitious samples, varying in composition and curing time, shows an approximately linear relationship in the investigated range of temperatures. 61
3.16 (A) Estimated temperature distributions based on piecewise constant and piecewise linear parameterizations are compared with the measurements of the surface temperature obtained with thermocouples attached in the middle of each segment. (B) The parametrization based on two-dimensional thermal conductivity model can be used to estimate the temperature distribution along the centerline and the surface of the waveguide. 63
3.17 (A) and (B) show thermal images of the proximal and distal ends of the waveguide. Temperature distribution in the waveguide predicted by the two-dimensional heat conduction model is shown in (C). 65

4.1 The ultrasound waveforms acquired from 4-inch and 5-inch alumina samples. Echo signals are seen at approximately 10 and 12 microseconds. 69
4.2 The ultrasound waveform for 1"×12" alumina rod shows multiple echoes produced by the reflections from the distal end of the waveguide. The data were obtained with the transducer having a 1 MHz central frequency. 70
4.3 Schematic depiction of multiple modes responsible for an observed multiple echoes from the distal end of the waveguide. 70

4.4 Three 3/32-inch holes were drilled into the precast alumina rod at 2, 4, and 6 inches away from its distal end. 71
4.5 The ultrasound echo waveforms obtained with transducers of different central frequencies. 72
4.6 Laboratory test system in the arraignment using during the calibration experiments conducted to establish the relationship between the speed of sound and the temperature. 73
4.7 (A) Typical waveforms of ultrasound echoes created by small holes at the locations z_i, which define different segments of the alumina waveguide (insert). The last echo is created by the reflection from the distal alumina-air interface. The shown waveforms were acquired at the reference temperature equal to 20 °C. (B) Envelopes of echo waveforms acquired at different temperatures. 75
4.8 The relationship between the SOS and temperature for all six repeat experiments is shown in (A). The time of flight measurements used in the calculation of the SOS followed the envelope cross-correlation methods. The results in (B) are shown with and without corrections for the thermal expansion of alumina waveguide. The error bars in all plots indicate the 95% confidence interval for each data point. 77
4.9 (A) Young's modulus as a function of temperature calculated based on the long rod model and its comparison with the data of Gault et al. study [1]. The results for sintered alumina [2,3] are shown in (B). 79
4.10 Young's modulus of elasticity normalized by its room temperature value E_0 as a function of the temperature is compared with the results reported in [2,3]. 80
4.11 The equal percentage and polynomial fit of the SOS as a function of temperature. The coefficient of determination of the equal percentage fit is $R^2 = 0.999$. The error bars indicate 95% confidence interval. 81
4.12 The experimental setup to establish nonuniform temperature distribution along alumina waveguide. 82
4.13 Echo waveforms used in the calculation of TOF though i-th segment used to estimate the segmental temperature distribution. 83
4.14 The estimated temperature distributions at steady state. Panels (a) and (b) show the results when the setpoint of the furnace (red dots) was maintained at either 500 °C or 1,000 °C, respectively. The temperature distributions in the three segments of the waveguide were obtained using piecewise-constant and piecewise-linear parameterizations. For comparison, thermocouples were used to measure the surface temperatures (black dots) in the middle of the three segments and at the distal end of the waveguide. 85

4.15 Real-time measurements of the temperature distribution in the sample during transient changes in the furnace setpoint. Thermocouple measurements were logged manually after steady state was reached after each change in the setpoint. 87

5.1 The difference in the TOF between echoes produced by an internal interface of a two-layer cementitious sample and its distal end obtained by threshold crossing (A), peak matching (B), cross-correlation (C), and envelope cross-correlation of the waveforms (D). 90
5.2 The ultrasound excitation pulse applied to aluminum samples produces multiple round-trip echoes. 92
5.3 The shift needed to maximize the cross-correlation between the first and second echoes (blue trace) of the acquired response to the ultrasound excitation equal to the ultrasound time of flight through the aluminum sample. Green line shows the original waveform shifted by the calculated TOF. . . . 93
5.4 The time of the electrical trigger must be corrected to find the time when the ultrasound waveform starts its propagation through the sample. 94
5.5 (I) Echo waveforms produced by four small echogenic features PR1...PR4 obtained by drilling small holes along the length of the alumina waveguide and the reflection from its distal end, DE. Insert (A) shows the photograph of the waveguide; its discoloration was caused by insertion into a pilot scale oxy-fuel combustor (data not included). (II) The envelopes of waveforms in panel (I). (III) Echo waveforms in the cementitious sample were created by an internal interface between consecutively cast layers and the distal end. The envelopes of the two waveforms are shown as black and red lines. . . . 100
5.6 (I) The original echo waveform, shown in blue, was produced by PR3 echogenic feature of the ceramic waveguide; its envelope is shown in A. The application of the anisotropic diffusion filter for 100, 500, 1000, and 1500 iterations produced filtered envelopes respectively shown as B, C, D, and E. Maximum values of filtered envelopes are marked with red triangles. (II) Two echoes, shown as blue traces, were produced by the PR1 feature. They were acquired at the same conditions but different times. Their envelopes show variability in the position of the maximum value indicated by green triangles. After applying 3000 iterations of anisotropic diffusion algorithm, the filtered envelopes of both waveforms are shown in the middle of the panel. Red arrows show that the peak values coincide after filtering. 102
5.7 Real-time measurements of the temperature distribution in the sample during transient changes in the furnace setpoint were obtained before (top plot) and after applying the anisotropic diffusion filter. After the envelopes of the waveforms were filtered, the excursion in the estimated temperature away from the setpoint trajectory were eliminated. 105

6.1 Pilot scale down-fired oxy-fuel combustor. 107
6.2 Flame imaged through a quartz window during NG (left) and coal combustion. 108
6.3 Schematic depiction of US-MSTD system designed and installed during the OFC pilot testing. Alumina waveguide was engineered with partial ultrasound reflectors located along the 1×12-inch alumina rod. Their locations, marked as z_1, z_2, z_3 and z_4, were 6, 4, 2 and 1 inches away from the hot distal end (DE) of the rod. The data acquisition and interpretation systems provided real time measurements and display of the temperature distribution across the waveguide and the comparison with the independent thermocouple measurements. 109
6.4 Port-mounted waveguide retention system. 110
6.5 (A) Waveguide was mounted in P3 port. (B) Engineered alumina waveguide is shown mounted in the flange fixture. (C) Thermal insulation was wrapped around the waveguide. (D) The fixture is being inserted into P3 port. (E) The mounted waveguide is shown with the attached ultrasound transducer connected to the BNC cable leading to the US data acquisition system. Thermocouples are shown connected to DAQ. (F) Radiation shield is now installed. (G) Distal end of the transducer is shown to be mounted flush with the refractory surface. The picture was taken prior to the experiments with a camera inserted inside the ignition zone. (H) The system during the experiments. (I) Computer screen shows the ultrasound waveforms acquired in real time and the corresponding temperatures obtained with ultrasound measurements. (J) Components of the ultrasound data acquisition system. (K) The waveguide removed from the port at the completion of the experiments. (L) The waveguide after removing thermal insulation. Note thermocouple wires inserted into holes drilled to provide US echoes. 111
6.6 Ultrasound measurements of segmental temperature distribution across the refractory of the OFC under piecewise constant parametrization. The ultrasound results are compared with the pointwise temperature measurements provided by the thermocouples. Thermocouple measurements were not logged for the first hour of the experiment. 114
6.7 Ultrasound measurements of segmental temperature during stable natural gas combustion under piecewise constant parametrization. Thermocouple measurements are shown for comparison. 115
6.8 Temperature distribution across the refractory during stable natural gas combustion obtained based on piecewise linear parametrization. 116

6.9 Temperature evolution at the distal end of the waveguide and feature locations z_i during stable natural gas combustion. Ultrasound results were obtained using piecewise constant and piecewise linear parametrization of the segmental temperature. The thermocouple measurements at the location of echogenic features are provided for comparison and show consistency with the ultrasound measurements. 117
6.10 Ultrasound measurements of segmental temperature during transition from natural gas to coal combustion under piecewise constant parametrization. Thermocouple measurements are shown for comparison. Ultrasound and thermocouple measurements are in agrement, but the ultrasound response for temperature changes is faster. 118
6.11 Temperature distribution across the refractory during transition from natural gas to coal combustion obtained based on piecewise linear parametrization. 119
6.12 Temperature evolution at the distal end of the waveguide and feature locations z_i during transition from natural gas to coal combustion. Ultrasound results were obtained using piecewise constant and piecewise linear parametrization of the segmental temperature. The thermocouple measurements at the location of echogenic features are provided for comparison and show consistency with the ultrasound measurements. 120
6.13 Ultrasound measurements of segmental temperature during the reduction in the feed rate of coal under piecewise constant parametrization. Thermocouple measurements are shown for comparison and indicate the same trend in temperature changes. 121
6.14 Temperature distribution across the refractory during the reduction in the feed rate of coal obtained based on piecewise linear parametrization. 121
6.15 Temperature evolution at the distal end of the waveguide and feature locations z_i during the reduction in the feed rate of coal. Ultrasound results were obtained using piecewise constant and piecewise linear parametrization of the segmental temperature. The thermocouple measurements at the location of echogenic features are provided for comparison and show consistency with the ultrasound measurements. 122
6.16 Ultrasound measurements of segmental temperature during stable coal combustion under piecewise constant parametrization. Thermocouple measurements are shown for comparison and indicate the same trend in temperature changes. 123
6.17 Temperature distribution across the refractory during stable coal combustion obtained based on piecewise linear parametrization. 123

6.18 Temperature evolution at the distal end of the waveguide and feature locations z_i during stable coal combustion. Ultrasound results were obtained using piecewise constant and piecewise linear parametrization of the segmental temperature. The thermocouple measurements at the location of echogenic features are provided for comparison and show consistency with the ultrasound measurements. 125
6.19 Temperature evolution at the distal end of the waveguide under different operating conditions. The thermocouple measurements were obtained at the different elevation inside the flame zone, in Port P2. 126
6.20 Alumina grain size distribution in the waveguide material as a function of thermal treatment is images with over 13000x magnification. (A) shows grains prior to heat treatment; the sample imaged in (B) was subjected to short term treatment; the effect of the long term exposure during pilot scale testing on the grain sizes is shown in (C). 128

List of Tables

3.1 Cementitious samples used during SOS vs. temperature testing 61

5.1 Ultrasound propagation delay relative to trigger obtained with different materials 95
5.2 Timing errors in ceramic waveguide 103
5.3 Timing errors in cementitious waveguide 104

Acronyms

The National Energy Technology Laboratory (NETL)
One-dimensional (1D)
Two-Dimensional (2D)
Three-Dimensional (3D)
Thermocouple (TC)
Resistance temperature device (RTD)
Coefficient of thermal expansion (CTE)
Fiber bragg grating (FBG)
Ultrasound (US)
Nondestructive testing (NDT)
Speed of sound (SOS)
Time of flight (TOF)
Ultrasound measurements of segmental temperature distribution (US-MSTD)
Internal diameter (I.D.)
Signal-to-noise ratio (SNR)
Oxyfuel combustor (OFC)
Partial stabilized zirconia (PSZ)
Tetragonal zirconia polycrystal (TZP)
Yttria stabilized zirconia polycrystal (Y-TZP)
Surface acoustic wave (SAW)

Contents

1 Goals and Accomplishments **14**
1.1 Motivation . . . 14
1.1.1 The challenge of gasification . . . 15
1.1.2 Current Temperature Measurement Techniques . . . 16
1.2 Organization of the Report . . . 19

2 Physical Basis of the Method **20**
2.1 Background . . . 20
2.1.1 Basic Ultrasound Instrumentation . . . 21
2.1.2 Speed of Ultrasound Propagation . . . 21
2.1.3 Impedance and Attenuation . . . 23
2.1.4 Scattering . . . 23
2.1.5 Reflections and Transmissions . . . 23
2.2 Physical Basis of the US-MSTD Method . . . 24
2.3 Method . . . 28
2.3.1 Structure US Propagation Path . . . 29
2.3.2 Acquisition of Echo Waveforms . . . 30
2.3.3 Signal Processing . . . 31
2.3.4 Temperature Dependence of the Ultrasound TOF . . . 33
2.3.5 Estimation of Temperature Distribution . . . 33
2.3.6 Estimation of Heat Fluxes . . . 36
2.3.7 Segmental characterization of elastic properties . . . 36

3 Low Temperature Laboratory Experiments **38**
3.1 Cementitious Waveguide Partial Reflector Structures . . . 38
3.1.1 High Water-Cement Ratio Samples and Varying Curing Times . . . 41
3.1.2 Low Water-Cement Ratio Samples and Varying Curing Times . . . 44
3.1.3 Medium Water-Cement Ratio Sample with Long Curing Time . . . 46
3.1.4 Summary of Partial Internal Reflection Structures . . . 46
3.2 Measurements of the temperature distribution in a cementitious sample . . . 51

3.2.1 Structured Cementitious Waveguide . . . 51
3.2.2 Temperature Dependance of the Speed of Sound . . . 51
3.2.3 Signal Processing . . . 55
3.3 Results . . . 58
3.3.1 Calibration: SOS as a function of Temperature . . . 58
3.3.2 Estimated temperature distribution . . . 59
3.3.3 Parametrization with 2D Thermal Conductivity Model . . . 64

4 High Temperature Laboratory Experiments 67
4.1 Alumina Refractories . . . 67
4.1.1 Castable Alumina . . . 67
4.1.2 Machinable Alumina . . . 68
4.2 Experiments . . . 70
4.2.1 Introduction of Echogenic Features . . . 70
4.2.2 Frequency selection . . . 71
4.2.3 Experimental Setup . . . 71
4.3 Results . . . 74
4.3.1 Signal Processing . . . 74
4.3.2 SOS as a Function of Temperature . . . 76
4.3.3 Elastic Modulus . . . 78
4.3.4 Calibration Curve in Normalized Form . . . 79
4.3.5 Estimation of Nonuniform Temperature Distribution . . . 81
4.3.6 Estimation of Nonuniform Temperature Distribution . . . 82
4.3.7 Real Time Measurements of Temporal Changes in Temperature Distribution . . . 86
4.4 Laboratory Tests of Refractory Degradation . . . 86

5 Anisotropic diffusion filter for robust timing of ultrasound echoes 89
5.1 Time of Flight Measurements . . . 89
5.1.1 Cross-correlation of Waveform . . . 89
5.1.2 Zero Time Reference . . . 91
5.1.3 Cross-correlation of Envelopes of Ultrasound Waveforms . . . 95
5.2 Anisotropic Diffusion Filter . . . 96
5.3 Experiments and Results . . . 99

6 Pilot Scale Testing 106
6.1 Pilot Scale Oxy-fuel Combustor . . . 106
6.2 Components of the US-MSTD System: Design and Implementation . . . 109
6.3 Experimental Conditions . . . 112
6.4 Experiments and Results . . . 113
6.4.1 Natural Gas Preheating . . . 113

6.4.2 Steady Natural Gas Combustion . . . 114
6.4.3 Transition from Natural Gas to Coal . . . 118
6.4.4 Response to Decreased Feed Rate of Coal . . . 119
6.4.5 Stable Coal Combustion . . . 119
6.4.6 Surface Temperature of the Refractory . . . 124
6.5 Discussion . . . 124
6.5.1 Couplant . . . 124
6.5.2 Alumina Refractory Waveguide . . . 127

7 Conclusion **129**

8 Products **130**
8.1 Publications . . . 130
8.2 Technology . . . 131

Bibliography **131**

Chapter 1

Goals and Accomplishments

The main objective of this project is to develop and validate ultrasound (US) techniques, in-situ sensors, and measurement systems for non-invasive or minimally invasive measurements of temperature distribution in solids, with particular emphasis on measurements in extreme environments. We are specifically interested in temperature measurement across refractories of combustion and gasification processes and containments of other energy conversion processes, which are often characterized by extreme operation conditions, including high temperatures, pressures, mechanical abrasion, chemical aggressiveness, and radiation exposure. This report describes the successful development of such techniques and their experimental testing in the laboratory and during pilot-scale operation of the coal-fired oxy-fuel combustor.

1.1 Motivation

Non-invasive or minimally invasive alternatives to the traditional methods of temperature measurements are particularly useful when: a) insertion of temperature probes is undesirable, difficult, or impossible; b) extreme environments affect longevity of conventional sensors, as is the case for many energy conversion processes; and c) when optical line-of-sight measurements are not practical because the medium is opaque or optically dissipative. A further advantage of ultrasound measurement is their sensitivity to the temperature distribution, as opposed to point-wise temperature measurements provided by conventional techniques. The US temperature measurements can be implemented in all traditional transducer-receiver arrangements. The pulse-echo mode, emphasized in this project, is particularly appealing because in this arrangement a single device – an US transducer/receiver – is ultrasonically coupled to the proximal end of the waveguide, which may be located outside an aggressive environment, at a stand-off location.

To illustrate the need for the developed technology, we take a closer look at coal and biomass gasification as an example of an energy conversion process that severely

challenges the utilization traditional temperature senors.

1.1.1 The challenge of gasification

Gasification involves the breakdown of carbon rich feedstock in a hot, reactive environment to produce synthesis gas, or syngas, which is rich in hydrogen (H_2) and carbon monoxide (CO). The obtained syngas can then be used as an alternative feedstock for many chemical processes, or in power generation. When used in power generation, gasification plants tend to use less makeup water, produce less solid waste, and airborne pollutants than typical coal combustion-based plants, and may be designed and run in carbon neutral or carbon capture-ready implementations [4]. Since 1970s, gasification process has been adopted to use a variety of carbon-based feedstocks, such as coals, low-cost petroleum coke, biomass, and agriculture (solid) waste [5].

Gasifiers operating at temperatures above the melting point of inorganic components (ash) in the feed offer several advantages, including high production of syngas, lower steam consumption, and more easily disposable and usable solid waste. Gasifiers of this type, known as slagging gasifiers [6], include (1) Lurgi Dry-Ash and British Gas/Lurgi fixed-bed gasifiers; (2) fluidized bed systems, such as KBR Transport, High Temperature Winkler, and ICC/CAS AFB gasifiers; and (3) entrained-flow gasifiers such as GE Energy (formerly Chevron Texaco), Shell, and CB& I E-Gas^{TM} gasifiers. These high-efficiency gasification processes operate at high temperatures and pressures, aggressive chemical environment, and mechanical abrasion caused by flowing slag. Typical operating conditions include temperatures of 1300 °C (slurry-fed gasifiers) or 1500–1800 °C (dry-fed gasifiers) and pressure of 0.15 to 2.45 MPa for fixed bed gasifier, 900–1200 °C and up to 2.94 MPa for fluidized bed, and 1200–1600 °C and 2–8 MPa for entrained flow gasifiers [7]. Together, these conditions create an extraordinarily severe environment for the structural components of the slagging gasification system [8] and largely rules out continuous use of conventional insertion sensors.

Service life of the refractory in slagging gasifiers has a significant impact on the cost of the operation. Current refractories often last only 4–18 months, which is significantly lower than the desired service life of at leat 3 years [9]. The replacement cost of the refractory lining is high, both in terms of the material and labor costs and lost production time (usually 2–3 weeks). Current degradation monitoring of slagging gasifiers is not a real time system, but is rather based on diagnostic methodologies that primarily use microstructural analysis of damaged refractory bricks extracted after the shutdown of the plant. The lack of the real-time measurements of the operating conditions inside a reactive zone impedes our ability to operate gasification processes at the conditions that insure efficient conversion while minimizing refractory degradation. Early detection of damage to the refractory walls is necessary to prevent unscheduled shutdown of a gasification plant. Real time diagnosis tool with capabilities to generate early warnings is critical in extending the refractories service life.

The pivotal idea for damage detection and prediction to the refractory wall is to monitor local temperature anomalies which contribute to temperature gradients and thermal stresses in the refractory. Temperature variations across different refractory cross-sections can be used to assess the thickness of the refractory and the slag flow on its hot surface. The refractory temperature profile could be used to calculate heat fluxes and thermal losses, which also depend on the integrity and thickness of the refectory [10]. Furthermore, mechanical properties of the refractories – including compressive strength, tensile strength, Young's modulus and creep rate – are primarily temperature and load history dependent. As the critical temperature is reached, refractories lose their strength. This critical temperature depends on the melting point and refractoriness of the materials. The strength loss results in excessive deformation and the loss of load-carrying capability with the consequent loss in integrity of the lining system [8]. Therefore, temperature distribution across the refractory wall is a key input for 2D and 3D stress analysis of gasifier support structures, such as the reactor shell and the anchors. Overall, together with the need for an improved refractory materials that can withstand harsh environments [11,12], the lack of real-time sensor-based information indicative of refractory degradation is one of the major technological challenges in gasification.

1.1.2 Current Temperature Measurement Techniques

Direct Measurements

Thermocouples (TC) remain the most common temperature sensors used to characterize gasification processes. Platinum-rhodium TCs are common as they can provide measurements of extreme high temperatures. However, when exposed to a harsh operating environment inside the slagging gasifier, such thermocouples often fail within hours of insertion, leaving operators with no real-time means for temperature measurements. The conventional approach to harden the thermocouples is to utilize ceramic sheathing and improved filler materials [9]. However, the heavy sheathing makes such devices less sensitive to dynamic changes in temperatures and the currently available sheathing materials are still susceptible to slag penetration and erosion damage. As a result, the service life of the most hardened TCs is typically less than 120 days inside the gasifier. Failure rates are often up to 50% within 15 days, and 75% within 30 days. This is especially true for entrained-flow slagging gasifiers since even the most hardened sensors are unlikely to survive for more than 1 or 2 months as the inner surface of the refractory wall degrades and recesses, exposing sensors directly to the corrosive slagging environment. Once exposed to the environment that exceeds material limits, TCs rapidly disintegrate [13]. Even within performance limits, thermal variations may lead to failure due to mismatch in the coefficient of thermal expansion of thermocouple and sheathing materials [14]. Our interviews with U.S. operators of industrial gasification units indicate that they are willing to trade-off the accuracy of temperature measurements for a longer service life of insertion

thermocouples. One consequence of these priorities is the practice of recessed installation of thermocouples inside the measurement ports. By placing the tip of the thermocouple withdrawn into the refractory wall, the sensor is better protected from slag or erosion damage [5] but measures the temperatures that may be 10's or even 100's degrees lower than the temperature on the surface of the refractory.

Indirect Measurements

Secondary measurements that are relatively easy to obtain – such as temperatures, pressures and compositions of streams into and out of a gasifier – can be used in conjunction with empirical or theoretical models and correlations to estimate inaccessible operating parameters inside the reaction zone. The sensors used for such inferential measurement are usually located up- and downstream from the gasifier and thus away from its extreme environment. Texaco Inc. [15] has developed a method to monitor the weight of the slag and infer the process conditions (including the temperature) and use this information in automatical control. The temperature measurements of the cooling water was used in [16–18] to estimate the heat flux away from the reaction zone. An attempt to correlate a large number of routinely measured process variables to the composition of the produced syngas was reported by Guo et al. [19]. Higman and van der Burgt [5] concluded that the temperature of a dry slurry feed gasifier can be monitored by measuring the concentration of CH_4 or CO_2 in the product gas. A similar conclusion was reached in the computational study of Sarigul [20], which showed close correlation between CH_4 concentration and the adiabatic flame temperature of the gasifier. The same approach was used to estimate gasification temperature during the Tampa Electric Integrated Gasification Combined-Cycle Demonstration Project [21,22] and is believed to be in common use by at least some operators of gasification units in the United States who, in our interviews, reported temperatures in ppm of methane.

Despite limited current use, the inferential sensors remain a promising approach in gasification and, more broadly, extreme environment applications. However, two fundamental limitations of inferential measurements must be taken into account. First, the quality of inferences critically depends on modeling errors and uncertainties, and unmodeled changes to the process itself (e.g., due to ware and aging), its feed, and unknown process disturbances. Second, the measurement accuracy, sensitivity, and response time of inferential measurement compare poorly with the corresponding characteristics of the direct measurements. Therefore, the direct measurements in gasification will continue to be desirable despite a long development time, high development cost, and technical challenges that must be overcome.

Noninvasive Measurements

Noninvasive measurements do not require the direct or partial insertion of a fragile sensing element into the harsh environment. The most widely used techniques in this category are optical measurements, which can be used to measure combustion temperature and gas composition [23]. Optic sensors may be based on the measurements of different properties, including optical reflection, scattering, interference, absorption, fluorescence, and thermal radiation [24]. The methods for optical measurements of temperature in an extreme environment has been reviewed in [25] and include optical fiber Bragg grating (FBG) sensors, optical resonator cavity measurements, optical sapphire fiber-based fluorescence sensors, optical single crystal sapphire-based sensor, among others. Photosensitive FBG sensor and optical resonator cavity sensor, such as Fabry-Pérot cavity-based sensor, use silica fibers which do not survive temperatures over 1000 °C. When FBG sensor was used at temperatures close to or above 1000 °C for hundreds of hours in air, silica single mode fibers lost their mechanical strength and became extremely brittle [26], which made their subsequent handling impossible. Single-crystal sapphire fibers have a melting temperature of $\sim$ 2050 °C [27] and can be used at higher temperatures. Most sapphire fiber sensors are based on Fabry-Pérot structures generating broad-band interference fringe pattern that can be monitored as a function of temperature [28]. Sapphire based sensors have been fabricated and demonstrated in high temperature measurements in laboratory experiments [29], [30]. Such sensors will still have to survive the difficult environment of industrial gasifiers and are still untested at these conditions. A well-controlled dopant density is important for measurement accuracy [31], which puts strict requirements on the fabrication process. It has been difficult to achieve high-quality measurement results, since the interference signal from the Fabry-Pérot cavity are degraded by multi-mode electromagnetic fields inside sapphire fibers. These systems during industrial service are prone to mechanical failure due to mismatch in the coefficient of the thermal expansion (CTE) between optical fibers and the sensing element.

Optical pyrometry [32] is an established method for measuring temperatures of flames. For several years, it was used by Texaco [33] in its pilot gasification unit. However, conventional total radiation or single-wavelength pyrometers cannot provide accurate measurement of the flame temperature because an unknown or non-uniform emissivity of the flame. The interference of the background radiation also contributes to the difficulties. A two-color pyrometry removes the limitation of an unknown and changing emissivity by using the irradiance ratio at two carefully selected wavelengths. The application of such an approach has been demonstrated in utility furnaces and different open flames, such as premixed and diffusion flames [34]. More recently, the multi-color method has also been developed.

Though minimally invasive (require a transparent access port), optical line-of-sight techniques are not suitable for temperature and composition measurements when an optically transparent line-of-sight is difficult or impossible to maintain, as in the case of

slagging gasification or when high particle concentration in the reaction zone prevents light transmission. Continuously blown (nitrogen) gas may be used to maintain the line of sight but this will change the gas composition and the temperature of the reactor. Consequently, commercial use of optical pyrometry in gasification is limited, intermittent, and is not seen a replacement of thermocouples.

1.2 Organization of the Report

This Report describes project activities and summarizes the results of our successful development and experimental testing of a novel noninvasive technique for ultrasound measurements of segmental temperature distribution (US-MSTD) in solid materials, such as combustion and gasification refractories and other containments of extreme environments. Chapter 2 describes the essential concept of the approach [35]. Chapter 3 demonstrates its development and describes its performance in measuring temperature distribution in cementitious materials maintained at non-uniform temperature up to 100°C [36,37]. The high temperature testing in laboratory conditions [38] is described in Chapter 4. The details of a robust signal processing technique [39], developed by us to improve the reliability of the US-MSTD method, is described in Chapter 5. The developed measurement system was installed on a pilot-scale down-flow oxy-fuel combustor. The results of a week-log pilot scale testing is given in Chapter 6 [40]. Chapter 7 discusses our experience with selecting US waveguide material that can withstand extreme combustion and gasification environments. The summary of our results, their potential applications, and extensions are outlined in Chapter 8.

Chapter 2 and 3 correspond to paper [36], Chapter 5 corresponds to paper [39].

Chapter 2

Physical Basis of the Method

2.1 Background

Ultrasound (US), because of its high sensitivity, penetrating power, fast response time, great accuracy, and noninvasive operation, has become a widely used probing modality primarily in nondestructive testing (NDT). It can be used to detect and characterize flaw, perform dimensional measurements, characterize material properties, assess microstructural composition and the associated mechanical properties [41]. Ultrasound can be used in real time to provide a feedback to control fabrication and synthesis processes; the materials stability during transport, storage and processing; and the rate of degradation during service life of the materials [42]. The application of ultrasound in medicine includes diagnostic imaging (sonography) and therapies [43, 44]. Sonography is used for evaluating the condition of internal organs and tissues, commonly for neonatal fetuses, heart imaging, and blood flow measurement. High intensity ultrasound is gaining prominence as a method for non-invasive tumor ablation [45–50], targeted drug delivery, and other therapies [51, 52].

Ultrasonic waves are stress waves at frequencies above 20 kHz that can propagate though gases, liquids, and solids [53]. The propagation of a harmonic wave can be described as [54]

$$y(x,t) = y_0 \cos\left(\omega t - \frac{2\pi x}{\lambda}\right), \tag{2.1}$$

where y is the displacement caused by the propagating sound wave with respect to distance, x, and time, t; y_0 is the amplitude of the displacement, ω is the angular wave frequency, and λ is the corresponding wavelength. The values of ω and λ depend on the propagation medium; they are related to the speed of ultrasound propagation (the speed of sound, SOS) and the frequency f as

$$c = f \cdot \lambda, \tag{2.2}$$

$$\omega = 2\pi f, \tag{2.3}$$

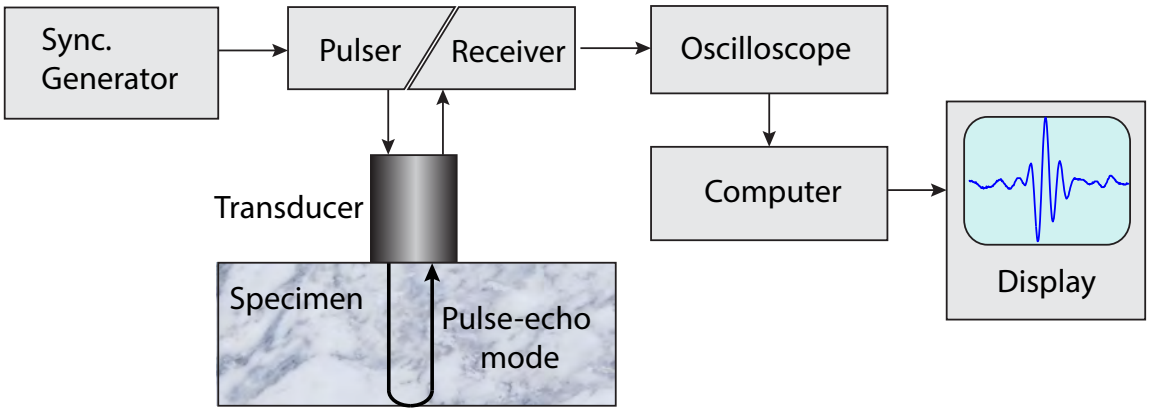

Figure 2.1: Block diagram of basic components of an ultrasonic measurement system used to generate and detect ultrasonic signals.

2.1.1 Basic Ultrasound Instrumentation

Figure 2.1 shows a block diagram of a basic ultrasonic measurement system used to generate and detect ultrasonic waves in a solid specimen. The synchronization generator sends trigger signals to the pulser, often with a high repetition rate. The pulser provides electrical excitation to the transducer which produces ultrasonic waves at the same repetition rate. In the pulse-echo mode, after traversing the specimen and reflecting from the interface, the reflected ultrasonic waves (echoes) return to the receiver (which is if often the same device as the transducer) and are converted to an electrical signal that can be displayed and analyzed.

2.1.2 Speed of Ultrasound Propagation

In the traditional pulse-echo mode, the transducer-generated US pulse propagates through a sample and produces an echo caused by its reflection from the sample's distal end relative to transducer location. For the sample maintained at isothermal conditions, the velocity of ultrasound propagation, c, can be found by measuring the time of flight (TOF), t_{of}, of the returned echo:

$$c = \frac{2L}{t_{of}} \tag{2.4}$$

where L is the distance between the proximal and the distal ends of the sample.

The speed of sound and its propagation modes depend on the transmitting medium. In solids, the SOS depends upon the type of a wave (e.g., p- or s-waves), the elastic properties of the medium, its density, and, in some cases, the frequency [2]. The ratio of applied stress (force/area) to axial strain (extension/length) is the elastic (or Young's) modulus, E, of the material. Piezoelectric transducers can generate longitudinal (compression, also known

as primary wave or p-wave) and shear waves (s-wave), but one type will be dominant depending on the specific design.

The relationship between longitudinal SOS and the elastic modulus in isotropic solids is given by

$$c_{longitudinal} = \sqrt{\frac{K + \frac{4}{3}G}{\rho}} = \sqrt{\frac{E(1-\nu)}{\rho(1+\nu)(1-2\nu)}}. \tag{2.5}$$

where K and G are the bulk modulus and shear modulus of the elastic materials, respectively; E is the Young's modulus, ρ is the density, and ν is the Poisson's ratio. The relationship between the Young's modulus and the Poisson's ratio has the following form:

$$E = 3K(1-2\nu) \tag{2.6}$$

The SOS of s-waves is equal

$$c_{shear} = \sqrt{\frac{G}{\rho}}, \tag{2.7}$$

The SOS of longitudinal waves depends both on the compression and shear resistance properties of the material, while the speed of shear waves depends on the shear properties only.

For a long, thin rod with a diameter shorter than a wavelength, the SOS of longitudinal waves may be simplified and is given by:

$$c_{rod} = \sqrt{\frac{E}{\rho}}. \tag{2.8}$$

Young's modulus of elasticity is sensitive to most structural changes and material damage, including micro-cracking, densification, and phase transitions between different crystal structures. The quantitative assessment of microstructural changes can be carried out through the measurements of ultrasound properties.

Liquids and gases cannot resist shear stresses. The SOS in fluids is expressed as

$$c_{liquid} = \sqrt{\frac{K}{\rho}} = \sqrt{\frac{1}{\beta\rho}}, \tag{2.9}$$

where $\beta = 1/K$ is the compressibility of liquid. For an "ideal gas," the SOS can be shown to be

$$c_{gas} = \sqrt{\frac{\gamma P}{\rho}} = \sqrt{\gamma RT}, \tag{2.10}$$

where γ is the adiabatic index, equal to the ratio of specific heats C_p of a gas at a constant pressure to its heat capacity C_v at a constant-volume; P is the ambient pressure and R is the molar gas constant.

2.1.3 Impedance and Attenuation

Acoustic impedance [55, 56] is defined as

$$Z = \rho \cdot c. \tag{2.11}$$

and is an important characterization of the propagation medium. Another important characteristic is the loss of the acoustic energy as the ultrasound signal propagates through the medium. US attenuation [56, 44] characterizes the reduction in the amplitude of a ultrasonic waveform, and is defined as the logarithm of the ratio of the magnitudes of the original to the attenuated amplitudes, a and a_0, expressed in decibels (dB):

$$A(dB) = 20log_{10}(\frac{a}{a_0}). \tag{2.12}$$

Two types of processes contribute to attenuation of the ultrasound waveforms propagating through the medium. The first process depends on the interaction with the medium, which can cause beam spreading or focusing, energy absorption, and dispersion. The presence of microscopic structural defects, such as point defects and dislocations, and macroscopic defects, affects the degree of hardness and the elastic properties of the material and give rise to absorption that occurs in both metals and nonmetals. The second process contributing to the attenuation is due to wave interactions observed during transmission across interfaces; scattering by material variation and inhomogeneities, such as grains, grain boundaries, and pores; and the Doppler effect [57], [58].

2.1.4 Scattering

Scattering is the primary mechanism by which ultrasonic energy is lost during propagation through many solids. Materials with significant scatter effect the feasibility and effectiveness of engineered waveguides used in the proposed method.

Scattering is the process of redirecting an ultrasonic wave as a result of the interaction between a primary ultrasonic propagating wave and the anisotropic grains (inhomogeneities) inside of the medium [59]. Scattering occurs when the dimension of grains is small relative to the wavelength $\lambda = c/f$, where f is the central frequency of the propagating US [60, 61]. If physical properties of grains and other inhomogeneities, such as density or elasticity, are different from those of the bulk medium, the discontinuity in the velocity of ultrasound propagation at the grain boundary will lead to the localized reflections and loss of acoustic energy. The extent of scattering depends on the number of grains per volume, their size relative to the wavelength (therefore, the scattering process is frequency dependent), and mismatch in acoustic impedance at the boundaries [62].

2.1.5 Reflections and Transmissions

When an ultrasonic wave encounters an interface, several phenomena may occur, including reflection, transmission, refraction, and mode conversion. These interactions are the

phenomena our proposed approach relies upon to create multiple ultrasound echoes from known locations along the length of the US propagation.

Ultrasonic waves are reflected at an interface of two media if there is a mismatch in acoustic impedances (Z) across the interface [53]. Assuming the incident angle is normal to the interface, the fraction of the incident wave intensity that is reflected can be characterized by the reflection coefficient which depends on the acoustic impedances of the materials on either sides of the interface:

$$Re = \left(\frac{z_2 - z_1}{z_2 + z_1}\right)^2, \tag{2.13}$$

where z_1 and z_2 are acoustic impedances of media 1 and 2. The transmission coefficient, which characterizes the ultrasound energy transmitted through the interface, is calculated as

$$Tr = \frac{4z_1 z_2}{(z_2 + z_1)^2}, \tag{2.14}$$

Note that

$$Re + Tr = 1 \tag{2.15}$$

indicating that the reflection and transmission coefficients represent the percentage of acoustic energy which is either reflected or transmitted at a boundary. The greater the impedance mismatch, the greater the percentage of energy that will be reflected at the interface.

2.2 Physical Basis of the US-MSTD Method

Velocity of ultrasound propagation is temperature dependent in gases, liquids, and solids. This dependence is the physical basis of several temperature measurement techniques, such as those reported in [63–65]. Here, we are primarily concerned with measuring temperature in solids. Though the velocity of US propagation (colloquially referred to as the speed of sound, SOS) of all elastic waves is temperature dependent, and thus can be used in thermometry, the longitudinal (primary) waves were emphasized in this project.

The US techniques provide non-invasive or minimally invasive alternatives to the traditional methods of temperature measurements. They are particularly useful when:

- Insertion of temperature probes is undesirable, difficult, or impossible;
- Extreme environments affect longevity of conventional sensors, as is the case for many energy conversion processes; and
- When optical line-of-sight measurements are not practical because the medium is opaque or optically dissipative.

The US temperature measurements can be implemented in all traditional transducer-receiver arrangements. The pulse-echo mode, emphasized in this project, is particularly appealing because in this arrangement, a single device – an US transducer/receiver – is ultrasonically coupled to the proximal end of the waveguide, which may be located outside an aggressive environment, at a stand-off location.

If a sample is maintained at a uniform temperature, by measuring the time of flight, t_{of}, over the known propagation path of length L, the velocity of ultrasound propagation, c, can be calculated using equation (2.4). If the relationship between the speed of sound and the temperature, T, is known from theoretical considerations or empirical correlations,

$$c = f(T) \tag{2.16}$$

then the measured t_{of} can be used to obtain the sample's uniform temperature as:

$$T = f^{-1}\left(\frac{2L}{t_{of}}\right) \tag{2.17}$$

where we assumed that the inversion of (2.16) is unique. Note that, in addition to the time of flight measurements emphasized in this project, other ultrasound characteristics, such as a phase change of echoes produced by a tone burst excitation [66], may be used to characterize temperature-dependent variations in the speed of sound.

The application of this basic idea to measure the temperature in gases is known as acoustic pyrometry and is well established [67, 68] and commercially used in many high-temperature applications [69–71]. The advantage of the approach is the ability to obtain real-time temperature measurements over an extremely large range of temperatures (from 0 to 3500 °F), which makes it applicable to process monitoring from a cold start up to normal high-temperature operation. Disadvantages include significant measurement uncertainties when temperature along the propagation path between the transducer and the receiver varies significantly and unknown changes in the adiabatic constant due to variability in the gas composition. The utilized acoustic frequency range is low (typically, ≤3kHz) because higher frequency ultrasound does not propagate through gases. The consequence of low excitation frequencies is interference from combustion instabilities (sounds produced by a turbulent flow) and other disturbances, collectively known as a passive acoustic signature. Such low frequencies also limit the achievable spatial resolution of measurements when multiple transducers-receivers are used in order to measure the temperature distribution inside of a containment [72]. In addition to high-temperature gas-phase measurement, acoustic thermometry was used to detect temperature changes in the ocean by receiving low-frequency ultrasound (< 100 kHz) transmitted across an ocean basin [73].

Examples of ultrasound measurements of the uniform temperature in solids are relatively few. Lee et al. [64] reported the development of an acoustical temperature measurement system which uses the TOF measurements of an acoustic wave introduced into

the silicon wafer through an excitation quartz rod. The wave, partially reflected from the quartz-silicon interface, travels through the wafer until reaching a second quartz rod through which the wave reaches the receiver. The difference between an arrival time of the reflected wave and the wave reaching the receiver through the second rod gives the time of flight through the wafer, which is used to estimate the wafer temperature. Lee et al. reported that ± 5 °C accuracy was achieved in the range from room temperature to 1000 °C. Another example of high temperature application of US thermometry is given by the form of Balasubramaniam et al. [74] who used an ultrasonic sensor to measure viscosity and temperature of molten material up to 1000 °C with the temperature resolution of 5 °C.

US thermometry was also used in biomedical applications. For example, Arthur et al. [75] investigated the use of backscattered ultrasound energy in temperature measurements to monitor and control noninvasive thermal therapies of tumors. Using 7 MHz linear ultrasound phased array transducer, they demonstrated temperature measurements in ex vivo phantom tissue from 37 to 50 °C in 0.5 °C steps. The project did not progress towards in vivo testing because the quality of temperature measurements was severely affected by subject motion, unavoidable in subjects due to breathing and other disturbance. Simon et al. [76] developed a 2D temperature estimation method based on the detection of shifts in echo location of the backscattered ultrasound from a tissue undergoing thermal therapy.

The application of US thermometry becomes problematic when the temperature of the sample is non-uniform. At the same time, a non-uniform temperature distribution (often with large thermal gradients) in containments and other solid structures is the most relevant case in most energy, defence, and other applications, as is the primary focus of this project.

When the temperature along the ultrasound propagation path is not uniform, the measured time of flight of ultrasound echoes encodes the spatial distribution of the temperature along the entire propagation path. The relationship between the measured t_{of} and an unknown temperature distribution, $T(z)$, is given by the following measurement equation:

$$t_{of} = 2 \int_0^L \frac{1}{f(T(z))} dz. \tag{2.18}$$

Unlike the isothermal case described by (2.17), there are arbitrary many temperature distributions $T(z)$ such that, when used in (2.18) to predict t_{of}, the result will be identical to the measured time of flight. Consequently, the deconvolution of the measurement equation (2.18) is an ill-posed problem.

The lack of unique dependence of the measured t_{of} on the temperature distribution presents a difficulty that may be resolved in one of several ways. In the first approach, the problem is regularized by imposing additional constraints on the temperature distribution. This has an effect of parameterizing "admissible" temperature distributions by prescribing a functional form that depends on one or more unknown parameters, which are then found from ultrasound and, perhaps, other measurements. Parameterizations may include: a)

an assumption that the temperature along the US propagation is constant and given by (2.17); b) the temperature distribution is linear along the sample; and c) the requirement that $T(z)$ satisfies a heat transfer model with an appropriately selected parameters (such as thermal conductivity) and boundary conditions.

Typically, an assumption of a constant temperature T_a across the ultrasound propagation path, calculated from (2.17) using the measurements of t_{of}, results in the least accurate temperature estimation. The relationship between the calculate "average" T_a needed to match the measured TOF and the unknown temperature distribution $T(z)$ is given by the following equation:

$$\int_0^L \frac{1}{f(T(z))} dz = \frac{L}{f(T_a)} \tag{2.19}$$

Such approximation is particularly problematic when strong thermal gradients are present. This is the case when the temperature distribution across refractories of energy conversion processes or other containments of extreme environments are of interest.

The TOF measurements alone are insufficient to reconstruct the temperature distribution parameterized with more than a single unknown. For example, the linear parametrization is determined by an unknown slope and an intercept, both of which cannot be determined simultaneously from a single measurement of t_{of}.

Several examples of the deconvolution of the TOF measurements based on thermal models are found in the literature. Takahashi and Ihara [77] assumed that a one-dimensional heat transfer model adequately describes the temperature distribution along the length of the ultrasound propagation. They furthermore assumed that the relationship (2.16) is linear, and the boundary temperature at the transducer location is known (e.g., independently measured). Therefore, only the boundary condition at a distal end of the sample is needed to calculate the model prediction of the temperature distribution, $T(z)$, and the corresponding time of the flight, predicted by the measurement equation (2.18). In [77], temperature of the distal end was selected as the boundary condition needed to completely define the heat conduction model. An alternative boundary condition that specifies the heat flux at the distal end of the sample was used in [78]. In both cases, the selected distal boundary condition (either the distal temperature, or the heat flux) was estimated as the value that minimizes the difference between the predicated TOF and its measured value. The temperature distribution through the sample was then found as the solution of the obtained heat conduction problem.

An alternative to reducing the number of unknowns by parameterizing the temperature distribution is to use more than a single TOF measurement in temperature reconstruction. This is possible when multiple transducers and receivers are used to measure the transmit and echo delays along different ultrasound propagation paths, followed by the reconstruction of the temperature distribution (e.g., [63, 72, 79]) using a procedure similar to computer tomography. System theoretical discussion of similarities of ultrasound and other noninvasive measurement modalities, in which the acquired data depends on the

spatial integral of the property of interest, is given in [80].

The third distinct approach is to devise a way to extract more information from each ultrasound transducer-receiver than a single time of flight measurement. This is possible if each ultrasound excitation pulse produces multiple ultrasound reflections, caused by echogenic features encountered as it propagates through a sample. In an approach reminiscent to Bragg grating of optical fibers (see, for example, [81]), Hanscombe and Richards [82] proposed a method in which an ultrasound waveguide is engineered to have regions of periodic ultrasound gratings, each producing US echoes with different dominant frequencies determined by grating dimensions. Temperature variations change these dimensions through thermal expansion and thus shift the frequency content of the echoes. By using gratings of different dimensions at different spatial locations along the waveguide, multiple frequency-separated echoes are produced, each encoding temperature changes in a different spatial location. In this approach, the cross-talk between overlapping echoes is reduced. However, the frequency content of echoes produced by grating zones is insensitive to the temperature distribution between them. The described approach apparently has not been tested in experiments, leaving many unanswered questions. For example, it is not clear how long each grated zone should be to insure narrow frequency content of each echo. The achievable accuracy as a function of grating design also remains unknown. The accuracy of temperature measurements when thermal gradients are present within each grated zone, leading to a wider frequency band of each echo, has not been quantified, as well.

The method for ultrasound measurements of segmental temperature distribution (US-MSTD) in solids developed during this project may be viewed as an approach which extracts more than a single TOF data from each US excitation. In this approach, the ultrasound propagation path consists of n segments defined by echogenic features bounding each segment. The difference in the time of flight between consecutive echoes, produced by partial ultrasound reflections from the echogenic features, is used to estimate the temperature distribution across the segment. Different parameterizations of segmental temperature distribution may be used. Therefore, the US-MSTD method may be viewed as the development of a hybrid approach which extracts more information from each ultrasound excitation than a single time of flight measurement and deconvolutes the information encoded in the TOF of each echo by parameterizing the segmental temperature distributions.

2.3 Method

The US-MSTD method is graphically summarized in Fig. 2.2 for the case when the temperature across the containment of an aggressive process is measured. Its essential components are:

- The structured ultrasound propagation paths with echogenic features creating partial

ultrasound reflections from known locations;

- An ultrasound instrumentation needed to create the excitation pulse and receive the train of resulting echoes;
- The signal processing of the ultrasound waveforms needed to accurately determine the speed of sound or its change in different segments of the propagation path by measuring the echoes' time of flight;
- The relationship between the SOS and the temperature; and
- The method to translate the segmental speed of sound into the temperature distribution such that the predicted time of flight, according to the measurement model (e.g., equation 2.18), matches the measured values.

In the described approach, the sensitive electronic components are kept away from harsh gasification environments and it is only required that the US transducer be acoustically coupled to the cold side of the refractory, representing minimal modifications to the gasifier.

In the following, the components of the method are discussed in more details.

2.3.1 Structure US Propagation Path

The central idea of the US-MSTD method is to have an US propagation path that incorporates echogenic features at known locations that redirect a portion of the US energy of the excitation pulse back to the transducer where the train of echoes is recorded. The TOF of these echoes encode the temperature distribution with finer granularity by providing information specific to the temperature distribution within individual segments.

For cementitious samples, several methods for producing partial internal US reflections were investigated [36]. It was found that inclusions, stratifications, and variations in the waveguide geometry are the adequate means in creating the structured US propagation path. For example, it was found that by casting multiple cementitious layers of identical composition and allowing time for a partial curing before consecutive castings, enough variation in acoustic impedance is introduced to create partial US reflections at the interface of the layers. With such implementation, thermal, chemical, and mechanical properties remain essentially constant throughout the structured material. In another example [39, 38, 40], echogenic features were obtained by drilling small holes along the length of a ceramic (alumina) waveguide.

An alternative to purposefully structuring the waveguide, the echogenic features occurring naturally in the material or introduced for reasons unrelated to the needs of the US-MSTD method may also be used. These may include natural stratifications, natural inclusions, or geometric features, such as a rifling inside a gun barrel used in [78] to estimate the temperature variations caused by firing a gun. It is only required that the spatial

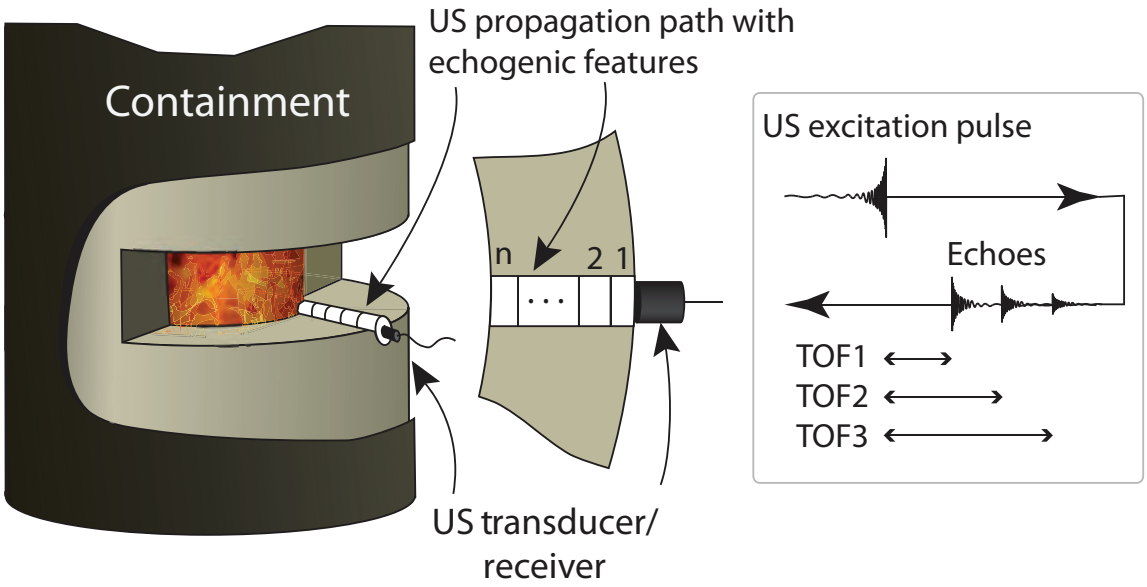

Figure 2.2: The method for ultrasound measurements of segmental temperature distribution (US-MSTD) in solids: An excitation pulse created by an US transducer propagates through the structured containment and encounters n echogenic features along the way, which produce a train of echoes acquired by the receiver. The TOF difference between consecutive echoes is used to estimate the temperature distribution in the corresponding segment of the containment. By sequentially estimating the temperature of each segment, the temperature distribution along the entire path of ultrasound propagation is obtained.

locations of echogenic features are characterized prior to their utilization in the US-MSTD method.

2.3.2 Acquisition of Echo Waveforms

A measurement of the temperature distribution in a pulse-echo mode begins with an excitation of an ultrasound pulse by a transducer. As the US pulse propagates through the structured material, multiple echoes are produced by each echogenic feature encountered along its path. The waveforms of returned echoes (labeled in Figure 2.2 by their time of flight $TOF1$, $TOF2$, $TOF3$, …), acquired by the US transducer, are the primary data used to measure the segmental time of flight, and to estimate the temperature distribution in each segment.

The time of flight $t_{of}^{z_i}$ of the echo produced by a feature located at z_i is related to the

temperature distribution along its propagation path as

$$t_{of}^{z_i} = 2\int_0^{z_i} \frac{1}{f(T(z))} dz \tag{2.20}$$

where it was assumed that the trasducer/receiver is located at $z = 0$. The temperature distribution in the i-th segment of the propagation path is inferred from the difference in the time of flight, t_{of_i}, between consecutive echoes produced by echogenic features which bound the segment at the locations z_i and z_{i-1}:

$$t_{of_i} = t_{of}^{z_i} - t_{of}^{z_{i-1}} = 2\int_{z_{i-1}}^{z_i} \frac{1}{f(T(z))} dz \tag{2.21}$$

where $(z_i - z_{i-1})$ is the segment's length. The TOF of the first echo depends on the temperature distribution across the 1st segment of the refractory, between the cold surface and the first echogenic feature. The next return echo will originate from the second echogenic feature. Then the difference in the TOF between the second and the first echoes gives the information on the temperature distribution in the second segment, and so on until the estimate of the temperature distribution across the entire refractory is obtained. With that distribution known, the last echo, reflected from the refractory-reactor zone surface, can be used to determine the temperature of the refractory's interior hot surface. Note that we often use the first segment between the transducer and the first echogenic feature at z_1 as a delay line and reference the time of flight of all subsequent echoes to the arrival time of the first echo, $t_{of}^{z_1}$.

2.3.3 Signal Processing

The speed of sound is calculated as the distance traveled by an ultrasound pulse divided by the time of propagation (or time of flight, TOF). Therefore, a method for precise measurements of the time of flight is essential to accurate measurements of temperature distribution. The simplest approach to the measurements of the TOF and its changes is to use temporal location of a single-point waveform feature, such as the first zero crossing or the peak value of the waveform. Though standard, these timing techniques are sensitive to measurement noises. Furthermore, when broad-band excitations are used, the timing accuracy of single-feature methods deteriorates further due to waveform distortions and broadening caused by stronger attenuation of higher-frequency content of ultrasound pulses.

More robust and accurate measurements of t_{of} and t_{of_i} may be achieved when the entire shape of the waveform is utilized in timing. In this case, both amplitude and phase information are taken into account [83], which makes timing results less sensitive to measurement noises and shape distortions. Mathematically, the cross-correlation between

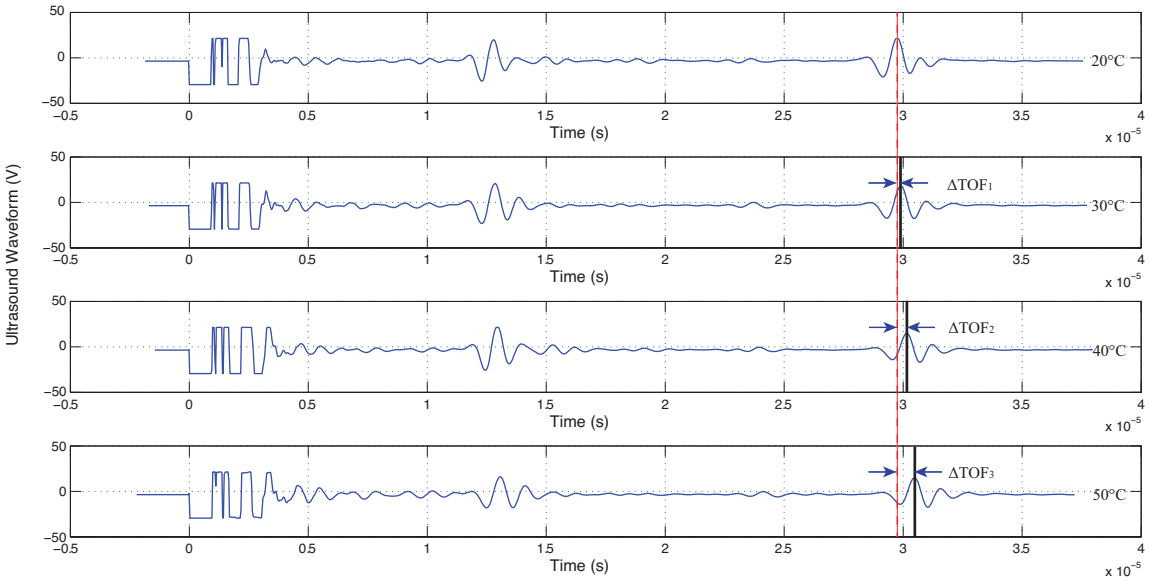

Figure 2.3: The ΔTOF between echo waveforms at different temperatures is calculated by cross-correlation with a reference waveform acquired at 20 °C.

two signal $f(t)$ and $g(t)$ is represented as:

$$\varphi_{fg} = f \star g(\tau) = \int_{-\infty}^{+\infty} f^*(t)g(t+\tau)dt, \tag{2.22}$$

where f^* is the complex conjugate of f and τ is the lag time between two signals. The temporal shift τ needed to obtain the best match between the waveforms may be found by maximizing their cross-correlation φ_{fg} [84], minimizing l_1 and l_2 norms of their difference [85], [86], [87], or by maximum likelihood [88]. Figure 2.3 shows ΔTOF between two echoes is obtained by finding the best match of the entire normalized shape of the two waveforms as based on both phase and amplitude information, which makes timing results less sensitive to noises and shape distortions.

Though cross-correlation and other shape-matching methods perform better than single-point timing, the results may still be unacceptable when significant distortion of ultrasound waveforms occurs, as is often the case when the pulse propagates through attenuating and dissipative materials. It was suggested by Le [89] that for waveform distorting samples, a higher precision can be achieved if the envelopes of the waveforms are used in timing. The analytic signal, $s_a(t)$, of the waveform, $s(t)$, is the following complex function:

$$s_a(t) = s(t) + j\hat{s}(t), \tag{2.23}$$

where $j^2 = -1$ and $\hat{s}(t)$ is the Hilbert transform of $s(t)$:

$$\hat{s}(t) = -\frac{1}{\pi} \lim_{\varepsilon \to 0} \int_{\varepsilon}^{\infty} \frac{s(t+\tau) - s(t-\tau)}{\tau} d\tau. \tag{2.24}$$

The envelope of the waveform $s(t)$ is then calculated at the amplitude of its analytic signal:

$$A(t) = |s_a(t)| = \sqrt{s^2(t) + \hat{s}^2(t)}. \tag{2.25}$$

We have recently shown [39] that further improvements in timing accuracy can be achieved by iteratively applying a nonlinear anisotropic diffusion filter to the envelopes of the echo waveforms.

2.3.4 Temperature Dependence of the Ultrasound TOF

The unknown temperature distribution is estimated from the measurements of the time of fight of ultrasound echoes. The length of the propagation path and the SOS both change with the temperature of the sample and thus influence the echoes' TOF. These factors typically contribute to the lengthening of the time of flight as temperature increases. For relatively short waveguides and small temperature ranges, the contribution of thermal expansion is negligible.

Note that it is possible to separate individual contributions of thermal expansion and the changing SOS to the measured time of flight. However, as long as the calibration curve (2.16) is obtained without such differentiation, there is no practical need to distinguish the degree each one of the two factors contribute to the measured change in the TOF with temperature. The subsequent discussion assumes that the correlation between the SOS vs. temperature, Eqn. (2.16), was not corrected for the thermal expansion. This simplifies the method, as it is becomes unnecessarily to adjust the length of the propagation path in Eqn. (2.18) and (2.20) for the thermal expansion.

2.3.5 Estimation of Temperature Distribution

The measurements of the segmental time of flight t_{of_i} encode the information on the temperature distribution within i-th segment. As before, additional assumptions are needed to estimate the segmental temperature distribution from the measurement model (2.20). All parametrization options discussed in the context of deconvoluting model Equation **??** may be used for this purpose, and are discussed below.

Piecewise Constant Distribution

This distribution is obtained by assuming constant speed of sound within each segment. Using this assumption in Equation (2.20), the constant SOS in the i-th segment of the

waveguide is obtained as

$$c_i = \frac{2(z_i - z_{i-1})}{t_{of_i}}, \tag{2.26}$$

The corresponding constant temperature is obtained by inverting the correlation (2.16). After repeating the process for all segments, the entire temperature distribution along the waveguide is approximated as a piecewise constant function. Infeasible temperature discontinuities occurring at the locations of the echogenic features is an undesirable feature of such approximation. Nevertheless, its accuracy is significantly better than can be obtained by assuming a constant T_a along the entire path of ultrasound propagation. Furthermore, by using a larger number of echogenic features and the correspondingly finer segmentation of the waveguide, this approximation can be further improved.

Piecewise Linear Distribution

The temperature continuity may be enforced by assuming that the temperature changes linearly within each segment. For the i-th segment, this gives that

$$T(z) = m_i z + n_i, \;\; z_{i-1} \le z \le z_i \tag{2.27}$$

where m_i and n_i are unknowns. To further illustrate this parametrization, consider a sample segmented by several echogenic features. Further assume that at the transducer location, $z = 0$, the temperature of the sample's proximal end is measured independently (e.g., by using a surface thermocouple), and is equal to $T(0) = n_1$. By using the measured TOF of the first echo and the linear temperature distribution in Eqn. (2.21), the following equation is obtained

$$t_{of_1} = 2\int_0^{z_1} \frac{1}{f(m_1 z + n_1)} dz \tag{2.28}$$

from which the unknown slope of the distribution, m_1, can be found. Similarly for the second segment, the unknown slope m_2 and intercept n_2 are obtained from the solution of the following two equations:

$$t_{of_2} = 2\int_{z_1}^{z_2} \frac{1}{f(m_2 z + n_2)} dz \tag{2.29}$$

$$n_2 = (m_1 - m_2) z_1 + n_1 \tag{2.30}$$

where t_{of_2} is the difference in the TOF of the second and first echoes and the second equation enforces the continuity of the temperature at $z = z_1$. The process continues for all remaining segments until the piecewise linear approximation of the temperature distribution over the entire sample is obtained. For the i-th segment, the unknown slope m_i and intercept n_i are obtained from the solution of the following two equations:

$$t_{of_i} = 2\int_{z_{i-1}}^{z_i} \frac{1}{f(m_i z + n_i)} dz \tag{2.31}$$

and

$$n_i = (m_{i-1} - m_i) z_{i-1} + n_{i-1}, \tag{2.32}$$

where t_{of_i} is the difference in the TOF of the i and $i-1$ echoes, and Equation 2.32 enforces the continuity of the temperature at $z = z_{i-1}$.

Parametrization with thermal conductivity model

The temperature parametrization by the following one-dimensional heat conduction models was used in references [77] and [78]:

$$\rho C \frac{\partial T}{\partial t} = \frac{1}{r} \frac{\partial}{\partial r} k \left(r \frac{\partial}{\partial r} \right) T, \tag{2.33}$$

where ρ, C, and k are refractory density, heat capacity, and thermal conductivity, respectively. In both cases, the temperature of the distal end, T_h, was unknown and elevated, the temperature at the location of the transducer, T_c, was assumed to be independently measured, and the temperature distribution, $T(z)$, was estimated by adjusting a single boundary condition in order to match the predicted and the measured TOF of an echo produced by a reflection of the excitation pulse from the distal end of the ultrasound propagation path.

When a two- or three-dimension model is needed to provide an adequately accurate description of the temperature distribution in the sample, additional measurements will be required to reconstruct the temperature distribution. For example, consider the case of a cylindrical waveguide with the transducer, used to launch an excitation pulse in the axial direction, coupled to one of its ends. Assuming the radial symmetry of the temperature distribution, constant density ρ, heat conductivity k and capacity C_p, the temperature distribution inside the sample must satisfy the following 2D heat transport model in cylindrical coordinates:

$$\rho C_p \frac{\partial T}{\partial t} = k \left(\frac{1}{r} \frac{\partial}{\partial r} r \frac{\partial T}{\partial r} \right) + \frac{\partial^2 T}{\partial z^2} \tag{2.34}$$

where r is the radial position relative to the centerline of the sample. To completely define the problem, three boundary conditions – at the proximal, distal and the cylindrical surfaces of the waveguide – are required. If the waveguide is unstructured, only a single US echo will be produced by a reflection from a distal end of the sample and measurement of its TOF will allow us to estimate only one of the three needed boundary conditions. The other two boundary conditions must be obtained from independent measurements. For example, if the temperatures of the distal and proximal ends of the waveguide are independently measured, then the measured Δt_{of} can be used to estimate the overall heat transfer coefficient h and define the remaining boundary condition given as the heat flux

through the cylindrical boundary of the waveguide:

$$q = h(T_e - T) \tag{2.35}$$

where T_e is the ambient temperature of the environment. The time of flight of multiple echoes received when the excitation pulse propagates through a structured waveguide provides sufficient data to estimate all required boundary conditions without the need for additional independent measurements. When such independent measurements are available, they can still be incorporated into the US-MSTD method and may help improve the accuracy and the robustness of the estimated temperature distribution.

2.3.6 Estimation of Heat Fluxes

The measurement of conductive heat fluxes through a solid is currently obtained by attaching a flux sensor to the surface of the sample. It is therefore capable of estimating only a localized heat flux in the immediate proximity of the sensor. The approach proposed in this paper can be used to profile the temperature distribution across the entire sample. It can, therefore, be used to non-invasively estimate conductive heat fluxes through the sample, at a considerable distance from the surface where the US transducer is attached. Specifically, by differentiating (exactly or approximately) the estimated temperature distribution $T(z)$, the conductive heat flux, q, across the sample is found as:

$$q(z) = -k\frac{dT}{dz} \tag{2.36}$$

For the case of a piecewise constant temperature profile, one form of an approximate differentiation gives:

$$q(z) \approx -k\frac{T_i - T_{i-1}}{z_1 - z_{i-1}} \tag{2.37}$$

The piecewise linear temperature distribution will result in a piecewise-constant estimation of the heat flux distribution in the direction normal to the plane of the ultrasound traducer. An even more detailed estimation is possible when the heat flux is calculated based on the temperature profile that satisfies the heat conduction model.

2.3.7 Segmental characterization of elastic properties

The proposed method essentially depends on the measurement of the segmental speed of sound (or its change) in a solid sample. Factors, other than temperature, that influence the speed of sound include the density of the material and its elastic properties. For example, the velocity of longitudinal waves (p-waves) in i-th segment of a "long" waveguide maintained at isothermal conditions is equal to

$$c_i = \sqrt{\frac{E_i}{\rho_i}} \tag{2.38}$$

Therefore, by measuring the SOS we can characterize the spatial changes in Young's modulus E of the sample and/or its density, ρ. Note that, as with the estimation of the temperature distribution, the change in these properties may be reconstructed under the assumption of their piecewise-constant or piecewise-linear change in a different segment, or other suitable parameterizations.

Chapter 3

Low Temperature Laboratory Experiments

The feasibility of the US-MSTD method hinges on the resolution of two questions:

1. For a given application, is it possible to introduce echogenic features, which create partial internal reflections along the path of the ultrasound propagation? What methods can be used to create such reflections?

2. Is the speed of ultrasound propagation sufficiently dependent on the temperature to allow for accurate remeasurements of the temperature distribution?

These questions were initially investigated for cementitious models of the refractory and tested in a low temperature range.

3.1 Cementitious Waveguide Partial Reflector Structures

Creating partial internal ultrasound reflections from known spatial locations inside the sample is the key prerequisite for the proposed approach to work. Two solutions, illustrated in Figures 3.1(A) and 3.1(B), were investigated with cementitious samples. Figure 3.2(A) compares the ultrasound echo waveforms from two similar 4 cm long cementitious samples, one of which (waveforms in red) contains a few 0.5 mm steel shots placed in the middle of the sample during its casting.

The result clearly shows a partial echo from inside of the sample created by embedded US reflectors. The range of other material has been investigated in order to find the most appropriate selection for internal reflectors. An ideal choice for partial reflectors would be a material with identical thermal expansion, and chemical and mechanical resistances similar to that of the surrounding refractory material; steel clearly does not satisfy these specifications.

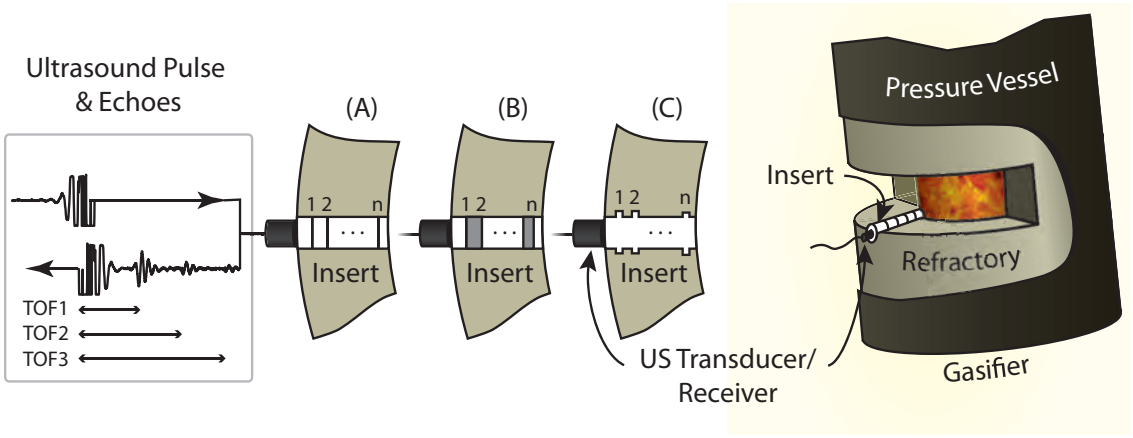

Figure 3.1: Acoustic measurements of temperature distribution in the refractory. (A) Refractory material contains embedded planes of scattering material. (B) Layered refractory. (C) Refractory insert with geometric changes in the ultrasound propagation path creates partial back scattering. *Left panel* shows an ultrasound excitation pulse and the train of partial echoes produced by internal partial ultrasound reflectors. *Right panel* illustrates an engineered ultrasound waveguide/insert – with internal back scatterers, layers structure, or geometrical changes – embedded into the gasifier refractory.

We, therefore, investigated if the concept implemented by small variations in the composition of the layered cementitious materials, creating partial internal reflections at the interface between the layers. This approach was found to be successful. In fact, it was found that by casting multiple layers of the *same* composition and allowing for a partial curing before casting the next layer, enough variation in acoustic impedance is introduced to create partial US reflections at the interface. Such implementation of the refractory with the embedded partial internal ultrasound reflectors is particularly appealing since each layer will have essentially identical thermal, chemical and mechanical properties. Figure 3.2(B) illustrates this approach. It depicts the results obtained with the cementitious sample (shown in the insert) obtained by casting three 1-inch thick layers of identical cement mixtures and allowing for a partial cure before the next layer is cast. Note three distinct echoes, produced at the two internal interfaces and the distal end of the sample.

To determine conditions needed to create detectable partial internal reflections originating from the interfaces between consecutively cast layers, three groups of cementitious samples were made by layered casting of Portland type I/II cement. Two inches of I.D. PVC tubing was cut in lengths of 2, 3 and 4 inches and used as a mold. The water-cement mixture was poured into a vertically oriented PVC mold in several layers approximately 1 inch thick, altering the duration (cure time) between the previous and the subsequent pours. To help with uniform setting of each layer and removing of air bubbles, the mold

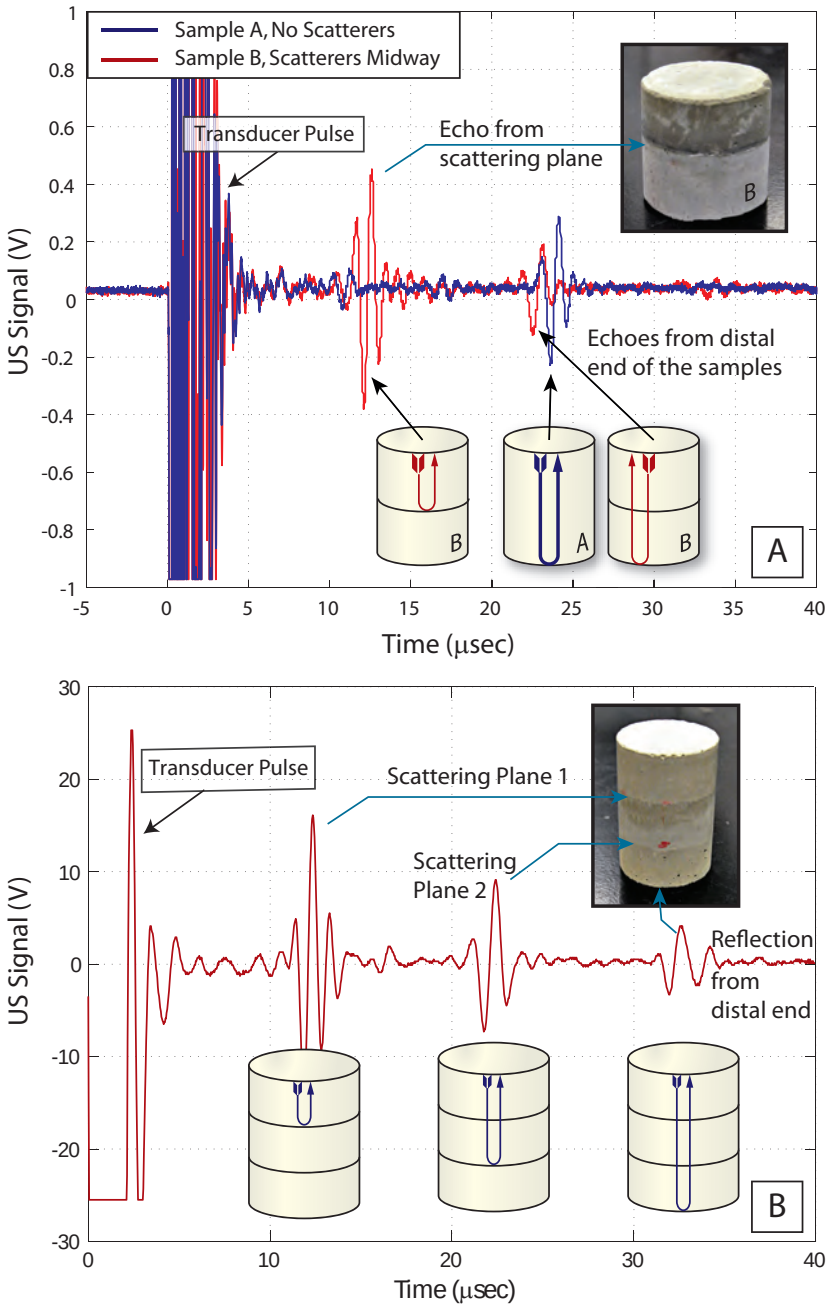

Figure 3.2: Ultrasound pulse-echo response for the samples with echogenic features. (A) The pulse-echo ultrasound response of two samples fabricated from the identical cementitious material. One of the samples (Sample B; shown in inserted photograph) contains embedded ultrasound scatterers at the midpoint of ultrasound propagation path, which produces partial reflection (red line). (B) Ultrasound pulse-echo response for the sample with two internal interfaces obtained by sequentially casting three layers of identical formulation and allowing time for a partial cure to occur prior to pouring the next layer.

was vibrated by a high speed vibrator applied to the outside surface. The curing time for different layers varied from 15 minutes to days. Fresh cementitious mixtures of identical composition were prepared right before the casting of each new layer. The water-cement ratio by weight also changed which was found to have a significant effect on the outcome. All samples were cured in air and at least one week was allowed after the casting of the final layer before ultrasound testing; this long cure eliminated short term aging effects. The ultrasound tests of cementitious samples were carried out using Panametrics pulser/receiver (model 5072PR) and Panametrics immersion transducer with a central frequency of 1 MHz (model V302), coupled to a sample using an ultrasound gel. The data were acquired using Tektronix oscilloscope (model MSO 2024) interfaced to a computer.

3.1.1 High Water-Cement Ratio Samples and Varying Curing Times

The water-cement ratio used for this group of cementitious samples was 0.5, which is the highest water content in the manufacture's recommended range. At this ratio, the mixture can be easily and uniformly poured into PVC molds. With two pours, each 1 inch thick, two layer samples are created that have a single internal interface. To investigate the effect of the cementitious curing time, several samples were created in which we varied the time the first layer was allowed to cure prior to completing the sample with the second pour. The curing time for the first cementitious layer was set to 15, 30, 45 minutes or 1 hour for different samples.

The results of ultrasound tests show that the clearest partial internal reflections are observed with samples in which the first cementitious layer was allowed to cure for 1 hour (Figure 3.3).

The reflections from the internal interface are less clearly defined when the curing time was 45 minutes, indicating some mixing at the interface and a smaller change in acoustic impedance between the layers that were cast with smaller delay (Figure 3.4(A)). Further reduction in time allowed for the first layer to cure makes the two layers even less distinguishable to ultrasound testing, indicating a higher degree of mixing at the interface. For the samples cured for only 15 minutes, we did notice the change in the ultrasound signature depending on the position of the ultrasound transducer relative to the center axis of the mold (Figure 3.4(B)). The signature is smaller closer to the center of the mold. We speculate that this may be due to the difference in temperature with radial position, caused by exothermic hydration curing reaction, resulting in different curing rates in different spatial position. Pouring the second layer after 15 minutes of curing results in a situation where the center of the first layer is less cured, allowing partial mixing with the newly poured second layer, which results in a minimal variation in the ultrasound impedance of the two layers in the center of the sample.

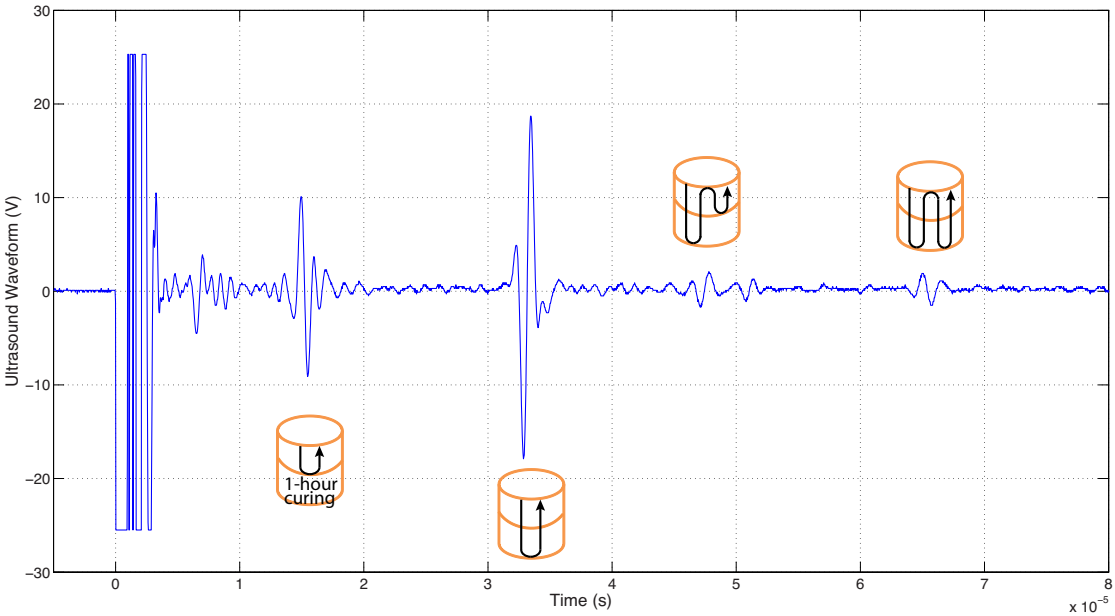

Figure 3.3: Ultrasound response of samples with the single internal interface obtained by allowing the first cementitious layer to cure for 1 hour. Inserts schematically depict the locations producing the acquired echoes: The first echo is the partial internal reflection from the interface between the two layers; the second echo is from the distal end of the sample. Round-trip echoes from partial internal reflection and the distal end were also seen.

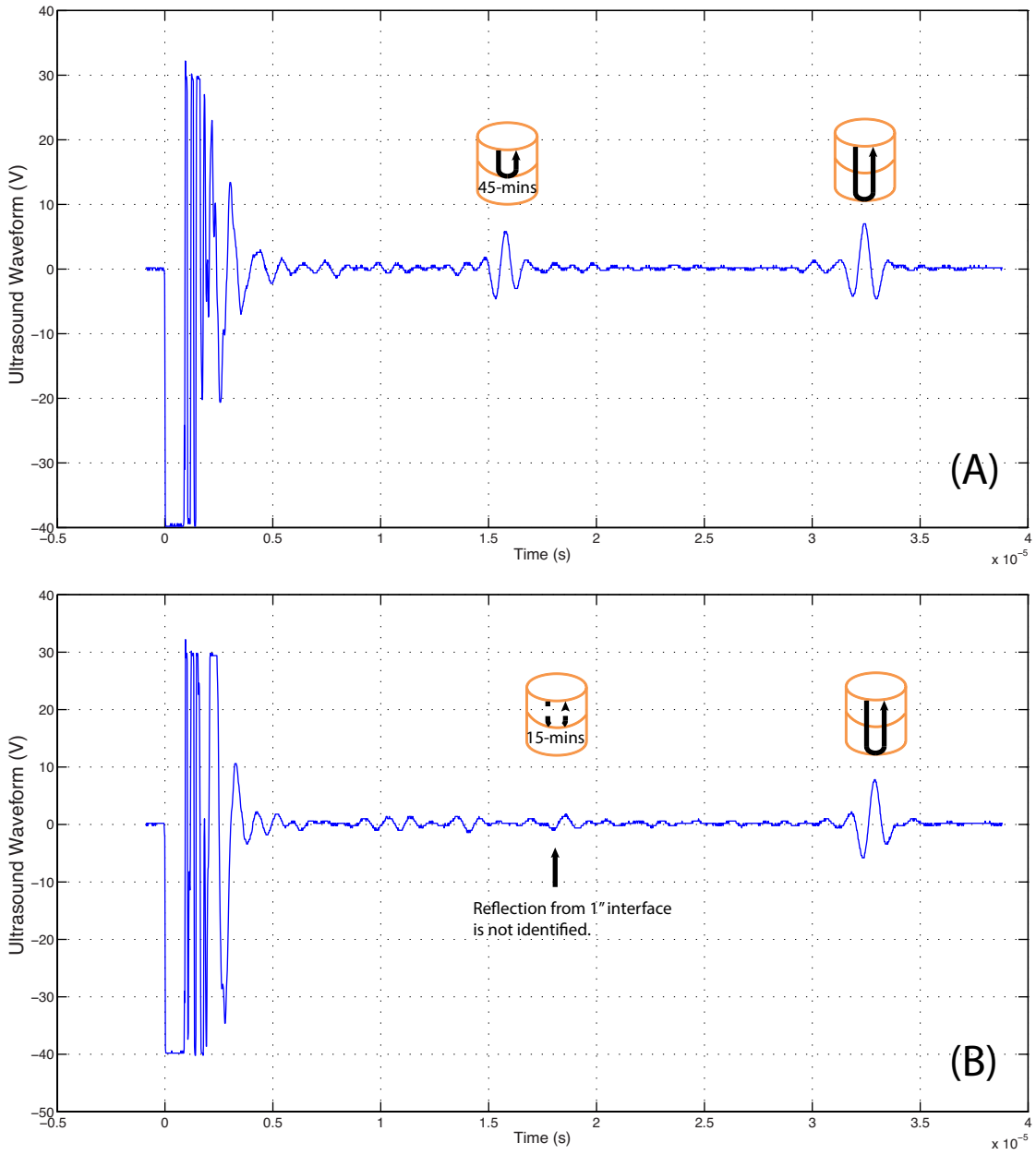

Figure 3.4: Ultrasound response of samples obtained by sequential casting of two 1" layers of cement. The single internal interface between the layers is obtained by allowing the first cementitious layer to cure for 45 minutes (A) or 15 minutes (B). Inserts schematically depict the locations creating the acquired echoes. In (A), both, the partial internal reflections and the reflection from the distal end of the sample are clearly visible. In (B), the reflection from the interface is not well defined and varies with the change in the transducer position relative to the centerline of the sample.

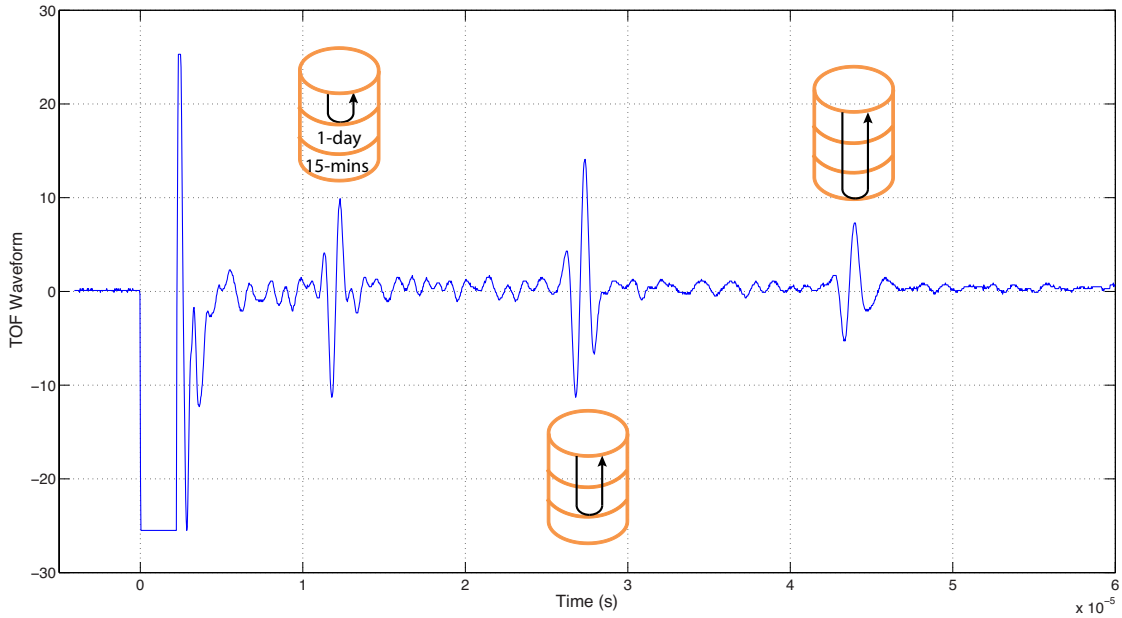

Figure 3.5: Ultrasound response of samples with two internal interfaces obtained by allowing the first cementitious layer to cure for 15 minutes, 1 day for the second layer, and at least 1 day for the final third layer. Water-cement ratio was equal to 0.36. Inserts schematically depict the locations at which the acquired echoes were created. Three echoes are clearly visible, of which the first two are from the internal interfaces created by multiple layers cast sequentially.

3.1.2 Low Water-Cement Ratio Samples and Varying Curing Times

This group of samples were cast with two internal interfaces obtained by sequentially casting three cementitious layers, 1 inch thick, using the water-cement ratio of 0.36, which was selected to be as small as possible while still allowing for layered casting of the sample with minimal air entrapment. The cure time for the first cementitious layer was also set to 15, 30, 45 or 60 minutes for different samples before pouring the second layer. The final, third layer was poured after the sample was allowed to dry for one day.

The ultrasound tests showed that all cementitious samples made according to this recipe exhibit partial internal reflections from each of two internal interfaces, even after a short curing time of 15 minutes (Figure 3.5), likely reflecting the reduction in mixing at higher viscosity. The tests also showed a higher signal-to-noise ratio (SNR) in this group of samples (Figures 3.5, 3.6), which may be due to air entrapment during multiple castings of this mixture with a relatively low water content.

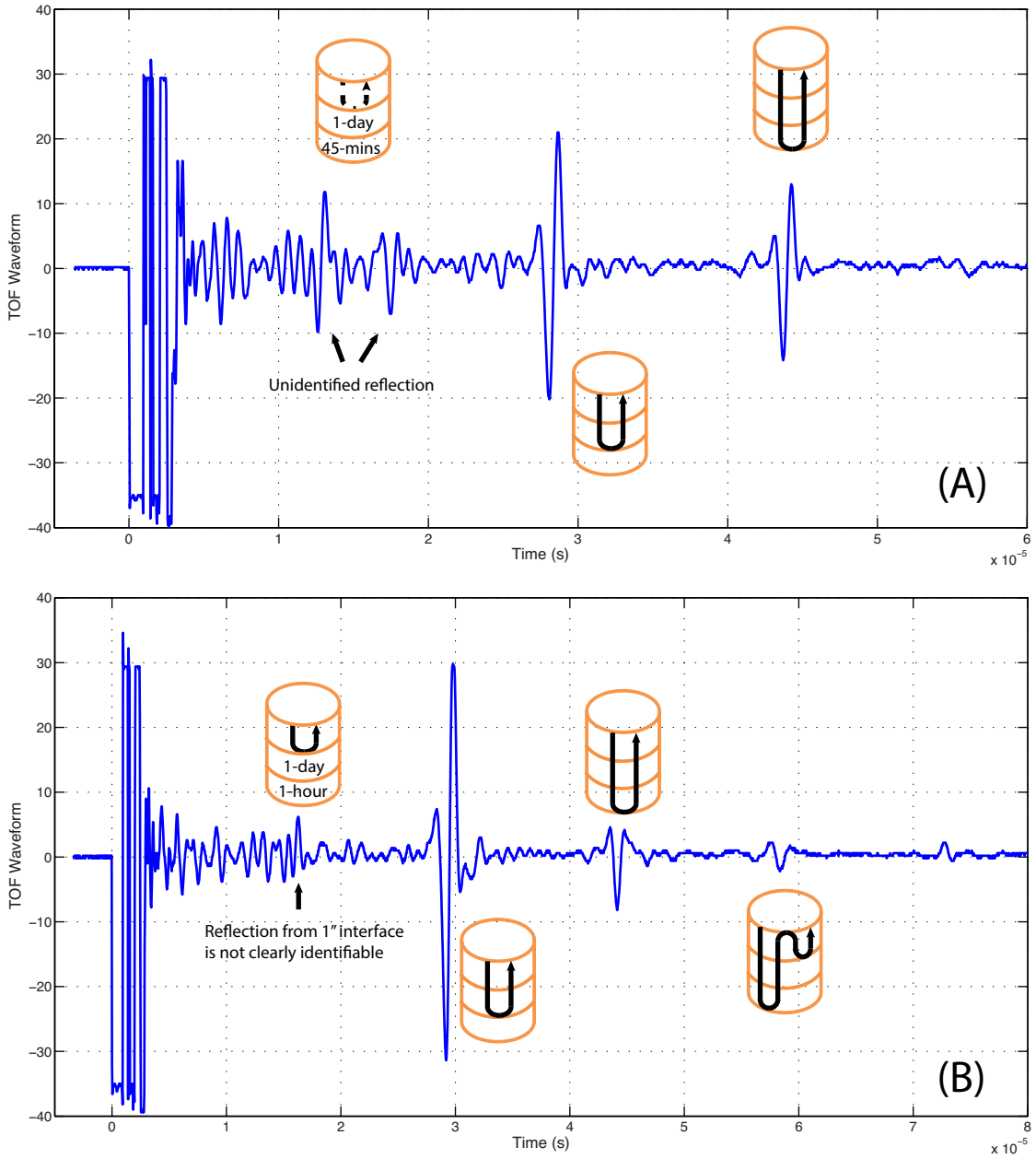

Figure 3.6: Ultrasound response for samples with the two internal interfaces obtained by allowing the first cementitious layer to cure for 45 minutes (A) or 1 hour (B). For both samples, the second and third layers were cured for al least 1 day. Water-cement ratio was equal to 0.36. Echoes from the second interface and the end of the sample are clearly visible. However, the signal from the first interface is rather complex, likely indicating entrapment of air at the interface or other unidentified features.

3.1.3 Medium Water-Cement Ratio Sample with Long Curing Time

The water-cement ratio equal to 0.44 was used to make the next series of samples. This ratio was chosen to be roughly an average of 0.36 and 0.5 values used with the already described samples. Our goal is to find the composition that gives an optimal trade-off between the ease of casting air free layers, which is easier to achieve with larger water content, without sacrificing the hardened strength of cementitious after curing, observed with high water content in the mixture.

The samples contained up to three layers. Each layer was equal to or less than 1 inch in thickness. The purpose of these samples was to obtain initial experimental evidence on the shortest spacing between the interfaces that does not lead to the overlap in the echo waveforms. By avoiding such overlap, the signal analysis and the measurements of the ultrasound TOF are simplified. Each layer of prepared samples in this batch was allowed to cure for a long time that varied from one day to several days before the next layer was poured.

The ultrasound testing revealed that all samples in this group produce clear internal reflections from each interface (Figure 3.7 shows the result for a 3-layer sample). The signal distortions in this and other samples prepared following this recipe (such as the two-layer samples for which the results are shown in Figures 3.8) are small, which is important for the precise measurements of the ultrasound time of flight.

3.1.4 Summary of Partial Internal Reflection Structures

Composition

We found that the samples produced using the standard Portland cement often cracked at the interface. Two new formulations were then examined to obtain a more stable refractory model.

1. In the first case, a fortifier was added to the Portland cement mixture to increase strength of the samples, adhesion between multiple layers and reduce permeability. In the following, samples prepared with this modifier are designated as PF (Portland Fortified samples).

2. Rapid Set® concrete mixture is another formulation that was tested. It produced fast setting, high strength samples, with excellent bond between layers and crack resistance. Samples prepared using Rapid Set mix are designated as RS.

Samples prepared according to these formulations have higher strength and lower permeability than samples prepared with the traditional Portland cement mix. The Rapid Set concrete samples were found to be much denser than other concrete samples. Their ultrasound waveforms are shown in Figure 3.9.

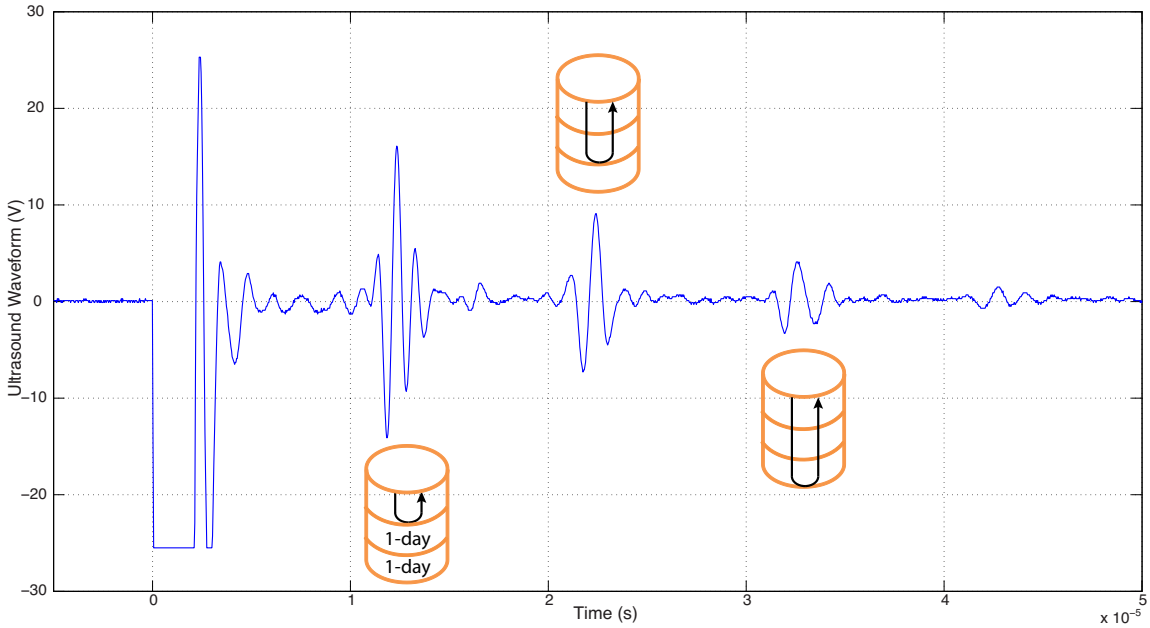

Figure 3.7: Ultrasound response for samples with two internal interfaces obtained by allowing the two initial cementitious layers to cure for 1 day each. The last layer was cured for at least 1 day. Water-cement ratio was equal to 0.44. Echoes from both interfaces are well defined, with relatively high SNR.

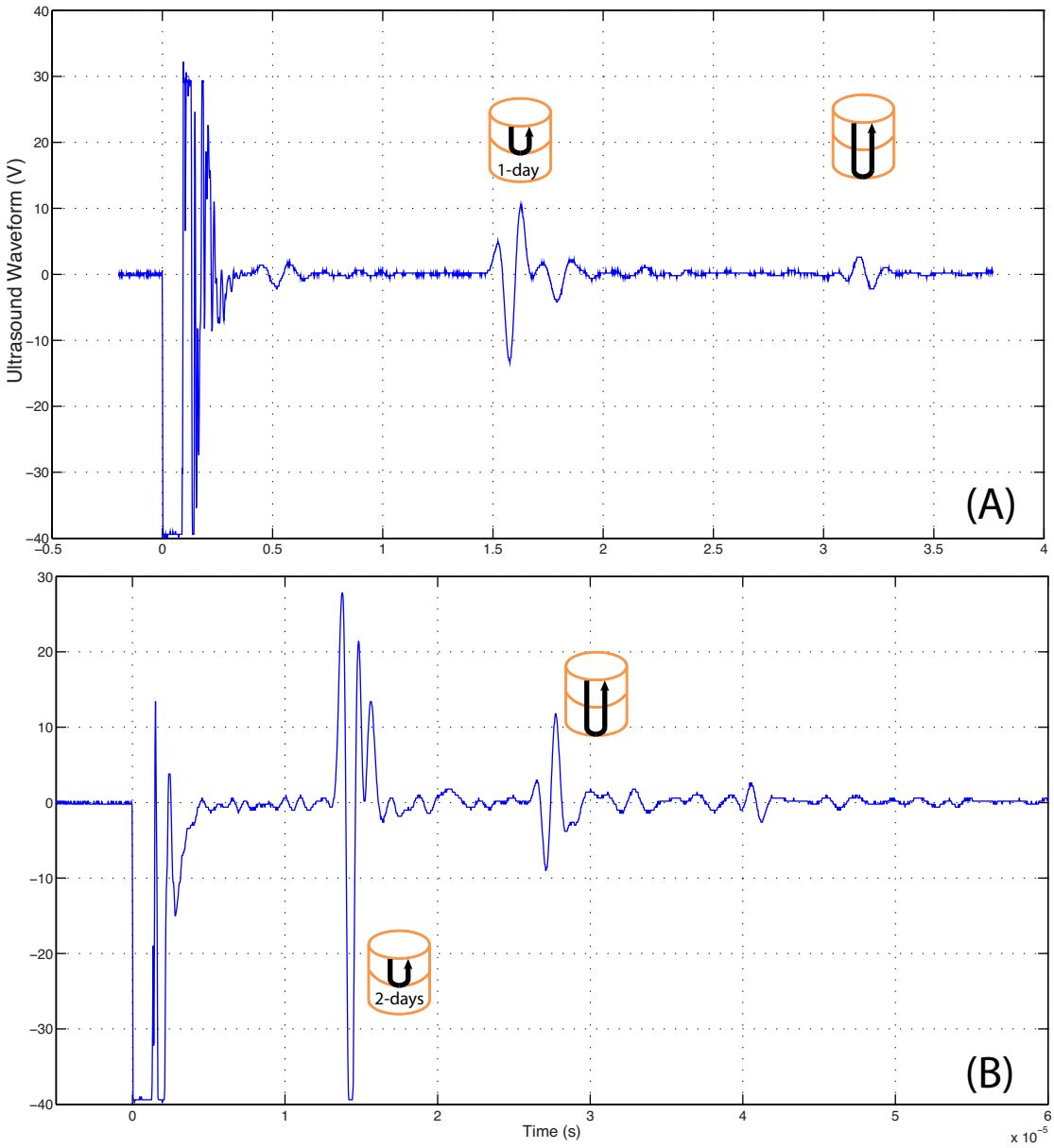

Figure 3.8: Ultrasound response for a sample with a single internal interface obtained by allowing the first cementitious layer to cure for 1 (A) or 2 days (B). Water-cement ratio equal to 0.44 was used. Echoes from the interface and the end of the sample are well defined, with a relatively high SNR.

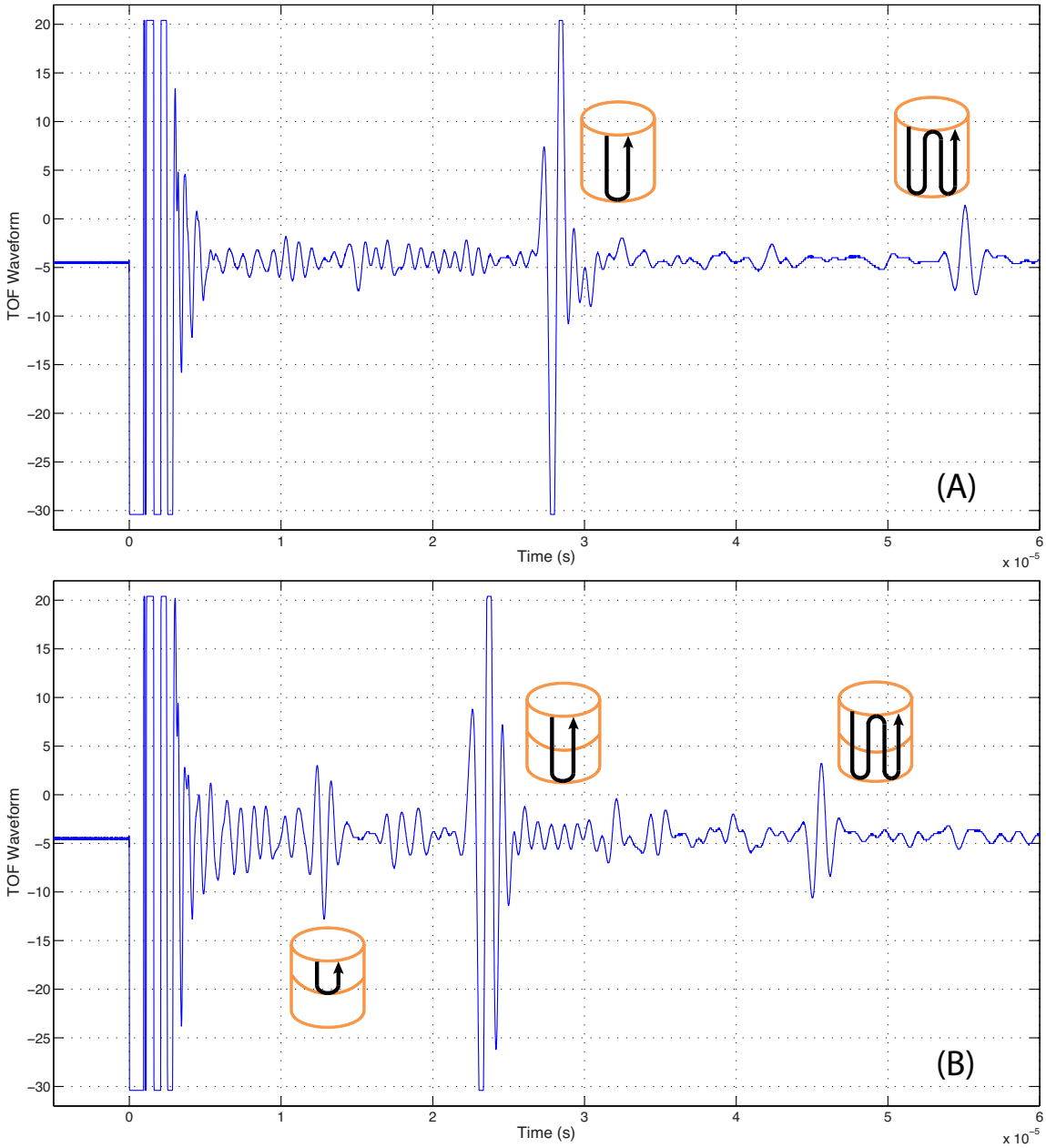

Figure 3.9: Ultrasound waveforms obtained with samples of different formulations. Panel (A) shows the results obtained with Portland Fortified cement. The results for the Rapid Set® cement sample is shown in (B). In both cases, the echoes from internal interfaces are well defined and have a relatively high SNR.

Water-cement ratio

Higher water-cement ratios lead to a better defined partial internal reflections and the measurements are characterized by higher SNRs. This is most likely due to the reduction in trapped reduced air bubbles inside samples with higher moisture content and more planar interfaces obtained with cementitious mixtures that are more "fluid." However, higher water content is associated with the reduced mechanical strength of cementitious samples. A lower water-cement ratio is known to lead to higher strength and durability, but makes it more difficult to obtain uniform planar interfaces. For a particular cement mixture used by us, a minimum of 0.25 of water-cement ratio is required for the sample to properly cure. A maximum of 0.5 of water-cement ratio was used in our experiments, which is still within the recommended range. The samples produced with an even higher water content, internal cracks and fractures are likely to form, which will reduce the strength of the cured samples.

Air bubbles

Vibration of freshly poured cement mixture (Fisher Sonic Dismembrator, Model 300, which produces 20 kHz vibrations) reduces the amount of trapped air bubbles significantly. The presence of trapped air significantly distorts the acquired echoes. At the same time, vibrating samples prior to curing previously cast layers (short cure time of 15 minutes or less) likely contributes to the lack or poor quality of echo signals produced at internal interfaces.

The partial curing time

For samples with water-cement ratio equal to 0.5 (the maximum value in the recommended range for the Portland cement used by us), the curing time of less than 1 hour produced complex reflection patterns which suggest a diffused interface between sequentially cast layers. It was found that better defined reflections are only observed on the edges of cylindrical samples but not in the samples' center. It was found that curing for at least 1 hour was necessary to obtain consistent reflections with the transducer placed in the middle of the sample. However, excessively long (over days) partial curing significantly reduces the bond between adjacent layers.

Spacing of partial reflections

We have shown that with the ultrasound excitation pulse having 1 MHz central frequency, the echoes do not overlap when the spacing between echogenic features (internal interfaces) is 1 inch or larger. The distance between the features that produce partial reflections determines the number of segments for which the temperature distribution is reconstructed. Larger number of features (and the corresponding segments) should generally

lead to a more accurate remonstration of the temperature distribution. Though only a 1 inch spacing has been demonstrated so far, a closer spacing of echogenic features may be possible with higher frequency of excitation, sharper defined interfaces, larger changes in acoustic impedance, and the more advanced signal analysis techniques that can handle overlapping echoes.

Sample length

We have demonstrated that with the standard laboratory ultrasound pulser used in the pulse-echo mode, it is possible to characterize samples at least 4 inches long and obtain clear measurements of partial internal reflections from, at least, two internal interfaces. High energy pulsers specifically designed for use with the dissipative materials would allow us to obtain temperature measurements across, at least, 12"-thick cementitious refractory.

3.2 Measurements of the temperature distribution in a cementitious sample

3.2.1 Structured Cementitious Waveguide

The experiments were conducted with a layered cementitious sample obtained by sequentially casting multiple layers and allowing for their partial curing in between. Even though the composition of each layer was identical, it was found that enough variation in acoustic impedance was introduced to create partial US reflections from the interface between the layers [36].

We used the following procedure to fabricate the waveguide. A mixture of water and Portland Type I/II cement was poured into a vertically oriented 2" ID cylindrical mold. A 4" long cementitious sample, schematically depicted in Fig. 3.10 and pictured as the insert in Fig. 3.11, was obtained by casting four 1"-thick layers of identical cement mixture and allowing for a partial cure before the next layer is cast. The mold was vibrated by an external vibrator after each pouring to ensure uniform setting of each layer and to remove air bubbles. The solidified sample was taken out of the mold and allowed to completely cure and age at ambient temperature. The waveforms of the four US echoes, produced by the three internal interfaces and the distal end of the sample, stabilized after the aging. These stable echoes, obtained at the reference temperature $T_{ref} = 20\,^{\circ}\mathrm{C}$, are shown in Fig. 3.11A.

3.2.2 Temperature Dependance of the Speed of Sound

Figure 3.12 illustrates typical ultrasound waveforms acquired when a cementation sample without internal interfaces was maintained at different uniform temperatures. The echoes

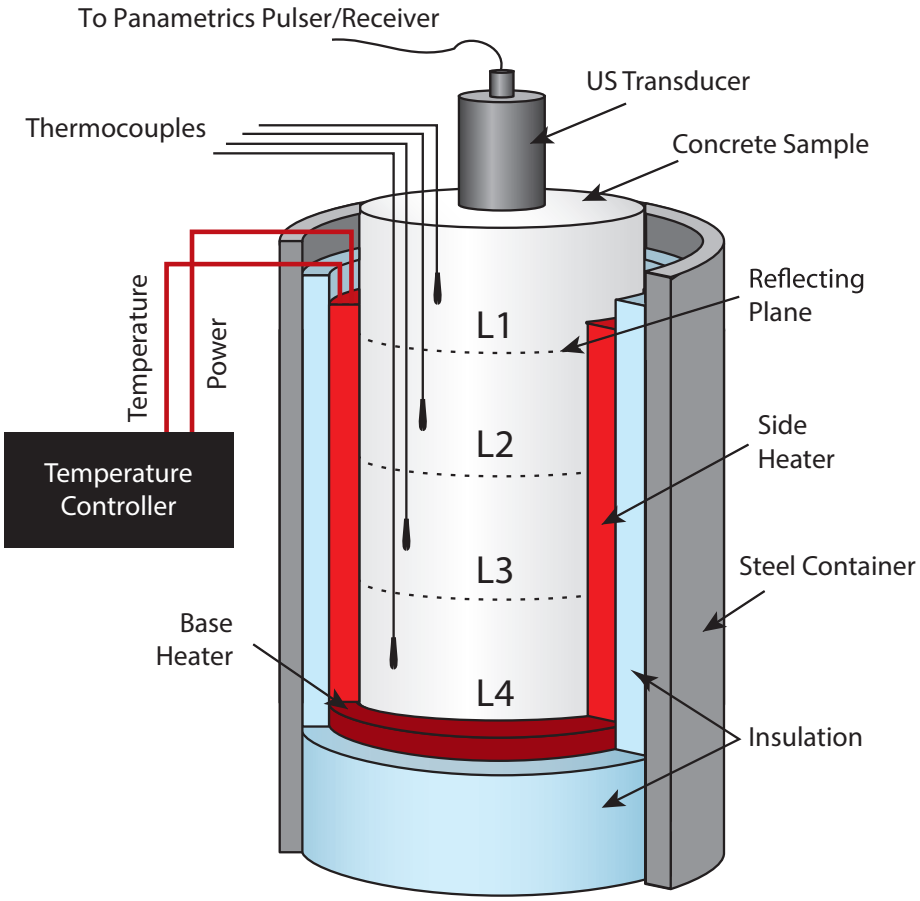

Figure 3.10: Setup used during experiments with the waveguide structured by four layers, L1...L4. During calibration experiments, layers L2–L4 were maintained at a uniform temperature controlled by the side heater. Nonuniform temperature distribution was created by using the base heater only.

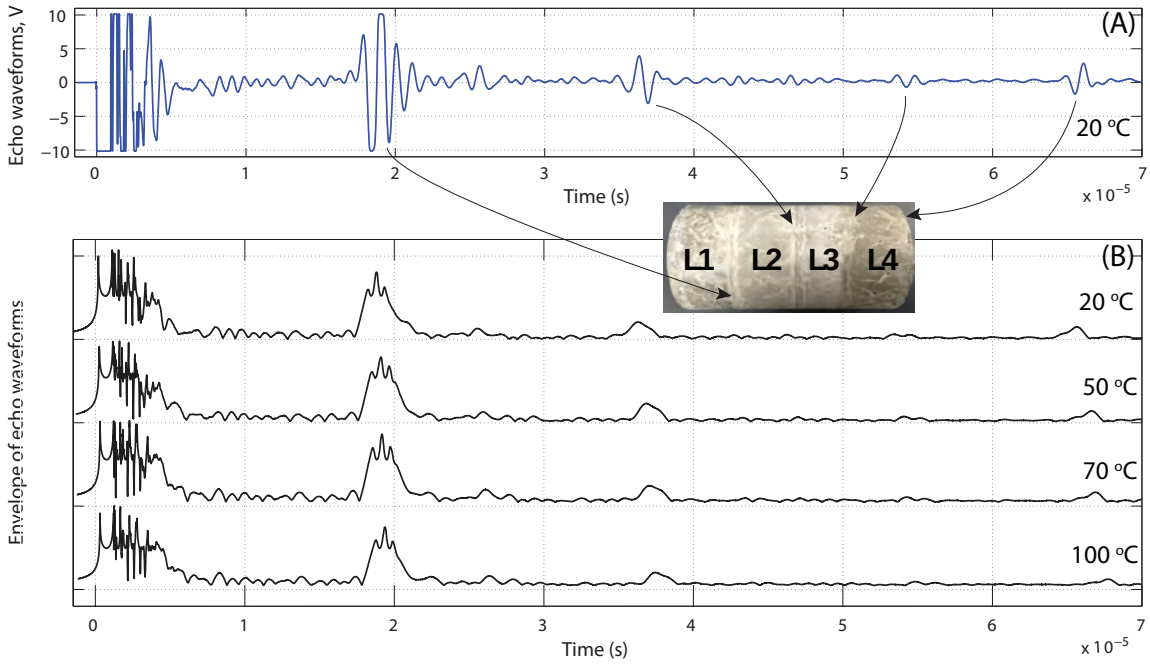

Figure 3.11: (A) Typical waveforms of ultrasound echoes created by the interface between different layers Li of the cementitious sample (insert) and the sample-air interface at its distal end. The measurements were acquired at the reference temperature of 20°C. (B) Envelopes of echo waveforms collected at different temperatures.

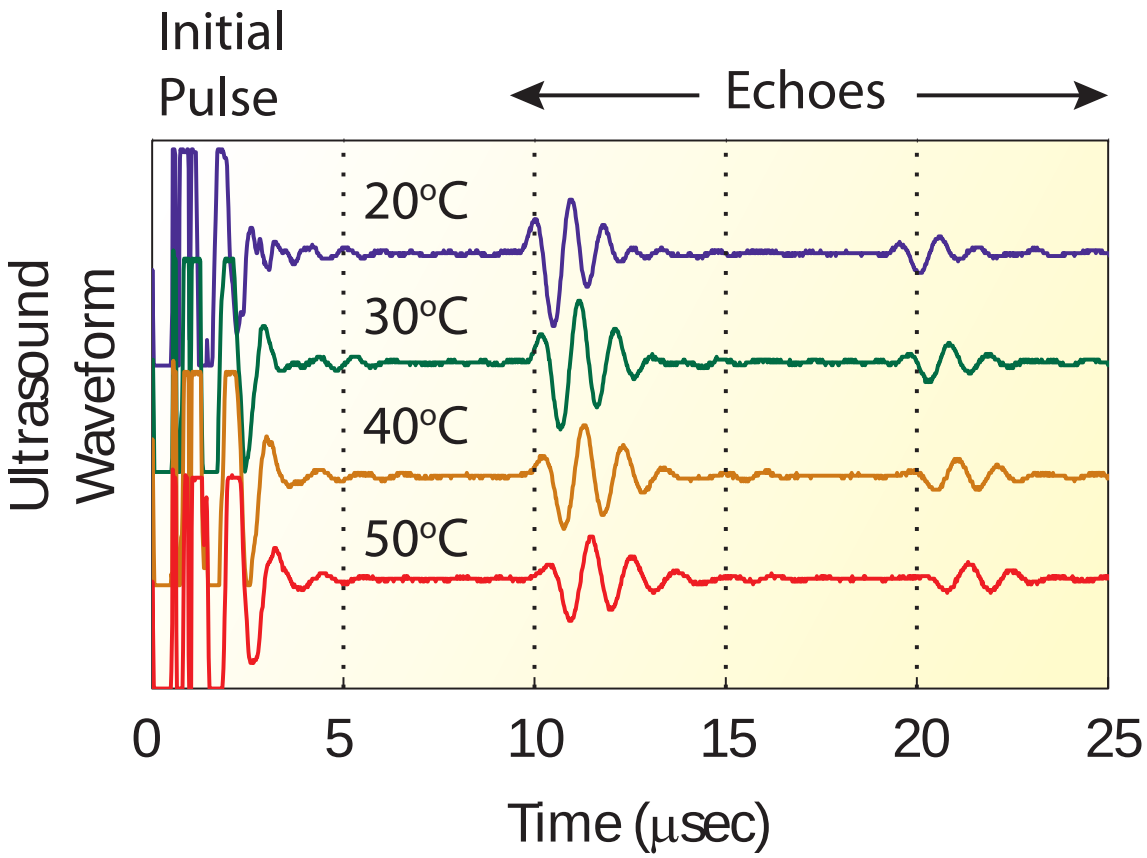

Figure 3.12: Ultrasound waveforms acquired at different temperatures illustrate the change in the TOF and the corresponding SOS with temperature.

were produced at the distal end of the sample. The first echo seen in the figure corresponds to the ultrasound pulse that traveled the length of the sample and back to the transducer (a single round trip), while the second measured echo corresponds to the same pulse after it made the second round trip through the sample. The direct inspection of waveforms in Figure 3.12 indicates that the speed of sound in the model refractory indeed depends on temperature, decreasing as the temperature goes up and leading to longer time of flight of ultrasound pulses at higher temperatures.

To establish the correlation between the speed of sound and the temperature, Eqn. (2.16), the sample was heated and maintained at different uniform temperatures inside the fabricated fixture depicted in Fig. 3.10. The heating fixture consists of a thermally insulated steel container and an internal heating blanket (silicon rubber blanket by BriskHeat®, Columbus, OH) that tightly surrounds the sample. The temperature of the heating blanket was measured by a thermocouple and controlled by a PID controller. To provide inde-

pendent measurements of the temperature on the cylindrical surface, high-temperature adhesive tape was used to attach four thermocouples (Type T, model 5TC-GG-T-30-36; OMEGA Engineering, Inc., Stamford, CT) in the middle of each layer. Two additional thermocouples were used to measure the temperature of the top and bottom surfaces of the sample. During the calibration experiments, the temperatures were changed in 10°C increments, from 20 to 100°C. After each temperature change, sufficient time was allowed for thermal equilibration to occur before attempting the US time of flight measurements.

The ultrasound tests of the cementitious sample were carried out using Panametrics pulser/receiver (model 5072PR; Olympus IMS, Waltham, MA) and Panametrics immersion transducer with a central frequency of 1 MHz (model V302). The data were acquired using an oscilloscope (Tektronix Inc., Beaverton, OR; model MSO 2024) interfaced to a computer. The ultrasound transducer was coupled to the surface of the top layer of the sample using ultrasound gel. To prevent the damage to the transducer, the top surface of Layer 1 (L1 in Fig. 3.10) extended above the fixture to allow for partial cooling of the sample; in this arrangement, Layer 1 is effectively used as a delay.

The sequence of temperatures, for which the SOS measurements were conducted, was randomized. In order to calculate the 95% confidence interval for the SOS vs. T calibration curve, tests at each temperature were repeated at least 6 times in random order. The randomization included all repeat experiments at each temperature. Such randomization lengthened the duration of the calibration experiments because the temperature no longer increased or decreased monotonically from one test point to the next, but was found to be essential in avoiding a measurement bias. During each test, 20 waveform sequences were collected and averaged. We noticed that the interface between the consecutive layers is not entirely flat or smooth (a consequence of coning, partial penetration and/or mixing between layers). To account for unevenness of the interfaces, during the repeat experiments the positioning of the transducer was slightly shifted relative to the centerline of the sample and kept at the same location for all the tests.

3.2.3 Signal Processing

Several methods for determining the TOF from the waveforms typified in Figures 3.12 were investigated. Our initial approach was to use a delay line and the echo signal from sample-delay interface as a reference "zero time" from which the time of flight is calculated. The time of flight is then calculated by matching single-point features (e.g., peak value or zero crossing) in the reference waveform from the sample-delay interface and the waveform of the reflection produced by internal interfaces and the end of the sample. Though this approach is standard, we encountered difficulties in its applications. Cementitious refractory materials are dissipative and have a higher absorption of higher frequency components of the ultrasound wave, which leads to distortion and broadening of the echo waveform and thus errors in determining the time of flight based on a single-point feature matching. We therefore opted to use the cross-correlation between the echo

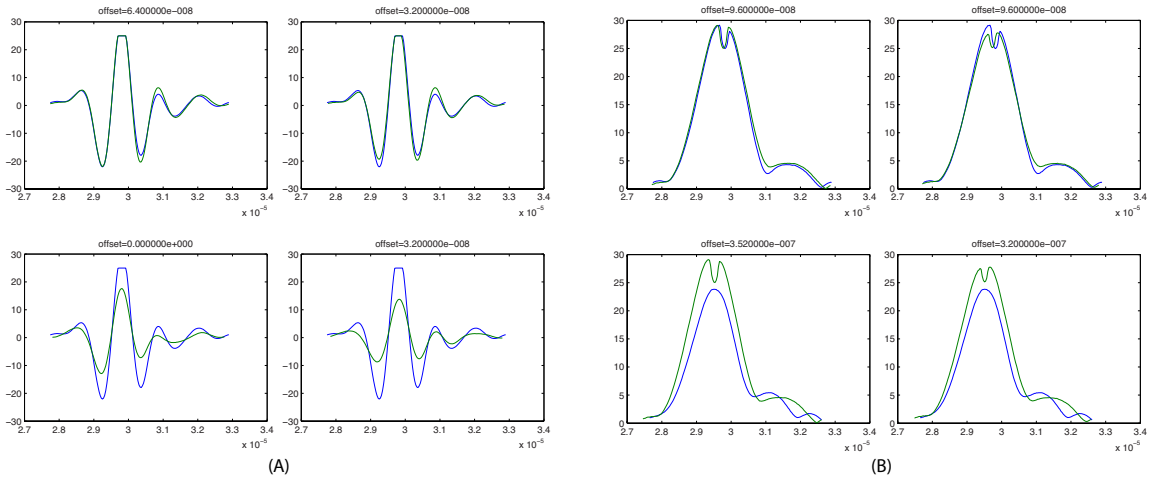

Figure 3.13: Comparison of the estimated ΔTOF (offsets) at different temperatures obtained by cross-correlating the waveforms (panel (A)) or envelopes of the waveforms (panel (B)).

waveforms obtained at different temperatures to determine the difference in the time of flight at two different temperatures, ΔTOF.

For dissipative samples higher accuracy may be obtained if cross-correlation is performed between the analytical envelopes of the waveforms, rather than the waveforms themselves [89]. To test the potential improvements, we implemented the envelope cross-correlation method and compared its performance with the TOF measurements based on the waveform cross-correlation. A numerical procedure based on the Hilbert Transform is applied to the waveform in the time domain to create an envelope of the waveform. This is a representation of the amplitude modulation on the carrier wave frequency. The procedure also creates a time-domain phase function which has application in interpreting dispersion. Figure 3.13 shows the comparison of results obtained using the cross-correlation between the waveforms (left 2 columns) and the envelopes of the waveforms. The offsets (ΔTOF) between the reference waveform and its envelope (green lines) and the waveforms and their envelopes of the echo signals acquired when the sample was maintained at different temperatures (blue lines) are listed for each subfigure. The two methods give a similar trend of increasing time of flight with temperature but differ in values of ΔTOF. In further analysis, the envelope cross-correlation method is used as an approach less sensitive to the waveform distortion.

The envelope of the echo waveforms in Figure 3.11A (collected when the sample was maintained at the uniform reference temperature of 20 °C) is shown as the top graph in Figure 3.11B. The remaining graphs in Figure 3.11B show the envelopes of the waveforms collected during the calibration experiments when the sample was maintained at the elevated uniform temperatures (results for 50, 70, and 100 °C are shown). Visual comparison

of the envelopes indicates a distinct trend towards an increased TOF as the temperature increases, and therefore the reduction in the speed of sound c through the sample at elevated temperatures.

The overall procedure for the data analysis using the envelope cross-correlation method and the speed of sound calculation is summarized in the following steps:

1. The reference zero time (or trigger) is maintained the same for all measurements.

2. The reference waveforms, which include 4 echoes from the three internal interfaces and the distal end of the sample, are acquired at the reference temperature, selected to be 20 °C.

3. The temperature tests are conducted in random order, with at least 6 repeats for each temperature. During each test, 20 waveform sequences are collected and averaged.

4. The envelope cross-correlation between the reference and the averaged waveforms is applied to find ΔTOF at a given temperature relative to the reference temperature of 20 °C.

   The change in the time of flight of an echo produced by i-th internal interface relative to the TOF at the reference temperature T_{20} is equal to

   $$\Delta t_{of}^{z_i}(T) = t_{of}^{z_i}(T_{20}) - t_{of}^{z_i}(T) = 2\left[\frac{z_i}{c(T_{20})} - \frac{z_i}{c(T)}\right]. \tag{3.1}$$

   To quantify $\Delta t_{of}^{z_i}(T)$ from the ultrasound measurements, we used the cross-correlation of the waveform envelope, A_T, of an echo obtained at the temperature T with the corresponding echo acquired at the reference temperature, T_{20}:

   $$A_{T_{20}} \star A_T = \int_{-\infty}^{+\infty} A_{T_{20}}(t) A_T(t+\tau) dt. \tag{3.2}$$

   The temperature-induced change in the TOF is then obtained as a delay (shift) τ between $A_{T_{20}}$ and A_T needed to maximize their cross-correlation. Formally, for i-th echo we find $\Delta t_{of}^{z_i}(T)$ as the solution of the following problem:

   $$\Delta t_{of}^{z_i}(T) = \text{argmax}_\tau \int_{-\infty}^{+\infty} A_{T_{20}}(t) A_T(t+\tau) dt. \tag{3.3}$$

5. The speed of sound $c_1, \ldots, c_4$ in each layer of the sample is calculated at each temper-

ature:

$$c_1 = \frac{2L_1}{\left(t_{of_1}(T_{20})\right) + \left(\Delta t_{of}^{L_1}(T)\right)}, \tag{3.4}$$

$$c_2 = \frac{2L_2}{\left(t_{of_2}(T_{20}) - t_{of_1}(T_{20})\right) + \left(\Delta t_{of}^{L_2}(T) - \Delta t_{of}^{L_1}(T)\right)}, \tag{3.5}$$

$$c_3 = \frac{2L_3}{\left(t_{of_3}(T_{20}) - t_{of_2}(T_{20})\right) + \left(\Delta t_{of}^{L_3}(T) - \Delta t_{of}^{L_2}(T)\right)}, \tag{3.6}$$

$$c_4 = \frac{2L_4}{\left(t_{of_4}(T_{20}) - t_{of_3}(T_{20})\right) + \left(\Delta t_{of}^{L_4}(T) - \Delta t_{of}^{L_3}(T)\right)}, \tag{3.7}$$

where $L_1 \ldots, L_4$ are the thicknesses of each layer; $t_{of_1}(T_{20}), \ldots, t_{of_4}(T_{20})$ are the times of flight of reference echoes originating from the three internal interfaces and the distal end of the sample; $\Delta t_{of}^{L_1}(T), \ldots, \left(\Delta t_{of}^{L_4}(T) - \Delta t_{of}^{L_3}(T)\right)$ are the differences between time of flights at reference and test temperatures. The overall length of the sample, $L = \sum_{i=1}^{4} L_i$, was measured using a micrometer, and the speed of sound at the reference temperature was calculated using Equation 2.4, where TOF is equal to $t_{of_4}(T_{20})$ which is the time of flight of the echo produced at the distal end of the sample. With known speed of sound at the reference conditions, the thicknesses of each layer L_i were calculated using the measurements of $t_{of_1}(T_{20}), \ldots, t_{of_4}(T_{20})$.

3.3 Results

3.3.1 Calibration: SOS as a function of Temperature

The correlation between the speed of sound that the temperature was obtained using the ultrasound measurements obtained when the sample was maintained at a known uniform temperature, T. The following equation (3.8) (the generalization of equations in Step 5 of the signal processing algorithm) was used to calculate the SOS in different segments of the waveguide,

$$c_i = \frac{2(z_i - z_{i-1})}{t_{of_i}(T)} = \frac{2(z_i - z_{i-1})}{\left(t_{of_i}(T_{ref}) - t_{of_{i-1}}(T_{ref})\right) + \left(\Delta t_{of}^{z_i}(T) - \Delta t_{of}^{z_{i-1}}(T)\right)}. \tag{3.8}$$

where z_i is the spacial location of the i-th echogenic feature (transducer is located at $z = 0$) and $t_{of_i}(T)$ was determined following the described signal analysis procedure. The result for all four layers is shown in Fig. 3.14. Data points in this figure are based on the SOS

measurements repeated 6 times. For different layers, this figure shows the average SOS in repeated experiments as a function of the temperature measured by a thermocouple attached to the middle of the corresponding layer. The linear regression of the data points for all layers has the following form:

$$c = f(T) = -1.06T + 3240.3, \quad 20\,^{\circ}\mathrm{C} \leq T \leq 100\,^{\circ}\mathrm{C} \tag{3.9}$$

and is also shown in Fig. 3.14. The shaded area indicates the 95% confidence interval for this regression.

The subsequent results of this Chapter, demonstrating the application of the US-MSTD method with the described cementitious sample, use the SOS vs. temperature relationship depicted in Fig. 3.14 and described by equation 3.9. Of separate interest, is the effect of the cement composition and the curing recipe have on this relationship. To investigate this question, six additional cementitious samples, summarized in Table 3.1, were tested in a temperature controlled water bath in the range 20 to 50 °C with 5 °C increments. During the experiments, all 2-inch samples (contain a single internal interface formed by two layers) were fully immersed under water, while 3-inch, and 4-inch samples were partially protruding above the water surface. Only the time of flight measurements corresponding to the two sections immersed under water were used to obtain the calibration curve. The echoes from the first and second partial internal reflectors, respectively, were used as delay line reference to measure the time of flight from the immersed sections.

Six sets of randomized tests for samples 1, 2, 5, and 6, and 3 sets for samples 3 and 4 were obtained for determining the relationship between the SOS and the temperature. Figure 3.15 summarizes the results for all samples. The speed of sound in the denser Rapid Set sample is noticeably higher. Overall, as temperature changes from 20 to 50 °C, the speed of sound in all samples linearly decreases by 2.23% in the RS sample to 4.32% in the PF sample. The curing time has some effect on the speed of sound in the standard Portland cement samples but its change with temperature remains consistent.

3.3.2 Estimated temperature distribution

After obtaining the calibration curve, the proposed method was applied to the measurement of non-uniform temperature distribution established in the sample by heating it from the bottom using the base heater shown in Fig. 3.10. After the temperature measurements provided by surface thermocouples stabilized at constant values, an ultrasound excitation pulse was applied to the sample and four return echoes were acquired. For each segment of the waveguide, the envelope cross-correlation of the echo waveforms was used to calculate the value of $t_{of_i}(T)$ in the left-hand-side of Eqn. (3.10):

$$t_{of_i}(T) = \left(t_{of_i}(T_{ref}) - t_{of_{i-1}}(T_{ref})\right) + \left(\Delta t_{of}^{z_i}(T) - \Delta t_{of}^{z_{i-1}}(T)\right) = 2\int_{z_{i-1}}^{z_i} \frac{1}{f(T(z))} dz, \tag{3.10}$$

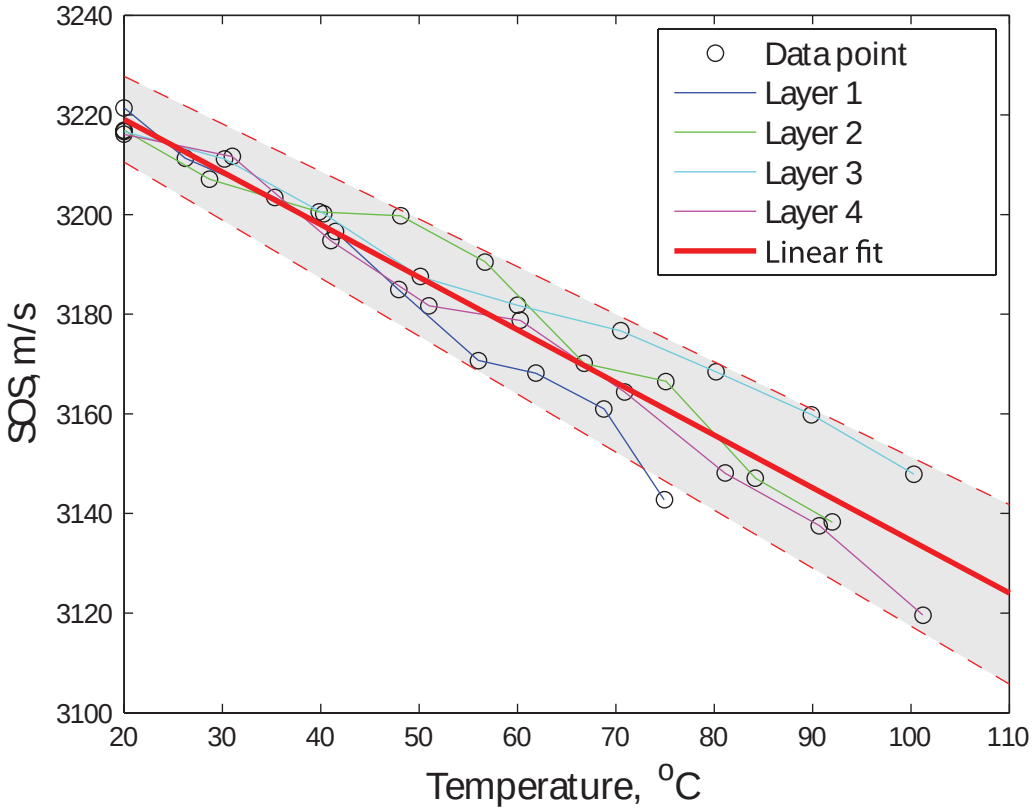

Figure 3.14: Calibration results for the speed of sound as a function of temperature. The SOS in different segments (layers of the waveguide) was calculated from the measurements of the change in the time of flight of the four echoes produced by the structured waveguide, relative to their TOF at the reference temperature $T_{ref} = 20\,^{\circ}\mathrm{C}$. The shown linear fit $c = f(T)$ is based on the data for all layers. The shaded area gives the 95% confidence interval for the obtained linear fit.

Table 3.1: Cementitious samples used during SOS vs. temperature testing

Sample	Length (in)	Cement type	Numbers of Internal interfaces	Curing time between conceptive layers (mins)
1	2	Portland I/II	1	15
2	2	Portland I/II	1	60
3	2	Portland I/II Fortified	1	60
4	2	Rapid Set	1	60
5	3	Portland I/II	2	30
6	4	Portland I/II	3	60

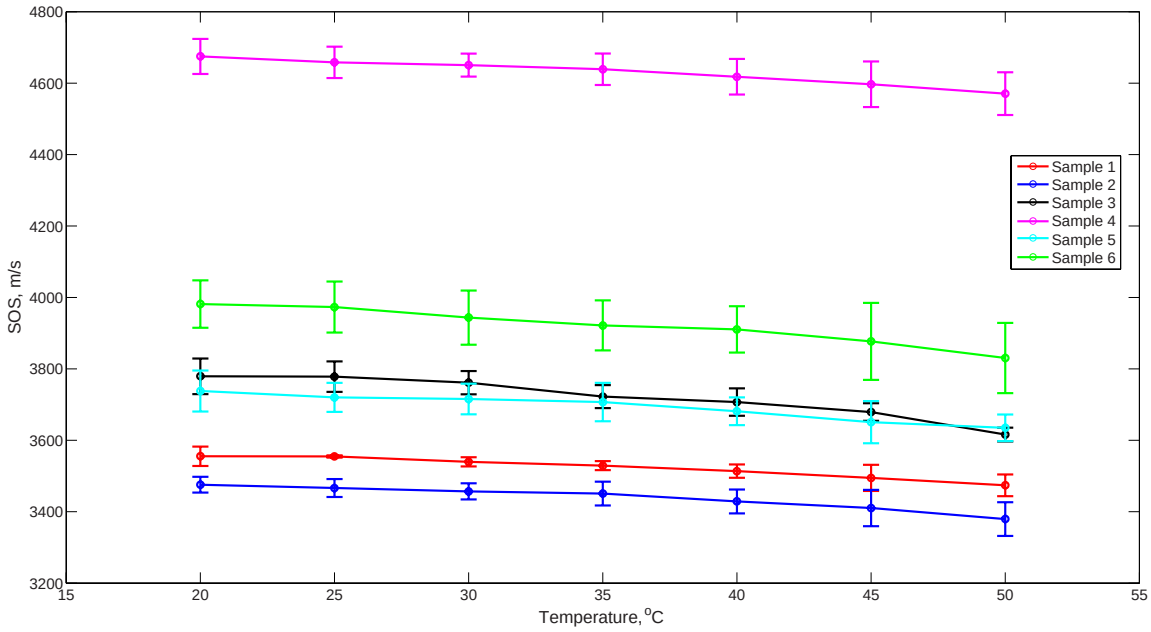

Figure 3.15: The speed of sound as the function of temperature for six cementitious samples, varying in composition and curing time, shows an approximately linear relationship in the investigated range of temperatures.

The estimation of unknown $T(z)$ was then obtained under different parameterizations of the temperature distribution. In each case, the parameters defining the distribution were selected to satisfy Eqn. (3.10) exactly or with the smallest possible error.

Piecewise Constant Distribution

The assumption of constant temperature in each segment, coupled with the calibration Eqn. (3.9), gives the piecewise constant estimation of $T(z)$, with the temperature in the i-th segment equal to

$$T_i = 3056.89 - \frac{1.89(z_i - z_{i-1})}{t_{of_i}}. \tag{3.11}$$

This piecewise constant parametrization was previously used in [36], and is included in Figure 3.16(A), for comparison. The thermocouple measurements of the surface temperature in the middle of each segment are also shown. Though this simplest possible parametrization exhibits a discontinuous change in the estimated temperature at the location of echogenic features, it is still able to capture the correct trend in the temperature distribution along the sample. If we approximate an axial thermal flux as $q_i \approx -k\frac{T_i - T_{i-1}}{z_1 - z_{i-1}}$, the obtained result is comparable to the flux estimated based on the thermocouple measurements.

Piecewise Linear Distribution

The assumption of a linearly changing temperature within each segment parameterizes the temperature distribution in the i-th segment as

$$T_i(z) = m_i z + n_i, \tag{3.12}$$

where m_i and n_i are unknown parameters. Coupled with the linear relationship between the speed of sound and the temperature (equation 3.9), this parametrization, when used in Equation 2.21, results in the following equation in unknown m_i and n_i:

$$t_{of_i} = a \int_{z_{i-1}}^{z_i} \frac{1}{a(m_i z + n_i) + b} dz \tag{3.13}$$

where $a = -1.06$ and $b = 3240.3$ from the linear relationship (3.9). After performing the integration and by requiring that the temperature remains continuous at the boundary of two adjacent segments, the following two equations for determining the slope m_i and the intercept n_i are obtained:

$$t_{of_i} = \frac{2}{am_i} \ln\left[a(m_i z + n_i) + b\right]_{z_i}^{z_{i+1}} \tag{3.14}$$

$$m_i z_i + n_i = m_{i-1} z_i + n_{i-1} \tag{3.15}$$

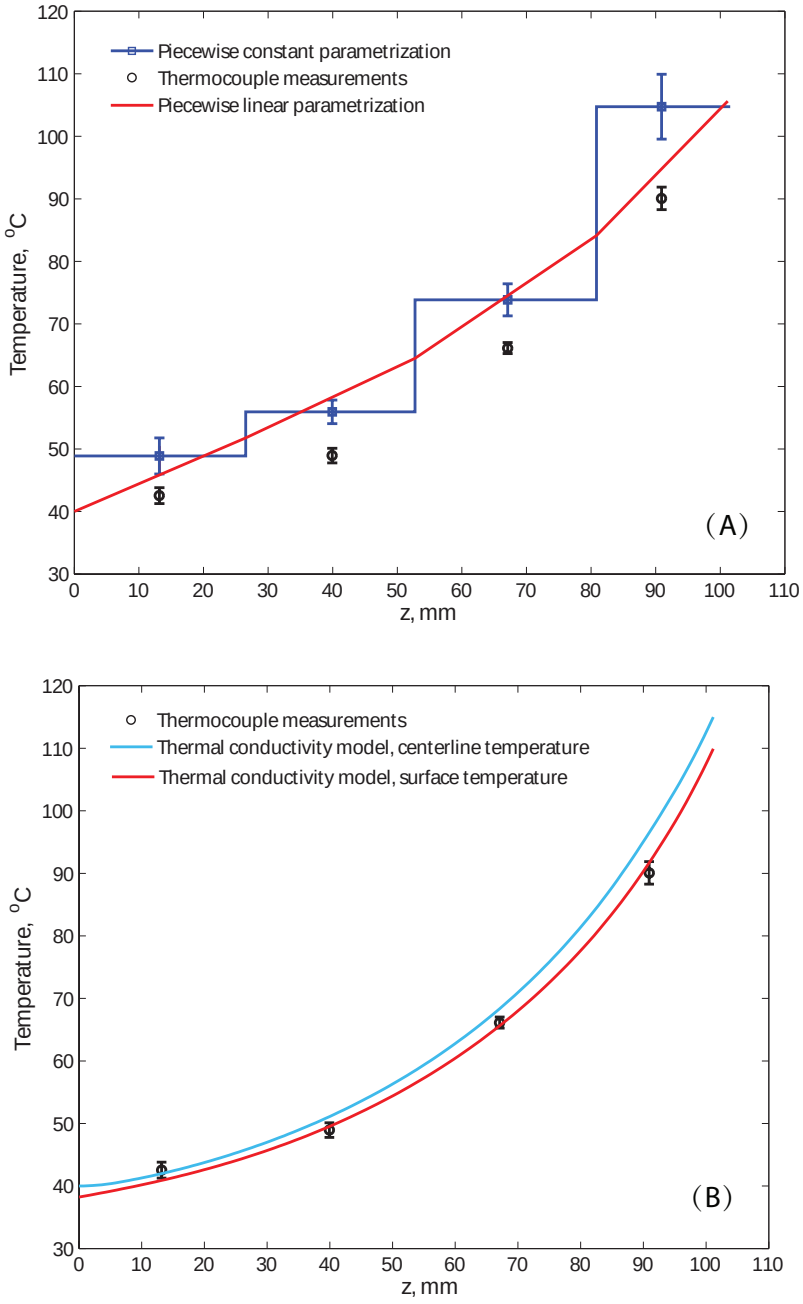

Figure 3.16: (A) Estimated temperature distributions based on piecewise constant and piecewise linear parameterizations are compared with the measurements of the surface temperature obtained with thermocouples attached in the middle of each segment. (B) The parametrization based on two-dimensional thermal conductivity model can be used to estimate the temperature distribution along the centerline and the surface of the waveguide.

Note that $n_1 = T(0)$, where $T(0)$ is the temperature at the transducer location. If we assume that $T(0)$ is measured independently, then the combination of equations (3.14) and (4.16) with similar equations for other segments of the waveguide provides us with sufficient number of conditions to find the piecewise linear temperature distribution across the entire waveguide.

For the four segments of the waveguide used in our experiments, the estimated piecewise linear temperature distribution is shown in Fig. 3.16(A). Though an improvement over the piecewise constant distribution, a substantial difference ($\sim 10\,^{\circ}$C at $z = 40$ mm) with the thermocouple measurements is still apparent. The simplification inherent in the assumption of the linear temperature profile can partially explain this observation. The difference may also be, at least partially, explained by lower surface temperatures, measured by the thermocouples compared, to higher internal temperatures which influence noninvasive ultrasound measurements. To quantify the difference between surface and internal temperatures, a model that accounts for the heat loss through a cylindrical surface of the waveguide must be used.

3.3.3 Parametrization with 2D Thermal Conductivity Model

A much more accurate estimate of the temperature distribution will be obtained if a more realistic "sub-grid" parametrization is used. For example, we expect that by requiring that the temperature distribution satisfies the realistic heat transport model (e.g., the conduction model of Equation 3.16 supplemented with the boundary temperature condition at the transducer's location), the accuracy of the temperature distribution based on ultrasound measurement and the estimation of the hot boundary temperature will improve.

The following two-dimension heat conduction model accounts for the radial heat loss through the walls of the test fixture:

$$\rho C_p \frac{\partial T}{\partial t} = k\left(\frac{1}{r}\frac{\partial}{\partial r} r \frac{\partial T}{\partial r}\right) + \frac{\partial^2 T}{\partial z^2}. \tag{3.16}$$

It was implemented in COMSOL Multiphysics (COMSOL, Inc., Burlington, MA) modeling software using the following model parameters for the cementitious sample: $\rho = 1{,}200\,\mathrm{kg/m^3}$ (measured value); $k = 26.91105 - 0.2477056T + 8.606168\times10^{-4}T^2 - 1.00482\times 10^{-6}T^3$ (Comsol database), and $C_p = 1.55$ kJ/(kg K). The temperature of the proximal and distal ends of the waveguide and the heat flux through its cylindrical surface were used as the three boundary conditions needed to completely define the model. Temperature distributions on the end surfaces of the waveguide were assumed to decrease linearly from the centerline ($r = 0$) to its cylindrical edge ($r = 25.4$ mm). The centerline and edge temperatures were estimated using the following procedure. The thermal image of the "cold" proximal end of waveguide ($z = 0$; Figure 3.17A), to which the US transducer was coupled, was acquired with an infrared camera (model T300, FLIR Systems, Inc., Wilsonville, OR).

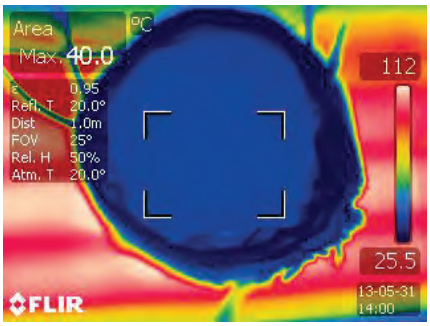

(A)

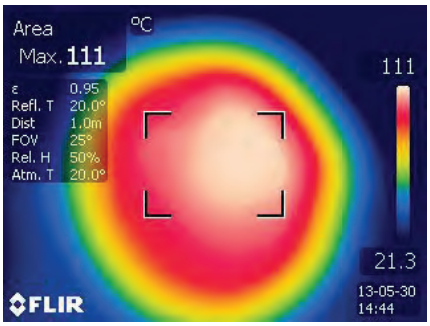

(B)

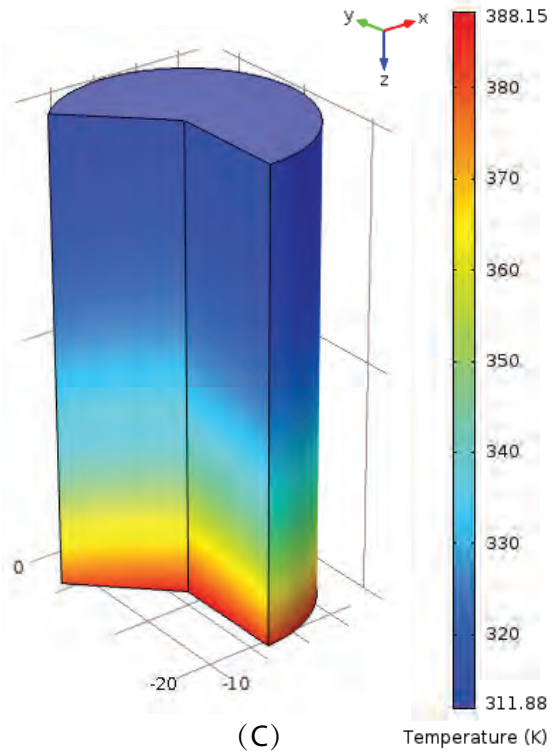

(C)

Figure 3.17: (A) and (B) show thermal images of the proximal and distal ends of the waveguide. Temperature distribution in the waveguide predicted by the two-dimensional heat conduction model is shown in (C).

Based on thermal images in three repeat experiments, the centerline and the edge temperatures of the cold surface were found to be $T(0,0) = 40\,^{\circ}\text{C}$ and $T(0,25.4) = 38.73\,^{\circ}\text{C}$. To characterize the temperature distribution of the hot end (in contact with the base heater, Fig. 3.10), the waveguide was quickly removed from the test fixture to take a thermal image (Fig. 3.17B). Based on three repeat experiments, it was found that $T(101.6,0) = 115\,^{\circ}\text{C}$ and $T(101.6,25.4) = 109.92\,^{\circ}\text{C}$. The estimated centerline temperature of the hot end was verified by the thermocouple measurements, and was found to be in good agreement with the imaging results.

The heat transfer coefficient h in the third boundary condition, Eqn. (2.35), was selected to match the measured segmental time of flights and the surface temperatures acquired by four thermocouples shown in Fig. 3.10. Figure 3.17(C) shows the temperature distribution in the waveguide obtained with $h = 14$ W/(m$^2\cdot$ K). The centerline temperature distribu-

tion, $T(z,0) = T(z)$, was used in the measurement equations (2.18) and (2.20) to calculate the overall and segmental times of flight of ultrasound echoes. The comparison of the predictions with the measured values shows less than 1% relative difference for all TOFs. Fig. 3.16(B) compares the centerline and surface temperature distributions, $T(z,0)$ and $T(z,25.4)$, with the thermocouple measurements of the surface temperatures. The results show that the centerline temperature is indeed higher than the surface temperature by as much as 7°C, and the difference between the estimated surface temperature and the thermocouple measurements is less than 2°C.

Chapter 4

High Temperature Laboratory Experiments

4.1 Alumina Refractories

The ultrasound studies with the cementitious samples proved the feasibility of the ultrasound measurements of segmental temperature distribution. However, the application of the US-MSTD method at temperatures and conditions representative of industrial-scale combustors and gasifiers, a more appropriate refractory model must be selected. due to the temperature limitation of cementitious material, advanced ceramic that is more resistant to corrosive environment, suitable for elevated temperature application, is required.

Alumina (Al_2O_3) is one of the most widely used general purpose technical ceramics for high-temperature applications. Alumina ceramic is hard, wear resistant, and has high compressive strength, even at very high temperatures (up to 1750°C). Compared to other oxide ceramics at high temperatures, alumina (Al_2O_3) provides better corrosion protection. Aluminas are also excellent electrical insulators, and can be fabricated with very low porosity and gas tight. Dopants, such as MgO and CaO, may be added to improve its performance characteristics, such hardness, strength, and thermal properties. These additives can slow the growth of alumina grains at higher temperature, which is desirable in ultrasound applications in order to reduce the signal attenuation.

4.1.1 Castable Alumina

Several castable alumina candidates were tested. GREENCAST®-94 PLUS is a high alumina, low silica castable ceramic, produced by APGreen. Its major ingredients are alumina (94.1% Al_2O_3) and Lime (5.1% CaO). This material may be used at a temperature up to 1,870°C. We continued to use our vibrating system to help the mixture flow and settle in the molds with minimum voids. However, because of high viscosity/low "fluidity" of

this mixture, it trapped air bubbles which were not possible to remove by simple vibrations. Several other issues were encountered with this ceramic. First, the lime appears as small-size gravel, about 2–4 mm in diameter. These particles reflect and dissipate the ultrasound signal. Second, the ceramic contains fibers, often clumped together, which are normally added to increase the crack resistance, elongation and thermal shock resistance in ceramic applications. However, clusters of this fibrous material absorb the US energy and limit the length of the ultrasound preparation to below 2 inches under the conditions of our experiments.

To get a better ultrasound signal for this type of ceramic sample, we sieved the large clumps of fiber out of the ceramic mix and crushed down bulky grains. Tests showed that ultrasound signal improved for the modified sample. We were able to measure reflection (return echoes) from 3 inch long samples. Still, the strength of the reflected signal was weak and distorted.

We proceeded to test high temperature ceramics from Cotronics, Corp. that do not contain fibers or large grains, such as zirconium oxide and alumina oxide castable ceramics. We tried to use the same method to create partial reflection as we used with cementitious materials by cascading ceramic at multiple times with a partial cure allowed after each layer was cast. However, a significant number of air bubbles left inside after drying distorted and weakened the ultrasound echo even after experimenting with different ways of vibrating the mixture. It appears that pressure casting, for which we did not have appropriate equipment, is essential in obtaining uniform void-free samples.

One example of ultrasound waveform from 4-inch and 5-inch lab cascade alumina ceramic samples tested using 1 MHz transducer (Panametrics V302) is shown as Figures 4.1. Because the length of the refractory inserted into the gasifier would be between 4 to 10 inches, we continued to search for the right ceramic material and the proper method to create strong and clear partial reflections from known positions inside the waveguide.

4.1.2 Machinable Alumina

Recognizing that the limitations of our casting process likely contributes to poor quality of samples, we settled on precast, pressure formed, machinable alumina ceramics provided by an external supplier. Specifically, we purchased a precast pressure formed alumina rod 1 inch in diameter and 12 inches long. The supplier specified that these samples are rated for continuous use up to 3000 °F (1649 °C).

Figure 4.2 shows the ultrasound waveform of the ceramic rod without echogenic features. The echo from its distal end appears between 140 and 160 μs. The echoes appearing after 160 μs were likely caused by multiple transmission modes present due to secondary reflections of the ultrasound pulse from the cylindrical surface of the waveguide, as conceptualized in Figure 4.3. Such modes are only when the length of the waveguide is significantly larger than its diameter. The reflection of at the cylindrical surface may also lead to a small percentage of mode conversion from longitudinal waves to shear wave [61],

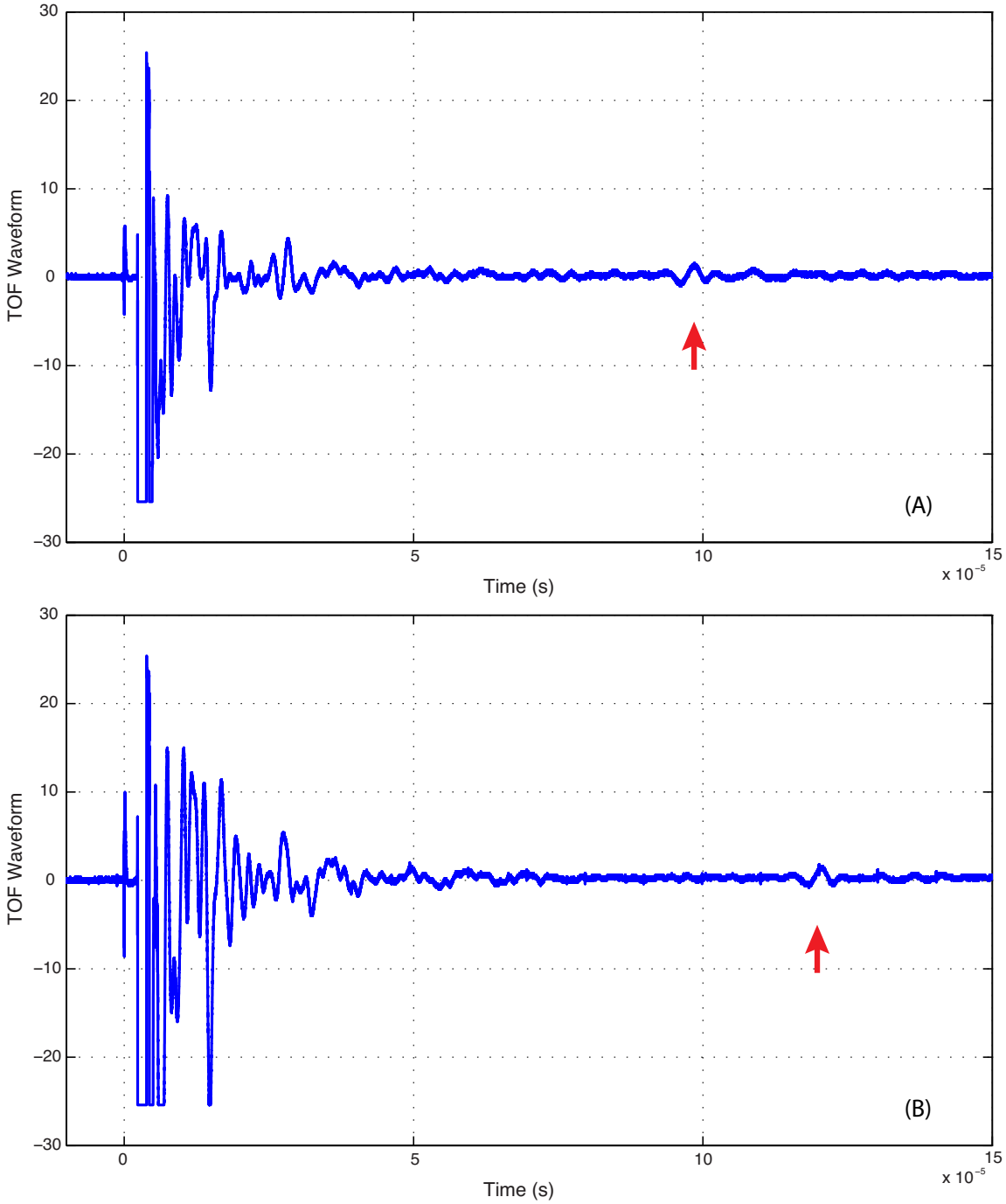

Figure 4.1: The ultrasound waveforms acquired from 4-inch and 5-inch alumina samples. Echo signals are seen at approximately 10 and 12 microseconds.

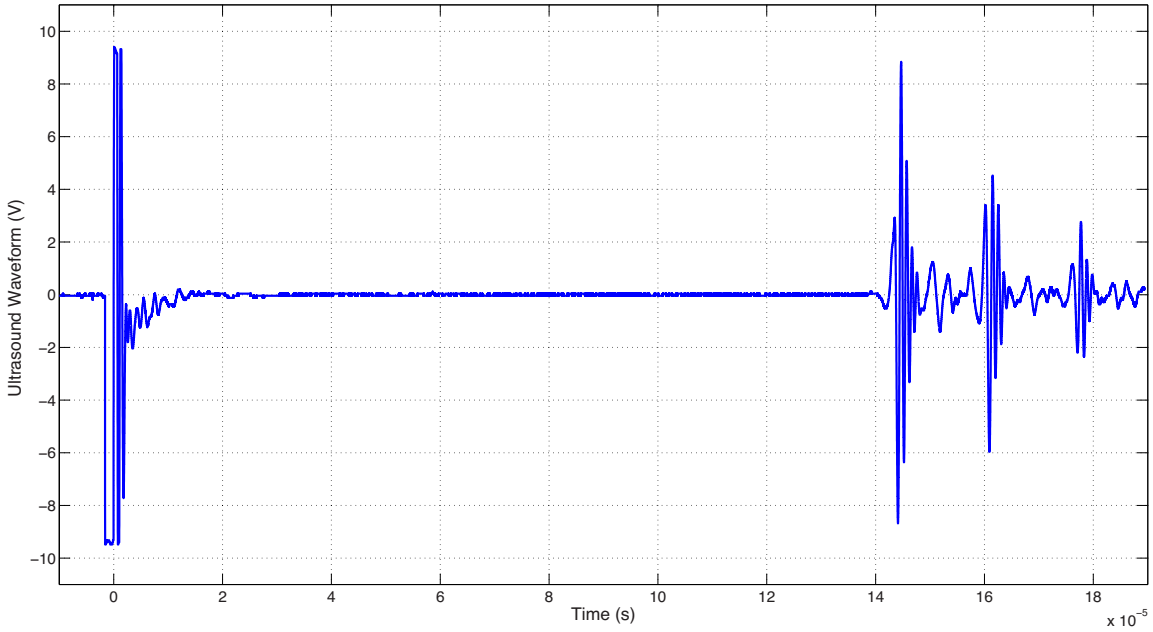

Figure 4.2: The ultrasound waveform for 1"×12" alumina rod shows multiple echoes produced by the reflections from the distal end of the waveguide. The data were obtained with the transducer having a 1 MHz central frequency.

which have a smaller velocity of propagation and, thus, would after p-wave echoes.

4.2 Experiments

4.2.1 Introduction of Echogenic Features

After experimenting with different solutions, we found a simple method to introduce echogenic features at predetermined spatial locations along the length of the ultrasound propagation, which involves drilling small holes normal to the surface of the waveguide. To balance the strength of the return echo signal from echogenic features, which improves

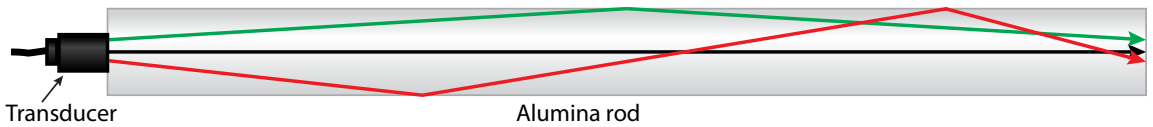

Figure 4.3: Schematic depiction of multiple modes responsible for an observed multiple echoes from the distal end of the waveguide.

Figure 4.4: Three 3/32-inch holes were drilled into the precast alumina rod at 2, 4, and 6 inches away from its distal end.

with larger hole sizes, while maintaining physical integrity of the waveguide, after some experimentation we settled at drilling 3/32-inch holes into the waveguide. Figure 4.4 shows a 12" waveguide with three 3/32" holes were drilled 2, 4, and 6 inches from its distal end. In this arrangement, the waveguide is segmented into four segments for which the temperature distribution can be determined.

4.2.2 Frequency selection

For high density, high hardness alumina ceramic, ultrasonic testing showed that frequencies in the megahertz regime are necessary to generate wavelengths as small as the microstructure features [90]. We tested the alumina waveguide at several ultrasound frequencies, including 0.5, 1, 5, and 10 MHz. The representative results are shown in Figure 4.5. Since the wavelength of 0.5 MHz transducer is ~0.022 m, which is close to the diameter of a 3/32" hole, clear partial reflections from hole locations were not produced due to ultrasound diffraction. The three echoes in the center in Figures 4.5 (b)–(d) are produced by the introduced echogenic holes. Further examination of the results in Figure 4.5 indicates that 1 MHz and 5 MHz transducers produced an acceptably clear response. A 5 MHz transducer produced the cleanest echo signals with the highest SNR. A 10 MHz transducer has higher spatial resolution but shows an expected higher attenuation of the ultrasound signal.

Our experiments show that alumina provides good ultrasound propagation at temperatures up to 800 °C for continuous use. It remains an acceptable ultrasound waveguide when temperatures exceed 1000 °C for a short term. However, the strength of the ultrasound signal degrades significantly when temperatures stay above 800 °C for a long time, discussed later in this report.

4.2.3 Experimental Setup

Carbolite 1 & 3 Zone Wire-Wound Tube Furnace (model MTF 201) was used in laboratory-scale ultrasound tests. This furnace is capable of operating at temperatures up to 1200 °C and provides convenient observation and access to all power and temperature controls. This tube furnace incorporates low thermal mass ceramic fiber insulation for fast response times and rapid heat-up to the operating temperature. Furnace controls are built into the

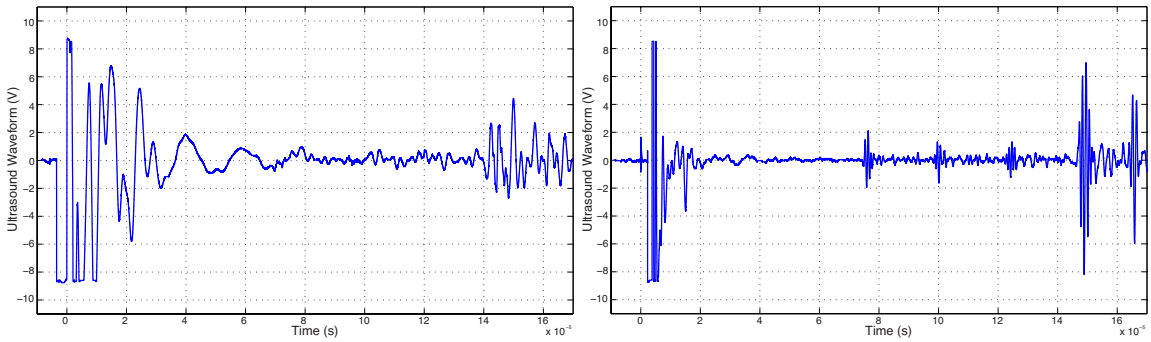

(a) Transducer V601 with frequency 0.5 MHz

(b) Transducer V603 with frequency 1 MHz

(c) Transducer V609 with frequency 5 MHz

(d) Transducer V611 with frequency 10 MHz

Figure 4.5: The ultrasound echo waveforms obtained with transducers of different central frequencies.

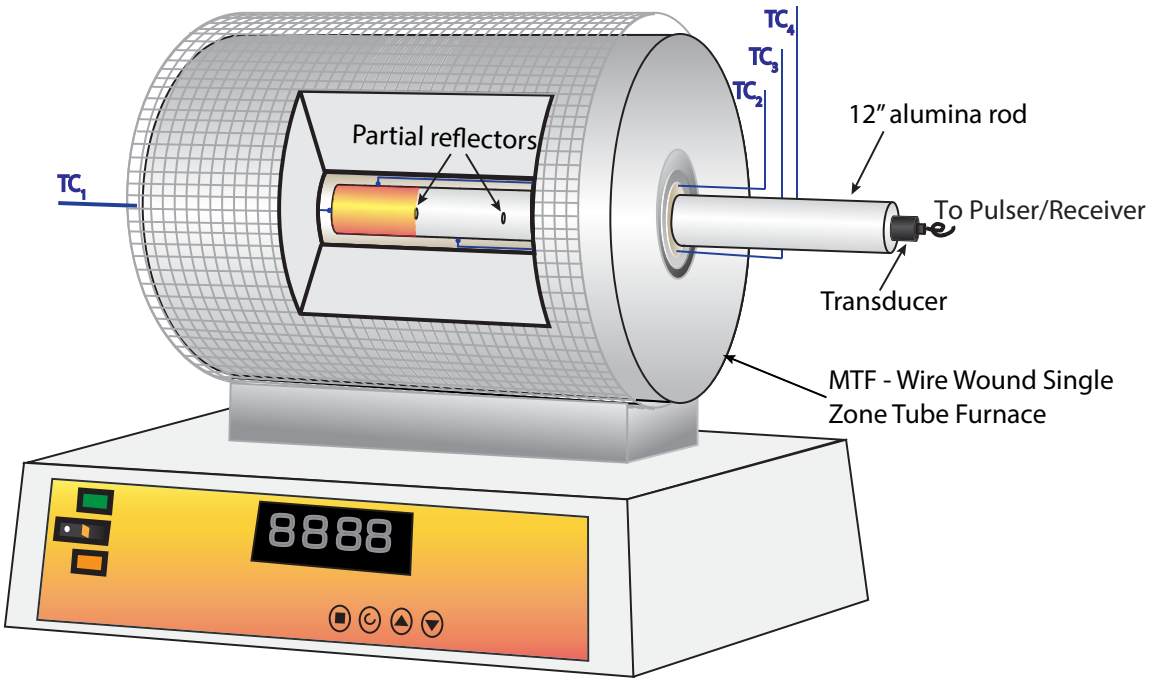

Figure 4.6: Laboratory test system in the arraignment using during the calibration experiments conducted to establish the relationship between the speed of sound and the temperature.

support base, providing convenient observation and access to all power and temperature controls. The three independently controlled heating zones of the tube furnace improve the uniformity of the maintained temperature. Despite this measure, we found that the temperature distribution inside of the heating tube is approximately parabolic, with the peak value in the center of the furnace and decreasing towards the edges. An actual setup of the lab scale ultrasound high temperature measurement system is shown in Figure 4.6. To improve temperature uniformity, the alumina ceramic waveguide was partially inserted into the furnace and held in place without surface contact with the heating tube. The segment of the refractory rod between its distal end and the hole drilled 2" away from it was placed in the center of the heating zone (colored in red in Figure 4.6).

During the experiments, the ultrasound transducer was attached to the proximal end of the alumina rod extending outside the furnace; this ensured that the transducer was operating below its Curie point. To reduce radiative heating affecting the transducer, an aluminum radiation shield was placed between the furnace and transducer. Independent temperature measurements were provided by OMEGA® Nextel ceramic insulated thermocouples attached to the hot distal end of the waveguide by gluing it to the surface with ceramic adhesive. Three additional thermocouples were attached between the drilled

holes to the side surface of the rod. The ultrasound tests were implemented using Panametrics pulser/receiver (model 5072PR) and Panametrics transducers (models V609) with a central frequency of 5 MHz. The data were acquired using Tektronix oscilloscope (model MSO 2024) interfaced to a computer. A customized Matlab code for data acquisition and data analysis was developed and used during the experiments.

For the accuracy of the calibration curve, the temperature setpoints were closely spaced in 50 °C increments from 50 °C to 1150 °C, plus room temperature at 20 °C. The sequence of temperatures for the TOF measurements and SOS calculation was randomized. The randomization included all 6 repeat experiments for each test temperature.

After each change of the setpoint temperature, sufficient time was allowed for thermal equilibration to occur before the ultrasound measurements were performed. To ensure consistency of the TOF measurements, the experiments were repeated with the transducer placed in the same location at the distal end of the sample. To reduce the effect of measurement noises, 16 consecutively acquired ultrasound waveform traces were averaged using a built-in oscilloscope averaging option. The TOF measurements were then used to calculate the SOS for all temperatures at which the experiments were carried out and the 95% confidence interval was established for each data point.

4.3 Results

4.3.1 Signal Processing

The echoes in the selected alumina ceramic waveguide produced by the introduced echogenic features are clear and strong, which allows us to obtain accurate measurements of the ultrasound TOF at high temperatures. Figure 4.7(A) gives a representative example of the echo waveforms. The insert, showing the photograph of the waveguide, is positioned to indicate the source of all echoes. The echo waveforms are also labeled as z_1, z_2, and z_3 to indicate the location of the echogenic feature producing the echo. The location of the distal end is denoted as z_{DE}. The introduced echogenic features divide the waveguide into 4 segments: L_1, L_2, L_3 and L_4. The proximal end of the sample, which is the interface between the transducer and the sample, produces the initial bang waveform seen in Figure 4.7(A) immediately following time $t = 0$. The distance between transducer and partial reflector at z_1 was treated as the delay line. Figure 4.7(B) shows the envelope of echo waveforms acquired at 4 different temperatures. The first trace, acquired at 20 °C, was used as the reference with respect to which the change in the time of flight, ΔTOF, was measured as a function of temperature by performing envelope cross-correlation analysis between the envelope of the reference waveform and the envelopes of waveforms obtained at different temperatures. Both cross-correlation and envelope cross-correlation of collected alumina waveform provide consistent TOF measurement results.

The SOS as a function of temperature calculated based on the measured TOF at a given temperature and the length of the propagation path through the fourth segment measured

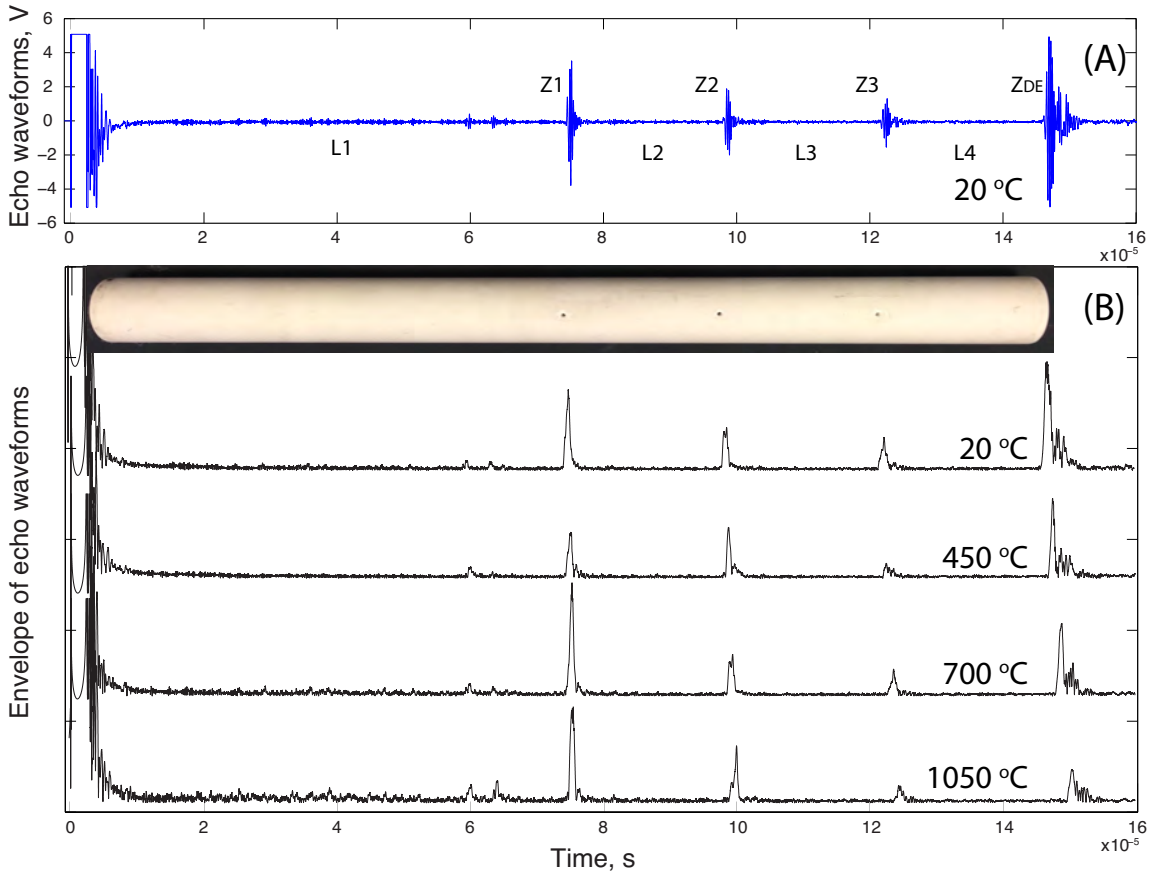

Figure 4.7: (A) Typical waveforms of ultrasound echoes created by small holes at the locations z_i, which define different segments of the alumina waveguide (insert). The last echo is created by the reflection from the distal alumina-air interface. The shown waveforms were acquired at the reference temperature equal to 20 °C. (B) Envelopes of echo waveforms acquired at different temperatures.

at room temperature:

$$c(T) = \frac{2L_4}{t_{of_4}(T)} = \frac{2(z_{DE} - z_3)}{\left(t_{of_{DE}}(T_{ref}) - t_{of_3}(T_{ref})\right) + \left(\Delta t^{z_4}_{of_{DE}}(T) - t^{z_3}_{of_3}(T)\right)} \tag{4.1}$$

where L_4 is the distance between the echogenic feature located at z_3 and the distal end of the sample z_{DE}, which was measured by a micrometer.

The temperature significantly affects the ultrasonic attenuation. The strength of echoes originating from the feature located at z_3 is reduced significantly when the temperature reaches over 800 °C. Intra-particle thermoelastic absorption is the major contributor for ultrasonic attenuation at high temperatures [91]. Portune [92] showed that thermoelastic absorption is the dominating absorptive mechanism in dense poly-crystalline ceramics which converts acoustic energy into heat.

4.3.2 SOS as a Function of Temperature

Figure 4.8(A) shows the experimentally obtained relationship between the speed of sound and the temperature changing from 20 °C to 1150 °C. It indicates a stronger dependence of the SOS on temperatures than observed with cementitious samples. Most of the experimental points from 6 randomized repeat experiments follow the same trend. A single data point from one of the repeat experiments at the highest tested temperature equal to 1150 °C appears to be an outlier. The possible cause of this variance in measurements is the reduced strength of the return echoes observed at high temperatures.

The results with and without the compensation of the measured SOS for the thermal expansion of the waveguide are shown in Figure 4.8(B). For the calibrated results, 75% of data points have uncertainties less than 1 °C. The uncertainty of the remaining measurements is between 1 and 2 °C.

The red line in Figure 4.8(B) shows the speed of sound compensated for the thermal expansion of the alumina waveguide, calculated as

$$c_{TE}(T) = \frac{L_{ref}[1 + \alpha(T - T_{ref})]}{t_{of}(T)}, \tag{4.2}$$

where α is the coefficient of the linear thermal expansion, which is $4.3 \times 10^{(-6)}$/°C ($7.74 \times 10^{(-6)}$/°F) for this alumina rod. The length of the ultrasound propagation waveguide and the SOS both change with temperature. For example, if the waveguide were heated by 1000 °C, its length increases by 0.43%. Though small, it clearly shows the SOS difference in Figure 4.8(B), which would cause temperature error for over 100 °C. However, as long as the calibration curve gives the SOS as a function of the temperature without differentiating the two phenomena, there is no practical need to distinguish the degree to which each one of the two factors (change in the SOS and the elongation of the ultrasound propagation

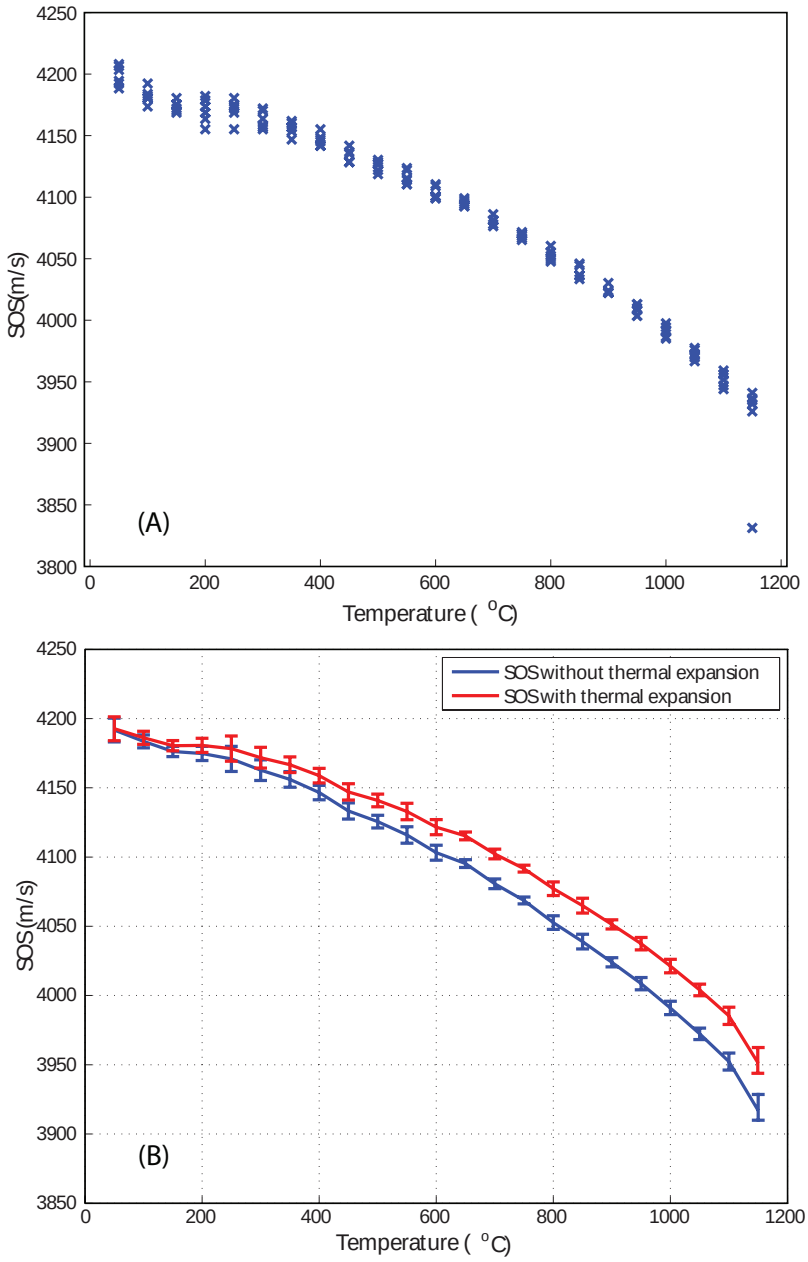

Figure 4.8: The relationship between the SOS and temperature for all six repeat experiments is shown in (A). The time of flight measurements used in the calculation of the SOS followed the envelope cross-correlation methods. The results in (B) are shown with and without corrections for the thermal expansion of alumina waveguide. The error bars in all plots indicate the 95% confidence interval for each data point.

path) contributed to the measured change in the TOF with temperature. Therefore, in the subsequent discussion we will use the SOS versus temperature data without correcting for thermal expansion.

4.3.3 Elastic Modulus

Young's modulus E and Poisson's ratio ν both change with temperature. The characterization of thermo-mechanical behavior of refractories using ultrasound [1] and, especially, the measurements of Young's modulus of refractories using the ultrasound [93] showed that Young's modulus varies nonlinearly with temperature. This nonlinear behavior is different when heating or cooling occurs [94].

Single grains of alumina exhibit some degree of elastic anisotropy; the ultrasound wave interacts with many differently oriented single grains. But overall, isotropic conditions can be applied and Poisson's ratio can be used. As mentioned before, in long bar mode, the velocity of propagation of the ultrasonic wave through the material is related to E by Equation 2.8, which has been used here to estimate the elastic property of the alumina waveguide. Though the alumina waveguide does not fit the description to apply this equation, in which the waveguide diameter is shorter than a propagation wavelength, the approximation of Young's modulus for our waveguide shows the feasibility of using the ultrasound method for elastic property measurements.

A rough estimation of E as a function of temperature can be estimated using a long rod model (2.8) which gives

$$E(T) = c(T)^2 \cdot \rho(T) = c(T) \cdot \rho_0(1 + \alpha(T))^3, \tag{4.3}$$

where ρ_0 is the density at the reference temperature, α is the coefficient of the thermal expansion, and c as a function of T is given by Equation (4.10). The result of such an estimate is shown in Figure 4.9(A), where the constant $\alpha = 4.3 \times 10^{-6}/\,^{\circ}\mathrm{F}$ (provided by the manufacturer) and the average value of the SOS at each temperature were used to estimate Young's modulus. Other elastic properties that depend on temperature include Possion's ratio, shear and bulk modulus which may be obtained using equations (2.5) and (2.8).

The study of Gault et al. [1] on Young's modulus of three industrial alumina refractories at high temperature shows a similar range of Young's modulus value as our experimental results. The refractories examined by them include three Al_2O_3-MgO castable, Al_2O_3-SiO_2-MgO sintered, and Al_2O_3-ZiO_2-SiO_2 fused-cast refectories. The tests were performed during the specimen continuously heated starting from room temperature at the rate of 5°C/min. The results of three castable refractories are summarized and compared with our experimental results in Figure 4.9(A). It was found that Young's modulus significantly decreased with temperature, with the most pronounced reduction occurring between 200°C and 400°C.

A number of studies on Young's modulus dependence on temperature of high purity sintered alumina have been performed and summarized by de Faoite et al. [2] and

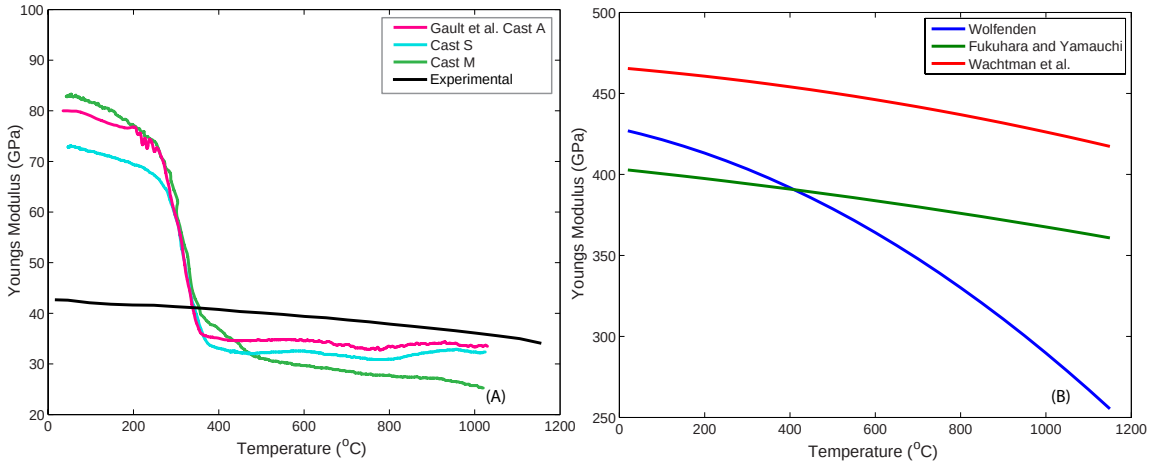

Figure 4.9: (A) Young's modulus as a function of temperature calculated based on the long rod model and its comparison with the data of Gault et al. study [1]. The results for sintered alumina [2,3] are shown in (B).

Wolfenden [3]. In their studies, Young's modulus versus temperature has been characterized as a 2^{nd} order polynomial shown in Figure 4.9(B).

All results consistently show a reduction in Young's modulus with the temperature increase. A significant difference between our results and those reported for sintered alumina by Gault et al. may be due to the difference in processing conditions, which are proprietary in many cases, including the samples used by us. It has been pointed out in literature that porosity, composition and dopants, powder size, and heat treatment method all affect Young's modulus of Al_2O_3 ceramics [2,95]. When normalized with the modulus at room temperature, E_0, our results and the results of Fukuhara and Yamauchi and Wachtman et al. are consistent, while Wolfenden's study reports a stronger dependence on temperature.

4.3.4 Calibration Curve in Normalized Form

The examination of the data summarized in Fig. **??**(A) shows an approximately equal percentage dependence. We, therefore, selected the following functional form describing the relative change in SOS with temperature:

$$\widetilde{c} = a - R^{(\widetilde{T}-b)} \tag{4.4}$$

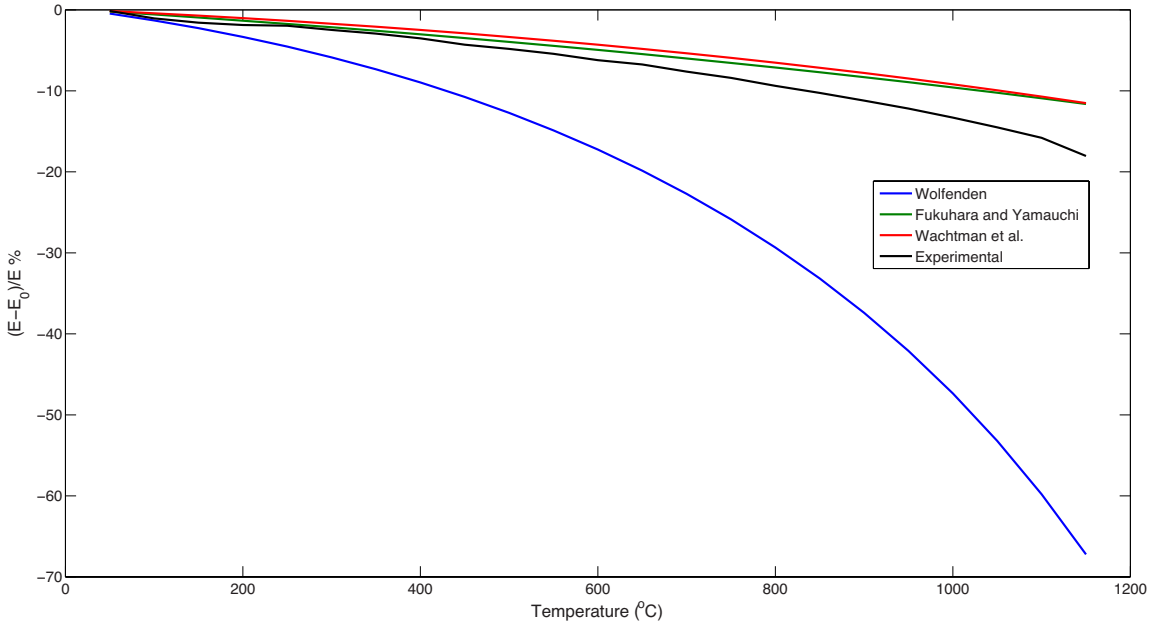

Figure 4.10: Young's modulus of elasticity normalized by its room temperature value E_0 as a function of the temperature is compared with the results reported in [2,3].

where $\widetilde{c}$ and $\widetilde{T}$ are normalized to change between 0 and 1:

$$\widetilde{c} = \frac{c(T) - c_{min}}{c_{max} - c_{min}} \tag{4.5}$$

$$\widetilde{T} = \frac{T - T_{min}}{T_{max} - T_{min}} \tag{4.6}$$

and a, b, and R are the regression coefficients. Their values that provide the best least squares fit to the experimental data were found to be

$$a = 1.172 \tag{4.7}$$

$$b = 0.943 \tag{4.8}$$

$$R = 4.907 \tag{4.9}$$

The comparison of the obtained model with the experimental results, shown in Figure 4.11, indicates an excellent agreement quantified by the coefficient of determination equal to 0.999.

After obvious manipulations, the obtained relationship can be cast in the form of equation (2.16):

$$c(T) = c_{min} + (a - R^{(\widetilde{T}-b)})(c_{max} - c_{min}) \tag{4.10}$$

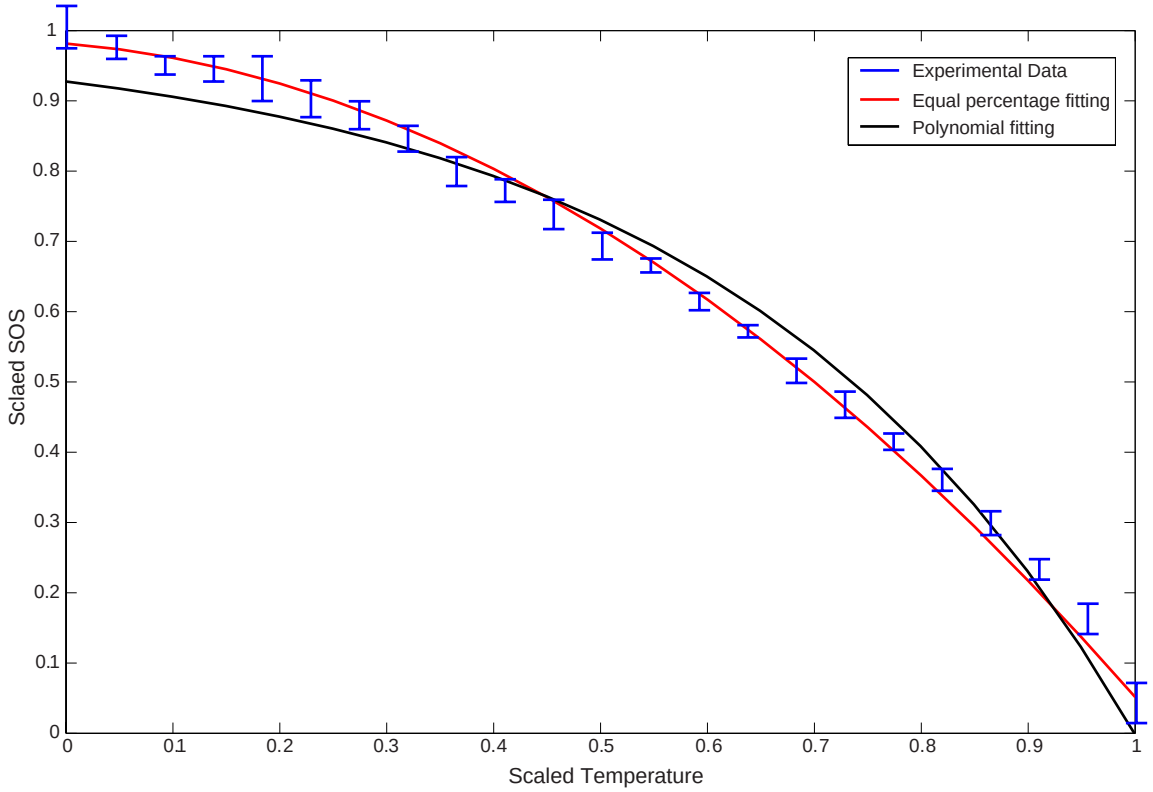

Figure 4.11: The equal percentage and polynomial fit of the SOS as a function of temperature. The coefficient of determination of the equal percentage fit is $R^2 = 0.999$. The error bars indicate 95% confidence interval.

where c_{min} and c_{max} correspond to the speed of sound at $T_{max} = 1{,}150\,^{\circ}\text{C}$ and $T_{min} = 50\,^{\circ}\text{C}$, respectively.

4.3.5 Estimation of Nonuniform Temperature Distribution

The experimental setup used during nonuniform high temperature experiments, shown in Figure 4.12, was somewhat different then the one used to obtain the SOS vs. temperature calibration curve. Only the part of the waveguide between z_3 and z_4 was placed inside of the heating zone (colored in red in Figure 4.12). The part of the ceramic rod outside of the furnace was covered with layers of fiberglass insulation to reduce heat loss. Other conditions were kept the same.

Thermocouples, used to provide independent temperature measurements, were attached to the surface of the waveguide at midpoints between echogenic features. An additional thermocouple was attached to the hot distal end of the waveguide. The data

acquisition and signal analysis were the same as during the calibration tests.

Two sets of experiments were conducted with the setpoint of the furnace maintained at either 500 or 1000 °C. Three repeat experiments were conducted for each setpoint. The sequence of experiments was randomized. All measurements were performed after the sample reached steady state temperature. Because the waveguide was only partially inserted inside the furnace, the temperature measured by the thermocouple inside the oven deviated substantially from the furnace setpoint values (~ 400 °C measured versus 500 °C setpoint and ~ 880 °C measured versus 1000 °C setpoint). To ensure consistency of the TOF measurements, the experiments were repeated with the transducer placed in the same location at the proximal end of the sample.

4.3.6 Estimation of Nonuniform Temperature Distribution

The first segment between the z_1 and the proximal end of the waveguide was used as the "delay line," and the temperature profile for this segment was not determined. By using the delay line, we avoid difficulties of extracting the reference "zero" time from the initial bang waveform seen in Figure 4.13 immediately after $t = 0$. When the temperature along the ultrasound propagation path is nonuniform, the TOF in i-th segment depends on the

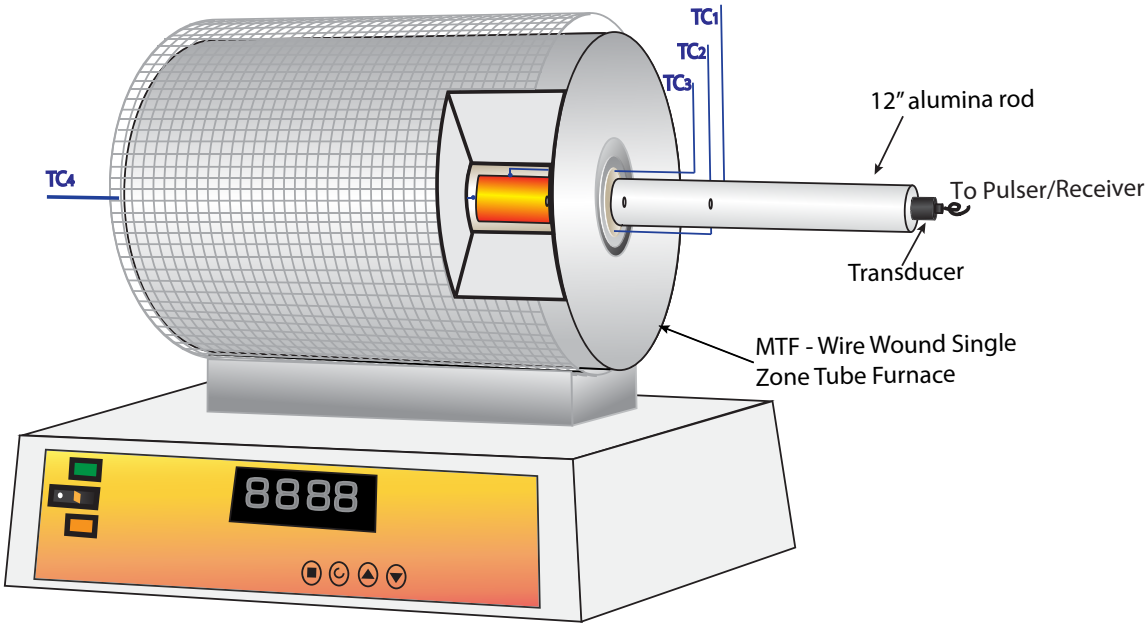

Figure 4.12: The experimental setup to establish nonuniform temperature distribution along alumina waveguide.

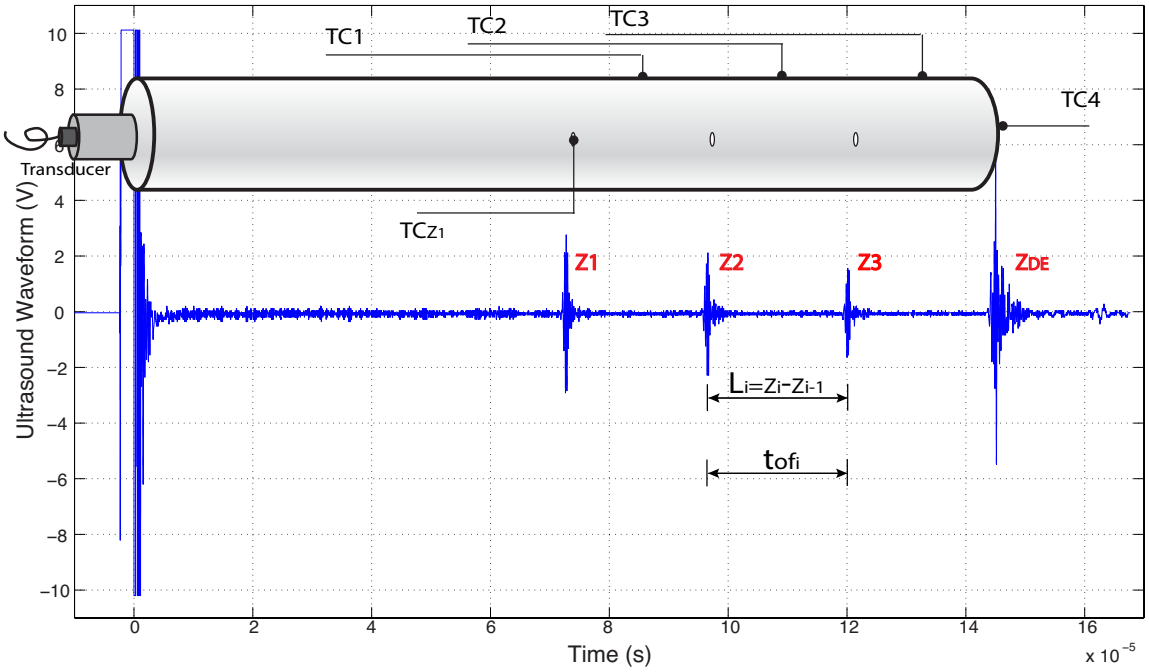

Figure 4.13: Echo waveforms used in the calculation of TOF though i-th segment used to estimate the segmental temperature distribution.

segmental temperature distribution as

$$t_{of_i} = t_{of}^{z_i} - t_{of}^{z_{i-1}} = 2\int_{z_{i-1}}^{z_i} \frac{1}{f(T(z))} dz. \tag{4.11}$$

and $T(z)$ was estimated using different parameterizations.

Piecewise Constant Temperature Distribution

The assumption of constant temperature in each segment of length L_i, coupled with the calibration Eqn. (4.10), gives the piecewise constant estimation of $T(z)$, with the temperature in the i-th segment equal to

$$T_i = (T_{max} - T_{min}) \frac{\ln\left(1 + \alpha - \frac{2L_i}{c_{min} t_{of_i}}\right) - \ln\beta}{\ln R}, \tag{4.12}$$

where

$$\alpha = \frac{a(c_{max} - c_{min})}{c_{min}}, \tag{4.13}$$

$$\beta = \frac{(c_{max} - c_{min})}{c_{min} R^{\left(\frac{T_{min}}{T_{max} - T_{min}} + b\right)}}. \tag{4.14}$$

The obtained piecewise-constant temperature distribution between z_1 and z_4 is shown in Figure 4.14. For comparison, this figure also shows independent thermocouple measurements of the surface temperature in the middle of each segment. Though the simplest possible parametrization, which predicts physically infeasible discontinuity in the estimated temperature distribution at the location of echogenic features, it nevertheless correctly captures the trend in the temperature along the length of the sample. If we approximate an axial thermal flux as $q_i \approx -k\dfrac{T_i - T_{i-1}}{z_1 - z_{i-1}}$, the obtained result is comparable to the flux estimated based on the thermocouple measurements.

Piecewise Linear Temperature Distribution

The assumption of a linearly changing temperature within each segment was used in (2.21), which leads to the following equation:

$$t_{of_i}(T) = \frac{2}{m_i} \left. \frac{(T_{min} - T_{max}) \ln\left[\left(a - R^{\left(\frac{b(T_{min} - T_{max}) - T_{min} + m_i z + n_i)}{T_{max} - T_{min}}\right)}\right)(c_{max} - c_{min}) + c_{min}\right] + m_i z \ln R}{\ln R + \ln\left[a(c_{max} - c_{min}) + c_{min}\right]} \right|_{z_{i-1}}^{z_i} \tag{4.15}$$

An additional condition needed to find unknown coefficients m_i and n_i is obtained by requiring that the temperature remains continuous at the boundary of two adjacent segments:

$$m_i z_i + n_i = m_{i-1} z_i + n_{i-1} \tag{4.16}$$

If we assume that $T(0)$ is measured independently, giving $n_1 = T(0)$, then the combination of equations (4.15) and (4.16) for all segments provides us with sufficient conditions to calculate m_i and n_i for all segments and the piecewise linear temperature distribution across the entire waveguide.

For the three segments of the waveguide for which the temperature distribution was estimated, the described procedure results in the piecewise linear temperature distribution shown in Fig. 4.14. The temperature discontinuity is eliminated, and an improved agreement with the thermocouple measurements is apparent. For segments 2 and 3 located outside the furnace, the ultrasound measurements give a higher temperature than the surface temperature measured by the thermocouples. This is a reflection of heat losses through a cylindrical surface of these segments that lower the surface temperature relative to the temperature of the waveguide's core, which we characterized with the ultrasound measurements.

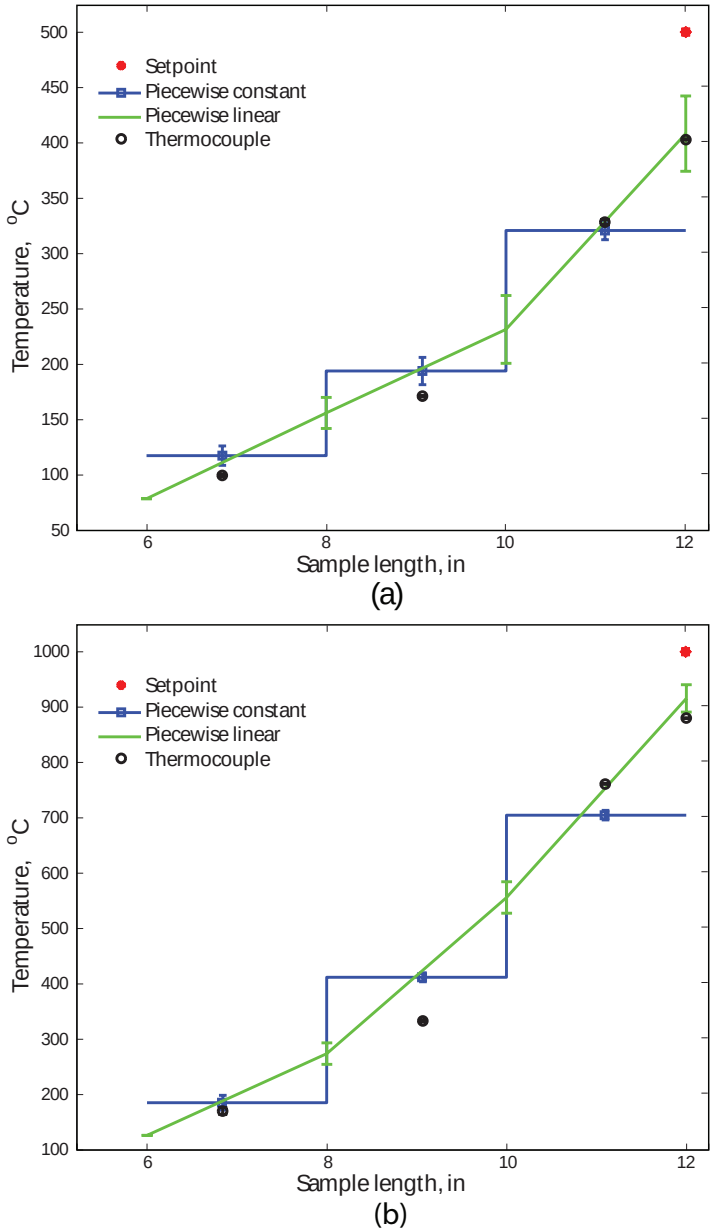

Figure 4.14: The estimated temperature distributions at steady state. Panels (a) and (b) show the results when the setpoint of the furnace (red dots) was maintained at either 500 °C or 1,000 °C, respectively. The temperature distributions in the three segments of the waveguide were obtained using piecewise-constant and piecewise-linear parameterizations. For comparison, thermocouples were used to measure the surface temperatures (black dots) in the middle of the three segments and at the distal end of the waveguide.

4.3.7 Real Time Measurements of Temporal Changes in Temperature Distribution

Preceding experiments were conducted with the furnace temperature maintained at a constant value. To validate the ability of the proposed method to measure time-dependent temperature distribution, the setpoint was changed from zero (corresponds to room temperature) to 1,200 °C, and then reduced first to 700 °C and back to room temperature, as indicated in Figure 4.15. In these experiments, the described alumina waveguide was modified by adding an additional echogenic feature by drilling the fourth 3/32" hole at $z = 11''$ (one inch away from the distal end). This divided the last (fourth) segment of the waveguide into two 1"-long segments, marked as segments 4-1 and 4-2 in Fig. 4.15 and demonstrated an improved spatial resolution of segmental temperature reconstruction. An additional thermocouple was added for the total of 5, and their placement was changed to coincide with the location of the four echogenic features, plus a thermocouple attached to the distal end of the waveguide.

We developed a Matlab code for the data collection, storage, interpretation and real time temperature display. An anisotropic diffusion filter was used with envelope cross correlation method to provide de-noised, numerically stable and accurate temperature estimation, as will be discussed in the next chapter. To ensure a high sampling rate, assumption of a piecewise constant temperature distribution was used, which simplifies real time calculations but implies a discontinuous change in the temperature at the interface between the segments.

The ultrasound measurements of the segmental time of flight were acquired continuously, while the thermocouple data were logged only after the setpoint values were reached. The obtained time-dependent estimation of the piecewise constant temperature distribution is shown in Fig. 4.15. The result is consistent with the independent thermocouple measurements of the surface temperature, and demonstrates that the developed method can be effectively used to measure temperature distribution in real time during dynamic transitions over a wide range of operating conditions.

4.4 Laboratory Tests of Refractory Degradation

We found that thermal cycling did not affect the alumina refractory sample appearance. We have not observed significant erosion of the refractory materials placed for a short time exposure in chemical baths (both base and acid treatments). Longer term refractory testing in a pilot scale combustor or gasifier would provide additional information about refractory degradation and its effect on the ultrasound propagation. Briefly, short term chemical degradation tests for refractory samples in laboratory include concentrated alkaline, concentrated acid, and diluted acid treatments. The sample testing in a concentrated solution lasted 24 hours and 60 hours in dilute solutions.

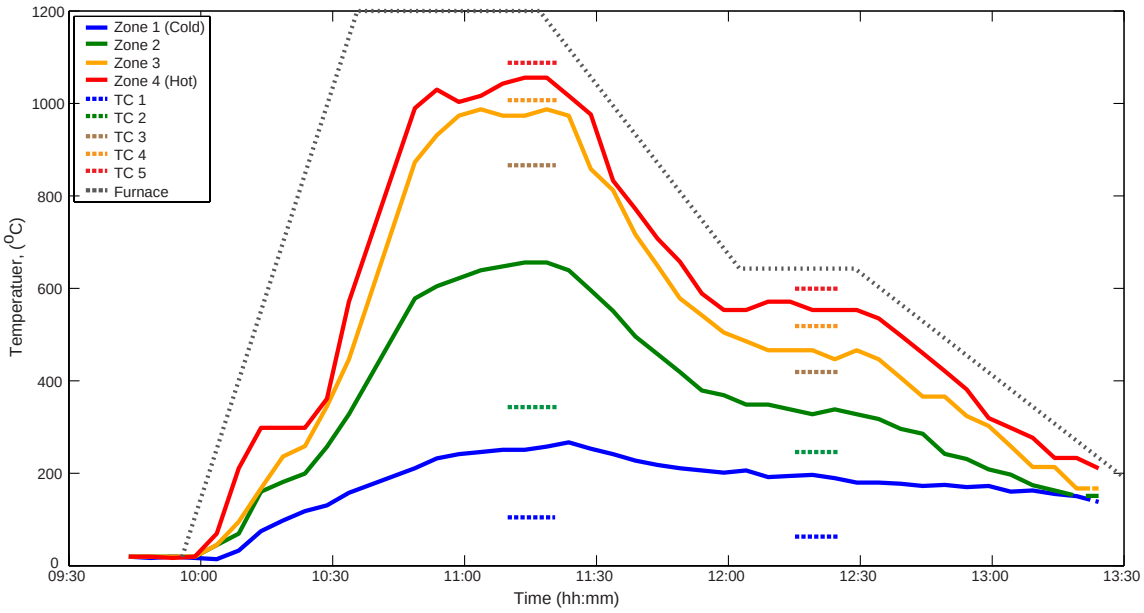

Figure 4.15: Real-time measurements of the temperature distribution in the sample during transient changes in the furnace setpoint. Thermocouple measurements were logged manually after steady state was reached after each change in the setpoint.

Both GREENCAST®-94 PLUS by APGreen and Rescor 780 by Cotronics castable samples were tested. The Contronics ceramic has a high concentration of Al_2O_3 (about 96%) while APGreen contains some fiber and a fraction of CaO, which appeared as small gravel particles in a dry sample.

Concentrated NaOH (pH 14) and NH_4OH (pH>11) were used as alkaline solutions. The tested samples remained stable after one-day soaking in these solutions, with no surface erosion or reaction observed.

The three concentrated acids used in experiments were H_2SO_4 (98% concentration), HCl (34 38%) and HNO_3 (65%). All acids had pH less than 1. Reaction on the surface of the sample and erosion were observed with samples immersed in any of three acids. The reaction with H_2SO_4 is likely

$$Al_2O_3 + 3\,H_2SO_4 \longrightarrow Al_2(SO_4)_3 + 3\,H_2O.$$

At room temperature, this reaction occurred very slowly. Rapid reaction was observed when the two samples were exposed to HCl. More than 50% of the soaked APGreen sample has reacted and dissolved within a day of exposure. The likely reason is the rapid reaction of CaO in APGreen sample with acids. The reaction between Cotronics ceramic and HCl is likely

$$Al_2O_3 + 6\,HCl \longrightarrow 2\,AlCl_3 + 3\,H_2O,$$

and was not as rapid as in the case of APGreen. Reaction between the ceramic samples and HNO_3 was not rapid initially but eventually consumed more than 30% of soaked samples after a day test. The possible reaction is

$$Al_2O_3 + 6\,HNO_3 \longrightarrow 2\,Al(NO_3)_3 + 3\,H_2O.$$

After testing in concentrated acids, the remaining part of the ceramic samples were tested in with weaker acids. Specifically, H_2SO_4, HCl and HNO_3 were diluted to a pH value of ~4, which is approximately the pH value of the gases inside gasifiers. With diluted samples at room temperature, the tested sample remained stable, with no erosion or reaction observed in laboratory experiments.

The pressure formed alumina ceramic rod is likely to be more stable than the castable tested sample tested because of its higher density and lower porosity.

Chapter 5

Anisotropic diffusion filter for robust timing of ultrasound echoes

5.1 Time of Flight Measurements

Accurate measurements of return delays and transmission times are important in many ultrasonic applications, including flaw localization [96], structure thickness and strength measurements [97], range determination [98], measurements of fluid flow rates [99], ultrasound imaging [100], and several biomedical applications [101, 102]. For example, the accuracy of ultrasonic temperature measurements depends on our ability to precisely measure the speed of sound (SOS) in materials [36,77,78], which we usually determine by measuring the time of fight (TOF).

With focus on ultrasound measurements of temperature in this dissertation, and the relationship between the time of flight and temperature, expressed as

$$T = f^{-1}(\frac{2L}{t_{of}}) \tag{5.1}$$

for solid with known ultrasound propagation distance, accurate TOF measurements are clearly essential for the accuracy of temperature measurements.

5.1.1 Cross-correlation of Waveform

It has been pointed out in previous chapters that the simplest and standard approach to the measurements of the TOF and its changes is to use temporal location of a single-point waveform feature. However, such approach is sensitive to measurement noises and small changes in experimental conditions. Our initial approach to timing of US echoes was to use threshold crossing or by matching the peak absolute values of the two round-trip echoes. When this method was used to calculate the speed of sound in the aluminum sample, we

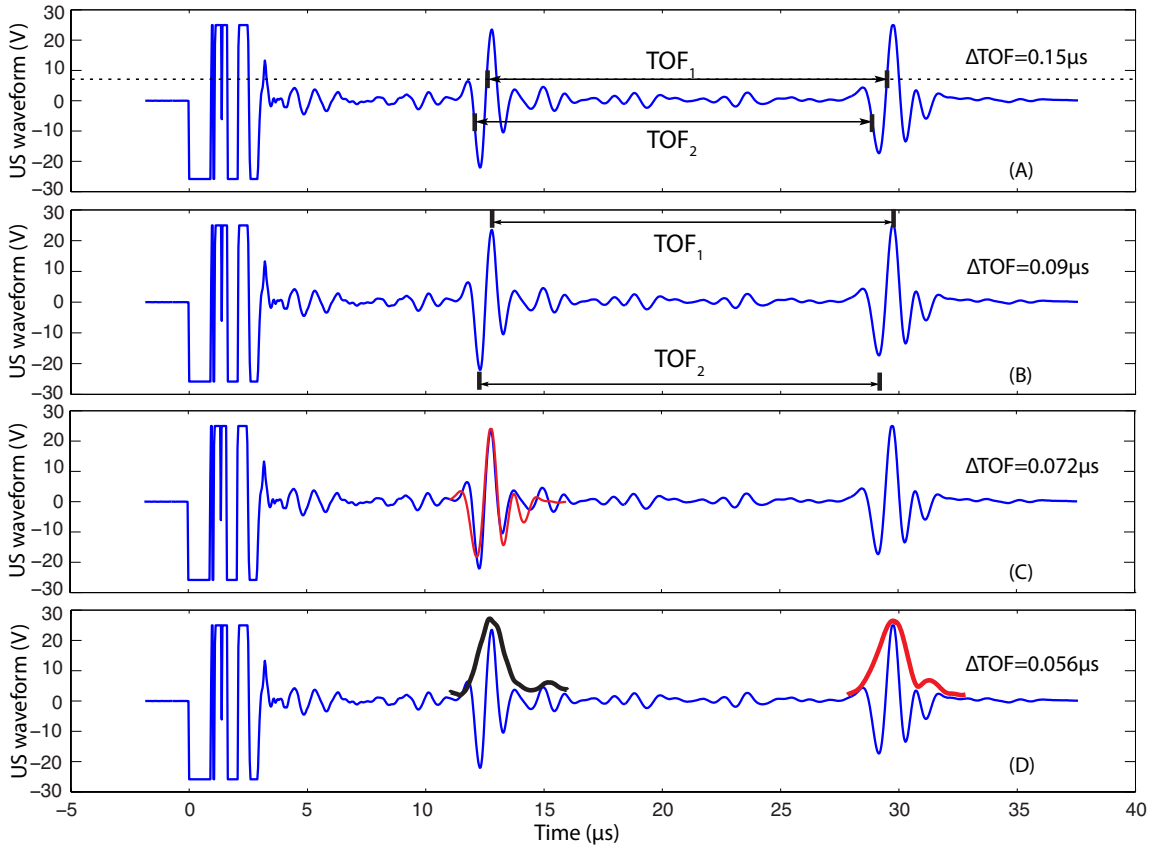

Figure 5.1: The difference in the TOF between echoes produced by an internal interface of a two-layer cementitious sample and its distal end obtained by threshold crossing (A), peak matching (B), cross-correlation (C), and envelope cross-correlation of the waveforms (D).

obtained $c_{\mathrm{Al}} = 6481$ m/s, which is very close to the handbook value. Though thresholding and peak matching approach are generally successful in low acoustic attenuation samples, they become problematic when used to time echoes propagating through dissipative samples. Figures 5.1(A) and 5.1(B) illustrate their application in timing the difference between two echoes produced by an internal interface of a cementitious waveguide and its distal end. The results obtained by the two methods are different largely due to the deterioration in timing accuracy of single-feature methods due to waveform distortions and signal broadening caused by stronger attenuation of higher frequency content of ultrasound signals.

When the entire shape of the waveform is utilized in timing by using cross-correlation and shape matching methods, a more robust and accurate measurement of t_{of} may be

achieved. In this case, both the amplitude and the phase information are taken into account [83], which makes timing results less sensitive to measurement noises. The temporal shift is obtained when the best match is found between the waveforms by maximizing their cross-correlation [84], minimizing ℓ_1 or ℓ_2 norms of their difference [85–87], or by maximum likelihood [88].

Mathematically, the cross-correlation between two signal $f(t)$ and $g(t)$ is represented as:

$$\varphi_{fg} = f \star g(\tau) = \int_{-\infty}^{+\infty} f^*(t)g(t+\tau)dt \tag{5.2}$$

where f^* is the complex conjugate of f and τ is the lag time between two signals. The shift time τ between two signals is determined by maximizing φ_{fg}.

The cross-correlation method for measuring TOF was initially tested with an aluminum standard. The experiments were performed in pulse-echo mode using an immersion transducer with 1 MHz central frequency (Panametrics model V302). Figure 5.2 shows the collected ultrasound waveform for an aluminum sample where multiple echoes represent round trips of the same excitation pulse. The difference in the time of flight of two consecutive round-trip echoes may be used to calculate the speed of sound in the sample. Figure 5.3 shows the original waveform obtained with an aluminum sample and its shift by the delay needed to maximize the cross-correlation between the first and the second echoes. The shift needed for such an alignment is precisely the value of the time of flight through the sample.

The cementitious samples and refractory materials are substantially more dissipative compared to metals. As a result, multiple round trip echoes are usually not observed. In this situation, the described method cannot be used to measure of the TOF. Our approach in this case requires that we first determine a zero time reference point, which we found to be different from the trigger time acquired from the ultrasound pulser.

5.1.2 Zero Time Reference

Our tests show that the recorded trigger time, which corresponds to the time an electrical pulse is sent to the piezoelectric transducer, is not equal to the ultrasound zero time, which is the instant when the ultrasound pulse starts its propagation through the sample. Our approach is to find the correction to the trigger time in order to obtain a reference time relative to which the TOF will then be determined.

We started by using the cross-correlation method to find the trigger time correction for materials with low ultrasound attenuation. Figure 5.4 shows the result obtained with the aluminum standard. The red dot on the blue waveform is the starting point of the first echo. By shifting time by the determined TOF value, the needed trigger correction for the particular transducer was found to be equal to 91.2 nanoseconds.

To establish if the obtained trigger correction depends on the sample, the experiments were repeated with several other materials, including bronze, stainless steel, steel and

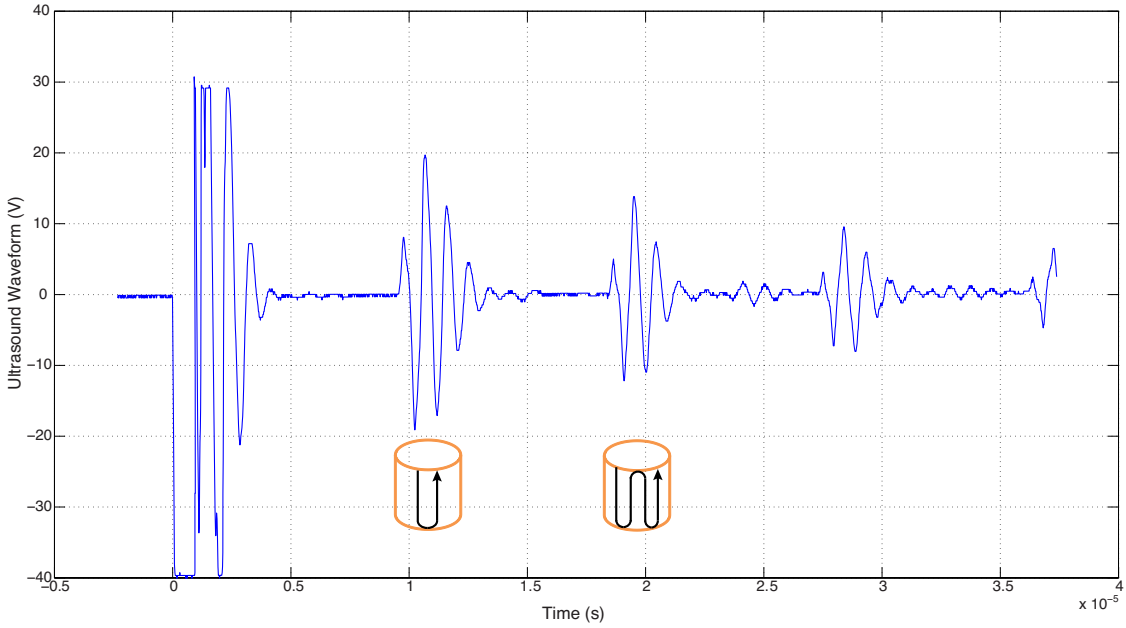

Figure 5.2: The ultrasound excitation pulse applied to aluminum samples produces multiple round-trip echoes.

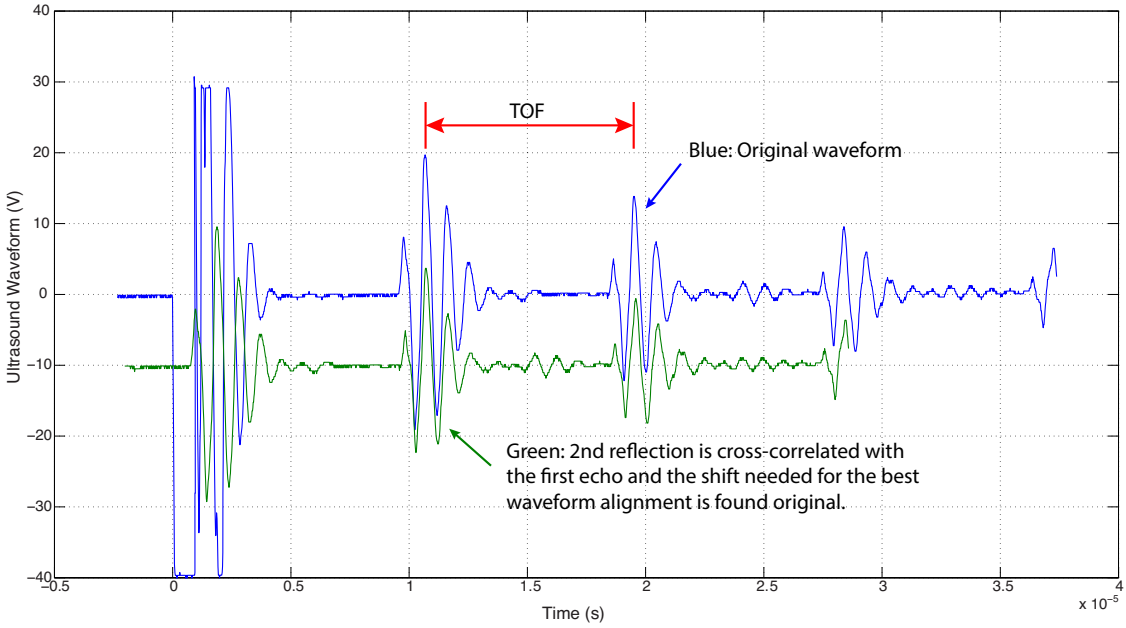

Figure 5.3: The shift needed to maximize the cross-correlation between the first and second echoes (blue trace) of the acquired response to the ultrasound excitation equal to the ultrasound time of flight through the aluminum sample. Green line shows the original waveform shifted by the calculated TOF.

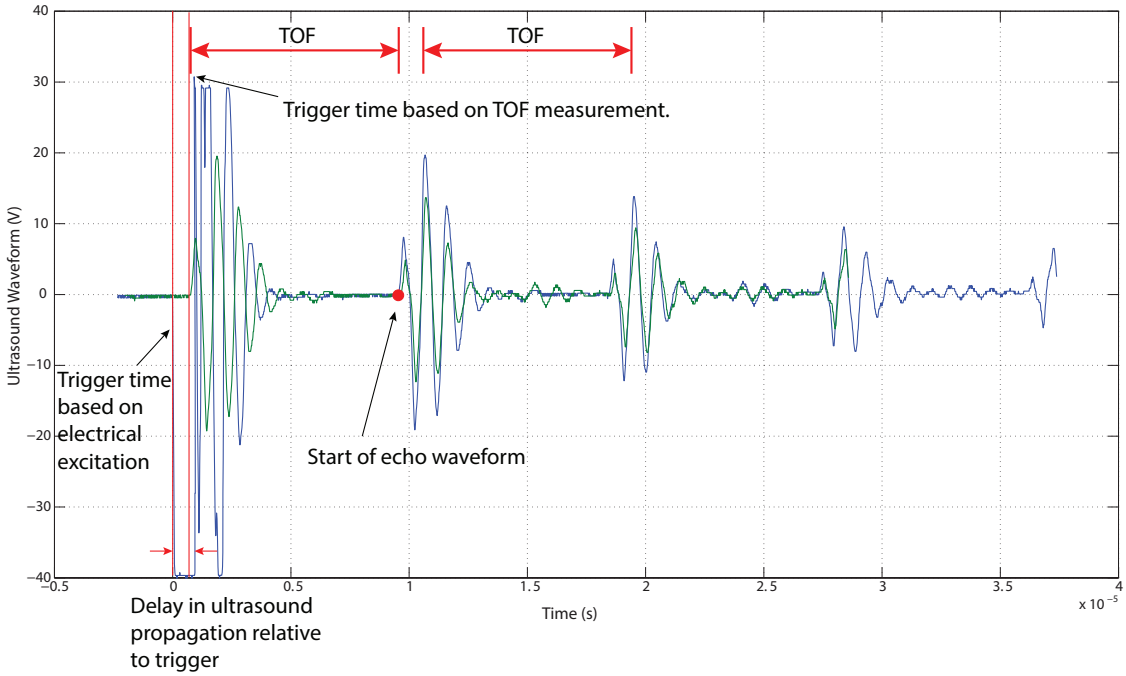

Figure 5.4: The time of the electrical trigger must be corrected to find the time when the ultrasound waveform starts its propagation through the sample.

Table 5.1: Ultrasound propagation delay relative to trigger obtained with different materials

Material	Aluminum	Bronze	Stainless steel	Steel	Plastic
Propagation delay (ns)	91.2	96	94.4	94.4	94.4

plastic. Results for all tested materials are summarized in Table 5.1 and show that the trigger correction time, equal to the delay between the electrical excitation sent to the transducer and the start of the ultrasound pulse propagation do not vary significantly with the material. This suggests that once the propagation delay is determined for a given transducer, it can be used to identify the zero reference when testing with different materials.

While we observed no to little dependence of the trigger correction on the material of the sample, it is reasonable to expect that the size and design of the transducer may have an effect on the ultrasound propagation delay which characterizes the time of transduction of an electrical pulse into the ultrasound pulse propagating through the sample. To test this hypothesis, we repeated the described experiment with a different 1 MHz transducer (Panametrics model A114s with 1 MHz central frequency). For the same aluminum sample, the signal delay observed with A114s transducer is only 25.6 nanoseconds, which is substantially shorter than the transduction delay for V302 transducer.

The possible reason for two transducers with same central frequency to have different transduction delays is the difference in their excitation bandwidth. While V302 is a vedioscan type transducer with a broadband bandwidth needed to optimize its near surface resolution, the A114S transducer is of accuscan type designed to have a relatively narrow frequency bandwidth preferable when an enhanced penetration is desired.

5.1.3 Cross-correlation of Envelopes of Ultrasound Waveforms

Though the cross-correlation method (illustrated in Figure 5.1(C)) performs better with attenuating materials than single-point timing, the results may still be unacceptable when significant distortion of ultrasound waveforms occurs, as is often the case with dissipative materials (e.g., materials with large grain sizes [103]). For waveform distorting samples, a higher precision can be achieved if the envelopes of the waveforms are used in timing [89], as illustrated in 5.1(D) for the case when the cross-correlation between waveform envelopes is used.

The analytic signal, $s_a(t)$, of a given waveform, $s(t)$, is defined as the following complex function:

$$s_a(t) = s(t) + j\hat{s}(t) \tag{5.3}$$

where $j^2 = -1$ and $\hat{s}(t) = H(s)(t)$ is the Hilbert transform of $s(t)$, which represents the

convolution of the original waveform with the function $h(t) = \frac{1}{\pi t}$. The envelope of $s(t)$ is then calculated as an instantaneous amplitude of its analytic signal:

$$A(t) = |s_a(t)| = \sqrt{s_a(t)s_a^*(t)} = \sqrt{s^2(t) + \hat{s}^2(t)}, \tag{5.4}$$

where * is the complex conjugation operator.

Several methods have been proposed to time ultrasound signals (echoes and transmission times) using the waveform envelopes. In [89], the transmission time of ultrasound pulses was measured by using the peak value of the waveform envelope as a reference point. Though this is still a single-point timing method, now based on the features of $A(t)$, it improved the accuracy when compared to timing based on single features of original waveforms (e.g., the first zero-crossing by $s(t)$). The cross-correlation of the envelope of the acquired echo with the envelope of the reference waveform was used in [36]. In the case of dissipative (cementitious) samples, a noticeable improvement was observed with this approach over the results obtained with waveform cross-correlation. A simplified version of the envelope cross-correlation method for TOF determination is summarized as Algorithm 5.1.

Algorithm 5.1 Calculate $offset_t = \text{cross}(sig_1, t_1, sig_2, t_2)$

$ls_1, lt_1 \Leftarrow findintervals(sig_1, t_1)$
$ls_2, lt_2 \Leftarrow findintervals(sig_2, t_2)$
$env_1 \Leftarrow abs(hilbert(ls_1))$
$env_2 \Leftarrow abs(hilbert(ls_2))$
$CF, Lags \Leftarrow xcorr(env_1, env_2)$
$M, loc \Leftarrow max(CF)$
$offset \Leftarrow Lags(loc)$
if $offset > 0$ **then**
  $offset_t \Leftarrow lt_2(1 + offset) - lt_1(1)$;
else
  $offset_t \Leftarrow lt_2(1) - lt_1(1 + offset)$;
end if

However, during long-term pilot-scale tests we found that performing envelope cross-correlation of echo waveforms is not sufficiently robust for accurate timing when the signal-to-noise ratio of the acquired signals is low. This motivated the development of the following method.

5.2 Anisotropic Diffusion Filter

A new method proposed here uses the results of Perona and Malik [104]. They developed an anisotropic diffusion algorithm for image processing that smooths an image without

blurring the edges found within. To achieve this outcome, the original image is iteratively subjected to a diffusion operator with spatially dependent diffusion coefficient that becomes small on the edges. As a result, the image features away from the edges are smoothed by diffusion, while the diffusion is impeded across the edges to prevent their blurring.

The anisotropic diffusion operator used in the Perona-Malik filter has this following form:

$$\frac{\partial}{\partial \tau} u(\mathbf{r}, \tau) = \nabla \cdot [D(\mathbf{r}, \tau) \nabla u(\mathbf{r}, \tau)], \tag{5.5}$$

$$u(\mathbf{r}, 0) = I(\mathbf{r}), \tag{5.6}$$

where the initial condition, $I(\mathbf{r})$, that initializes the iterations is the original image, $\mathbf{r} = (x, y)$ defines spatial position within the image, and τ is the ordering parameter that enumerates iteration steps of the discrete implementation of Equations 5.5 and 5.6. The diffusion coefficient $D(\mathbf{r}, \tau)$ changes with position and is selected by the designer to decay at the edges. Two common choices that satisfy this requirement include [104]:

$$D_1(\mathbf{r}, \tau) = \exp\left(-\left(\frac{|\nabla I(\mathbf{r}, \tau)|}{\kappa} \right)^2 \right) \tag{5.7}$$

$$D_2(\mathbf{r}, \tau) = \frac{1}{1 + \left(\frac{|\nabla I(\mathbf{r}, \tau)|}{\kappa} \right)^{1+\alpha}}, \quad \alpha > 0 \tag{5.8}$$

where κ is a selected constant. In both cases, the diffusion is small on the edges where the gradient of the grayscale image intensity is high. A proper choice of the diffusion function preserves and even enhances edges (see, for example, [105]) while ensuring numerical stability [106]. Further discussion of the effect of different design parameters on the performance of diffusion filters is found in [107].

The described filter has been used in several ultrasound imaging applications. For example, in reference [108] the anisotropic diffusion was applied to ultrasound strain images; the application of this filter to seismic images is found in [107]. To the best of our knowledge, this approach has not been previously used in timing the arrival of ultrasound waveforms by matching single-point features or shapes of their filtered envelopes.

According to the proposed method, a 1D version of the diffusion filter from Equations 5.5 and 5.6 is iteratively applied to the envelope of the acquired ultrasound waveform:

$$\frac{\partial}{\partial \tau} u(t, \tau) = \frac{\partial}{\partial t} \left[D(t, \tau) \frac{\partial}{\partial t} u(t, \tau) \right] \tag{5.9}$$

$$u(t, 0) = A(t). \tag{5.10}$$

The filtering process is initialized with the original envelope $A(t)$, given by Equation 5.4. The discrete approximation of Equation 5.9 is applied iteratively, with each new iteration using the results of the previous step as the initial condition.

The specific approximation of Equation 5.9 used by us during the experimental testing of the method is the same as the one found in [109]:

$$\begin{aligned}\frac{\partial}{\partial\tau}u(t,\tau) \approx & \frac{\partial}{\partial t}[D(t,\tau)\frac{1}{\Delta t}(u(t+\frac{\Delta t}{2},\tau)-u(t+\frac{\Delta t}{2},\tau))] \\ \approx & \frac{1}{\Delta t^2}[D(t+\frac{\Delta t}{2},\tau)(u(t+\Delta t,\tau)-u(t,\tau)) \\ & -D(t-\frac{\Delta t}{2},\tau)(u(t,\tau)-u(t-\Delta t,\tau))]\end{aligned} \tag{5.11}$$

where $\Delta t = 1$ and $u(t-\Delta t,\tau)$, $u(t,\tau)$, and $u(t+\Delta t,\tau)$ are the temporally consecutive values of the filtered envelope obtained at the preceding iteration. We elected to use the diffusion coefficient, D, given by Equation 5.7 because it tends to better preserve high-gradient data segments of the envelopes, which are analogous to high contrast edges in images. After approximating the gradient appearing in Equation 5.7, the following values of the diffusion coefficient are used in Equation 5.11:

$$D(t+\frac{\Delta t}{2},\tau) = \exp\left(-\frac{(u(t+\Delta t,\tau)-u(t,\tau))^2}{(\kappa\Delta t)^2}\right), \tag{5.12}$$

$$D(t-\frac{\Delta t}{2},\tau) = \exp\left(-\frac{(u(t,\tau)-u(t-\Delta t,\tau))^2}{(\kappa\Delta t)^2}\right), \tag{5.13}$$

where the parameter κ was set to 20. The updated value of the filtered envelope after each iteration is obtained by approximating the derivative on the left-hand side of Equation 5.11. For example, by using a simple forward difference approximation, the following update equation is obtained:

$$u(t,\tau+\Delta\tau) = u(t,\tau) + \Delta\tau \cdot rhs, \tag{5.14}$$

where *rhs* is the right hand side of Equation 5.11 and $\Delta\tau$ is the "discretization" step selected to provide the desired rate of convergence. Algorithm 5.2 summarizes the process of applying the anisotropic diffusion to envelope of ultrasound waveform.

The described filtering process uses a diffusion coefficient that takes small values when the temporal changes in the envelope are rapid. It acts to sharpen the envelope peaks while maintaining their temporal position over many iterations. The filter blurs small and slow variations that contribute to inconsistency of timing results commonly occurring when dissipative materials are tested. As a result, the timing of ultrasound signals based on the filtered envelopes is expected to be more robust to the presence of measurement noises and distortions. In the following, we put this expectation to the experimental test.

Algorithm 5.2 Calculate sig_{diff} = anisodiff($sig, iter, \delta t, \kappa$)

$sig_{diff} \Leftarrow sig$
$dx \Leftarrow 1$
$hW \Leftarrow [1 - 10]'$
$hE \Leftarrow [0 - 11]'$
for $t = 1$ **to** $iter$ **do**
  $\nabla W \Leftarrow conv(sig_{diff}, hW)$
  $\nabla E \Leftarrow conv(sig_{diff}, hE)$
  $cW \Leftarrow exp(-(\nabla W/\kappa)^2)$
  $cE \Leftarrow exp(-(\nabla E/\kappa)^2)$
  $sig_{diff} \Leftarrow sig_{diff} + \delta t * ((1/dx^2) * cW * \nabla W + (1/dx^2) * cE * \nabla E)$
end for

5.3 Experiments and Results

Two different dissipative ultrasound waveguides were used in experiments. The first sample was obtained by hot pressing high-purity alumina into 12"-long rod with 1" diameter (ceramic sample). Four 3/32" diameter holes were drilled radially along its length at 1″, 2″, 4″, and 6" from the distal end (see insert A in Fig. 1). The second sample was obtained by form casting Portland Type I/II cement-water mixture into a mold (2 in. I.D. PVC tubing). After casting a 1″-thick layer, we allowed time for partial curing to occur; this followed by casting the second 1" layer of identical composition and complete curing of this cementitious sample (shown in insert B). Partial curing introduced enough variation in material properties to create partial US reflections of the excitation pulse from the internal interface between the two layers. The ultrasound measurements were obtained using Panametrics pulser/receiver (model 5072PR) and contact transducer (model V609) which created an excitation pulse with 5MHz central frequency. The echo waveforms were acquired using Tektronix oscilloscope (model MSO 2024) interfaced to a computer. Custom Matlab code was written to control the acquisition, visualize the waveforms, and filter, analyze and interpret the data. Fig. 5.5I shows typical waveforms collected with the alumina waveguide. Partial ultrasound reflections from the drilled holes are marked as PR1, …, PR4 echoes; the reflection from the distal end of the waveguide is labeled as DE. The envelopes of these echo waveforms are shown in Fig. 5.5II. Fig. 1III shows the echoes from the internal interface and the distal end of the cementitious sample, along with the corresponding envelopes.

The importance of accurately measured time of flight of ultrasound pulses is highlighted by the influence the timing errors have on ultrasound measurements of temperature. Experimental characterization of $c = f(T)$ for our alumina waveguide indicated that at room temperature of 20°C, a TOF measurement error that overestimates the actual values by 0.1% implies that the temperature of the waveguide is 61°C – a temperature mea-

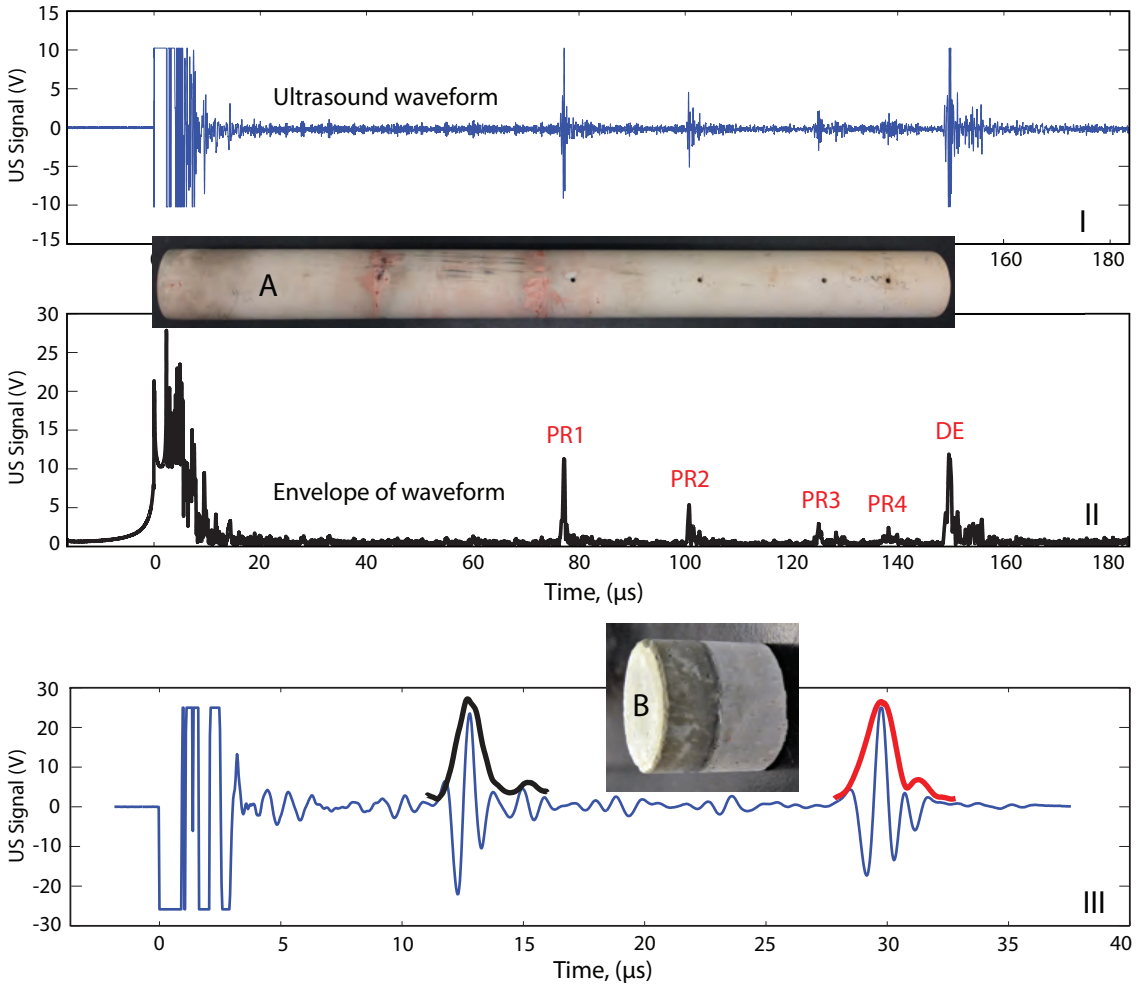

Figure 5.5: (I) Echo waveforms produced by four small echogenic features PR1...PR4 obtained by drilling small holes along the length of the alumina waveguide and the reflection from its distal end, DE. Insert (A) shows the photograph of the waveguide; its discoloration was caused by insertion into a pilot scale oxy-fuel combustor (data not included). (II) The envelopes of waveforms in panel (I). (III) Echo waveforms in the cementitious sample were created by an internal interface between consecutively cast layers and the distal end. The envelopes of the two waveforms are shown as black and red lines.

surement error of 41°C. A measurement error corresponding to 1% overestimation in the TOF at room temperature will result in the overestimation of the waveguide temperature by over 300°C.

When the ultrasound propagates through dissipative materials, noticeable variations in the waveforms taken under apparently identical experimental conditions are often present. Fig. 5.6II illustrates the variability in the echo waveforms (blue traces) produced by an echogenic feature PR1 located in the middle of the ceramic waveguide. Both waveforms were acquired at identical experimental conditions but different times. The envelopes of the two waveform (black lines) are also affected by this variability. For instance, note the change in the position of the maximum envelope values indicated by green triangles. If the maximum values are used to time the arrival of echoes, the observed variability would result in TOF measurement errors and inconsistencies. Specifically, a shift in the maximum value between the two peaks in Fig. 5.6II introduces the variation of 0.4% in the TOF measurements, which corresponds to a very significant (on the order of 150°C) error in the estimated waveguide temperature.

Panel IA in Fig. 5.6 shows the original echo waveform produced by the third echogenic feature of the ceramic waveguide (PR3) and its envelope. As in the case of echoes produced by PR1, the envelope of the original waveform is characterized by two closely separated peaks. Experiments showed that echo waveforms produced by PR3 and acquired at different times but identical conditions can also have the maximum envelope value at either one of these peaks.

To address the observed inconsistencies and the corresponding timing errors, the proposed anisotropic filter was applied to the envelopes of the echo waveforms. The result for the ceramic waveguide is illustrated in Panels IB through IE that show the filtered PR3 envelope as the number of iterations in applying anisotropic diffusion is increased from 100 to 1500. With more iterations, small variations are blurred, the filtered envelope retains a single peak, and its position is stabilized. The position of this peak can now be used to consistently time the arrival of ultrasound echoes. Once the filtered envelope is obtained, other single-point and shape-matching timing techniques may also be used.

Panel II shows that small variations in the envelopes of PR1 echoes acquired at identical conditions are filtered out after 3000 iterations and the single peak value is stabilized at the same location within both envelopes. If the maximum value of the filtered envelope is used to time the echoes, the identical estimation of the time of flight will be produced despite the variations in the original waveforms and their unfiltered envelopes.

The influence of different timing methods on the variability of the estimated TOF was investigated next. Several timing methods were considered: (a) Timing based on the maximum of the acquired echo waveform; (b) Timing by threshold value, which we selected to be 1/3 of the maximum of the waveform value; (c) Cross-correlation between the two waveforms; (d) Cross-correlation between their envelopes; (e) Maximum value of the filtered envelope; and (f) Cross-correlation between envelopes filtered using the

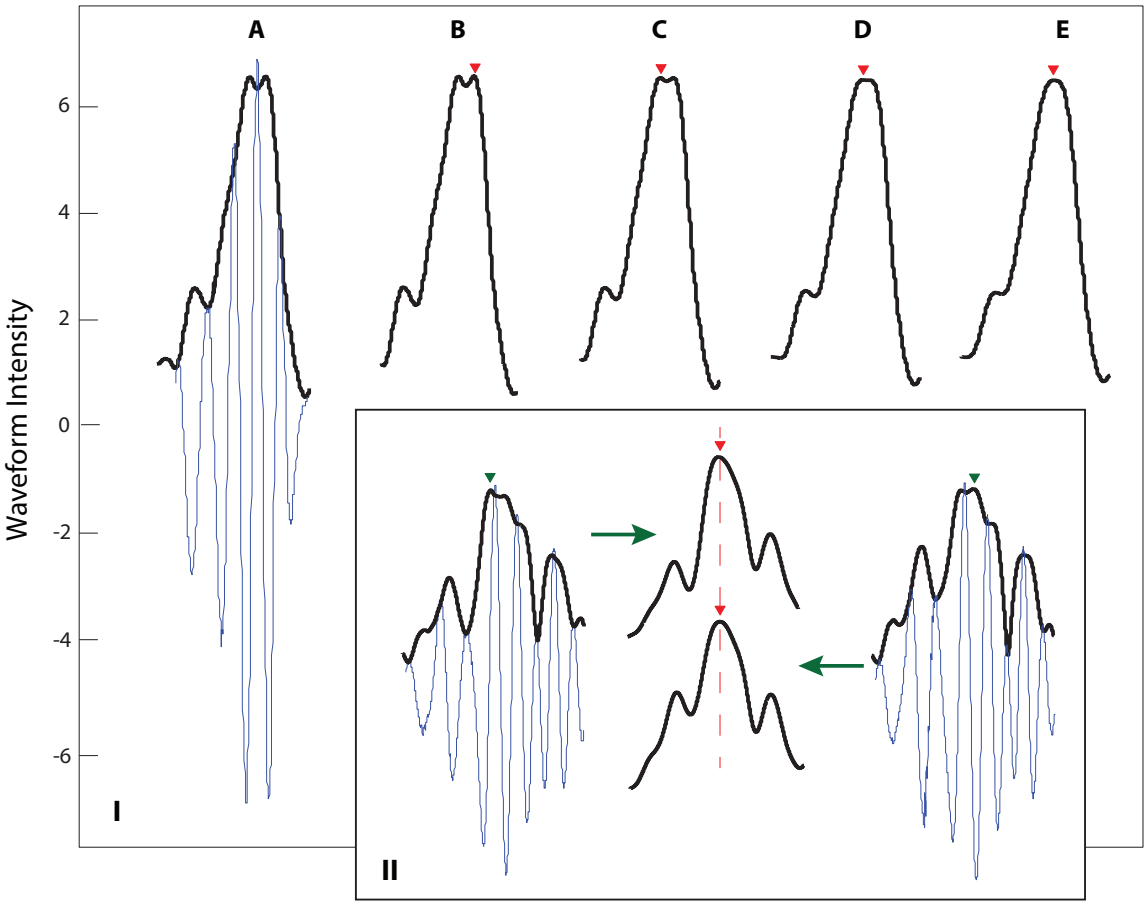

Figure 5.6: (I) The original echo waveform, shown in blue, was produced by PR3 echogenic feature of the ceramic waveguide; its envelope is shown in A. The application of the anisotropic diffusion filter for 100, 500, 1000, and 1500 iterations produced filtered envelopes respectively shown as B, C, D, and E. Maximum values of filtered envelopes are marked with red triangles. (II) Two echoes, shown as blue traces, were produced by the PR1 feature. They were acquired at the same conditions but different times. Their envelopes show variability in the position of the maximum value indicated by green triangles. After applying 3000 iterations of anisotropic diffusion algorithm, the filtered envelopes of both waveforms are shown in the middle of the panel. Red arrows show that the peak values coincide after filtering.

Table 5.2: Timing errors in ceramic waveguide

Method	**Timing difference**, s	**Difference in** T, °C
Peak of the waveform	3.0×10^{-8}	50.47
Threshold of the waveform	2.5×10^{-8}	42.30
Waveform cross-correlation	2.6×10^{-8}	43.94
Envelope cross-correlation	2.6×10^{-8}	43.94
Peak of filtered envelope	0	0
Cross-correlation of filtered envelopes	0	0

anisotropic diffusion. The comparison was first performed for ceramic waveguide based on the two PR1 echo waveforms shown in Fig. 5.6II. For each selected method, the difference in timing results when one or another waveform was used is given in Table 5.2. The same table also lists the corresponding errors in the estimates of the waveguide temperature. After applying 3000 iterations of the developed anisotropic diffusion filter, the peaks of filtered envelopes were located in identical positions for both waveforms, as illustrated in Fig. 5.6II. The cross-correlation between the two filtered envelopes shows that a zero shift is needed for the best match, indicating timing consistency when either one of the waveforms is used. For all other methods, the difference in timing based on the two waveforms was on the order of 25 nanoseconds. If we assume that this difference is an increase in the TOF over the actual value acquired when the waveguide is maintained at 20°C, the timing errors would correspond to the overestimation of the waveguide temperature by over 40°C.

Similar comparison of timing results produced by different methods was repeated for the cementitious sample. The results, summarized in Table 5.3, show a larger difference in the estimated TOF based on two different waveforms (not shown), indicating stronger dissipation and attenuation of ultrasound signals in a cementitious sample. The difference in the estimated temperature, however, is smaller because of substantially slower speed of sound in this sample. Specifically, a 1% difference in TOF at a reference temperature of 20°C produced 26°C difference in the estimated temperature of the cementitious waveguide. As before, after anisotropic diffusion filtering of the envelopes the consistent timing results were obtained based on the location of the peak values (they coincide) and the temporal shift needed to maximize the cross-correlation between the two filtered envelopes (zero shift needed).

The developed anisotropic diffusion filter was applied to the waveform data collected during transient changes in the temperature distribution of the alumina waveguide partially inserted into a high-temperature furnace (these experiments were described in the preceding Chapter). Figure 5.7 compares the results of these experiments obtained without the anisotropic filter (top graph) and and after its application to the waveform data.

Table 5.3: Timing errors in cementitious waveguide

Method	**Timing difference**, s	**Difference in** T, °C
Peak of the waveform	9.0×10^{-8}	7.4
Threshold of the waveform	10.0×10^{-8}	8.2
Waveform cross-correlation	7.2×10^{-8}	5.9
Envelope cross-correlation	5.6×10^{-8}	4.6
Peak of filtered envelope	0	0
Cross-correlation of filtered envelopes	0	0

Furnace setpoint temperature is shown as a grey dashed line in Figure 5.7. The thermocouple measurements at steady state are also included. After applying the developed filter to the waveform envelope data, the obtained ultrasound temperature measurements are consistent with the thermocouple measurements, the setpoint trajectory, and unexpected excursions in the estimated temperature distribution are eliminated.

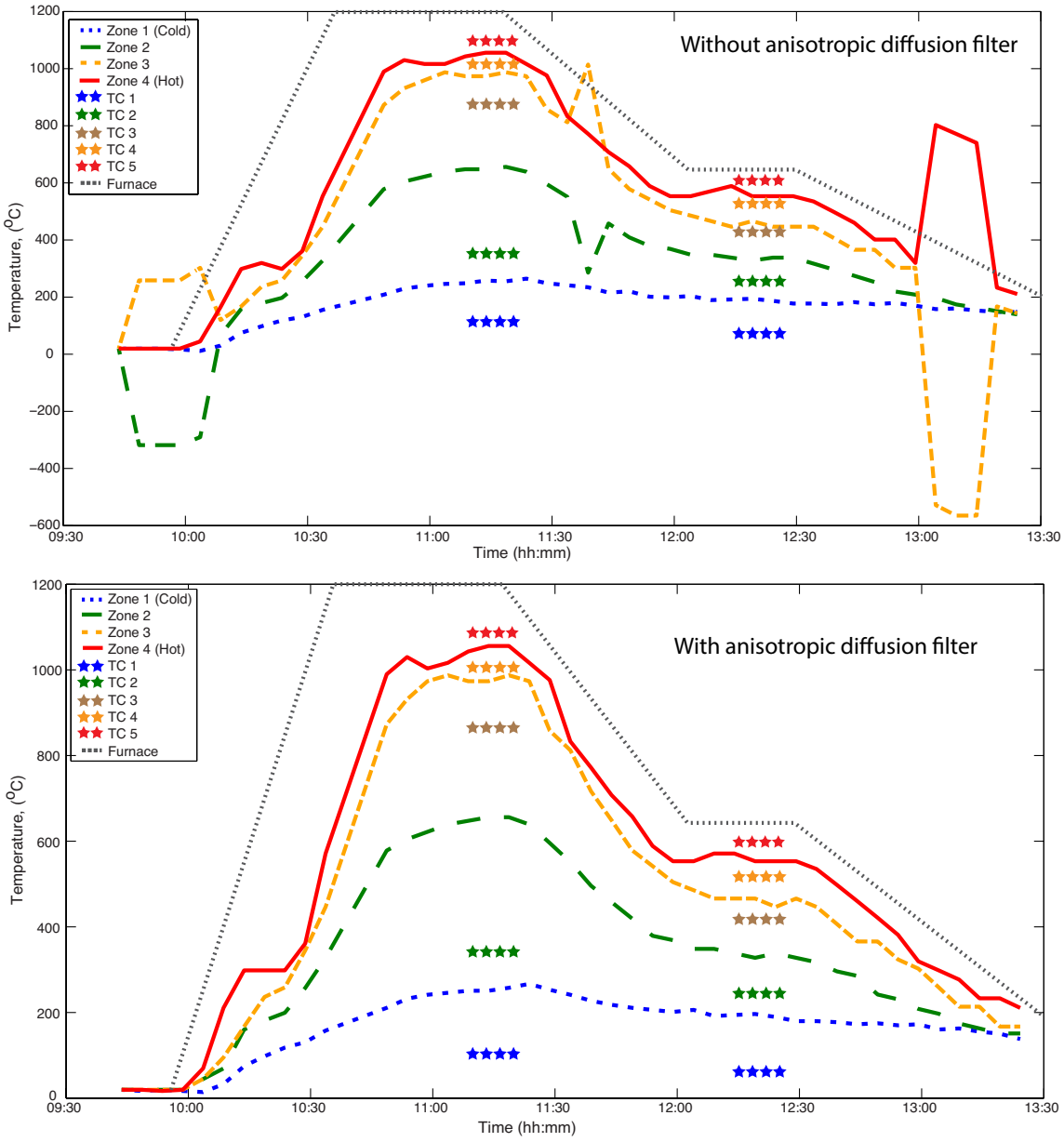

Figure 5.7: Real-time measurements of the temperature distribution in the sample during transient changes in the furnace setpoint were obtained before (top plot) and after applying the anisotropic diffusion filter. After the envelopes of the waveforms were filtered, the excursion in the estimated temperature away from the setpoint trajectory were eliminated.

Chapter 6

Pilot Scale Testing

6.1 Pilot Scale Oxy-fuel Combustor

The pilot scale experiments were carried out on a down-fired oxy-fuel combustor (OFC) schematically shown in Figure 6.1. This 100 kW pilot unit was designed to allow for a systematic control of inlet gas flow rates and to maintain refractory temperature high enough to simulate the self-sustaining combustion conditions of full-scale units in terms of the temperatures, coal particle concentrations, and mixing.

The OFC has three zones which are, from top to bottom: ignition (0.61 ID $\times$ 0.91 OD $\times$ 1.22 m height), radiation (0.27 $\times$ 0.61 $\times$ 2.60 m), and convection (0.15 $\times$ 0.15 $\times$ 3.66 m) zone. The combustion products exit the convection zone and pass through eight heat exchangers which cool the flue gas prior to discharge. The ignition zone is normally surrounded by 3 $\times$ 8 $\times$ 840 W flanged ceramic-plate electrical heaters used to control the wall temperatures of the furnace at the start-up. However, these heaters fell off from the interior surface of the refractory wall during a previous test and our experiments proceeded without using them. The burner for this unit is not equipped with an ignition nozzle. As a result, natural gas must first be used initially to heat up the furnace to a temperature high enough to ignite coal particles introduced into the ignition, at which point a self sustained combustion can be maintained. Natural gas is also used to keep furnace temperature high at night. The temperature during coal combustion is higher than achieved with natural gas, as visually apparent from Figure 6.2, which shows a quartz window into the ignition zone.

Nine pairs of ports provide access to the reaction zone inside the OFC. All ports are positioned along the vertical section of the unit and are marked as marked as P1–P9 in Figure 6.1. They can be used for sampling, instrumentation insertion, and observations. Our refractory ultrasound waveguide was mounted in the ignition zone inside port P3.

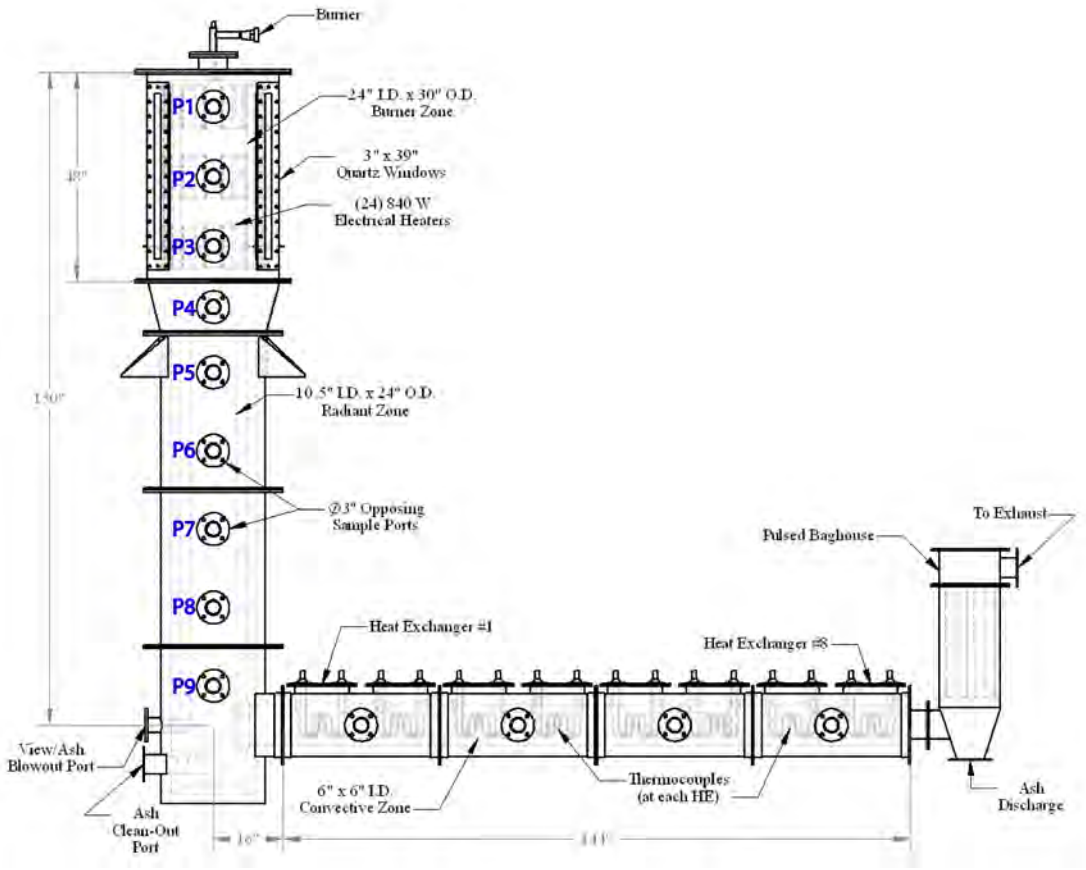

Figure 6.1: Pilot scale down-fired oxy-fuel combustor.

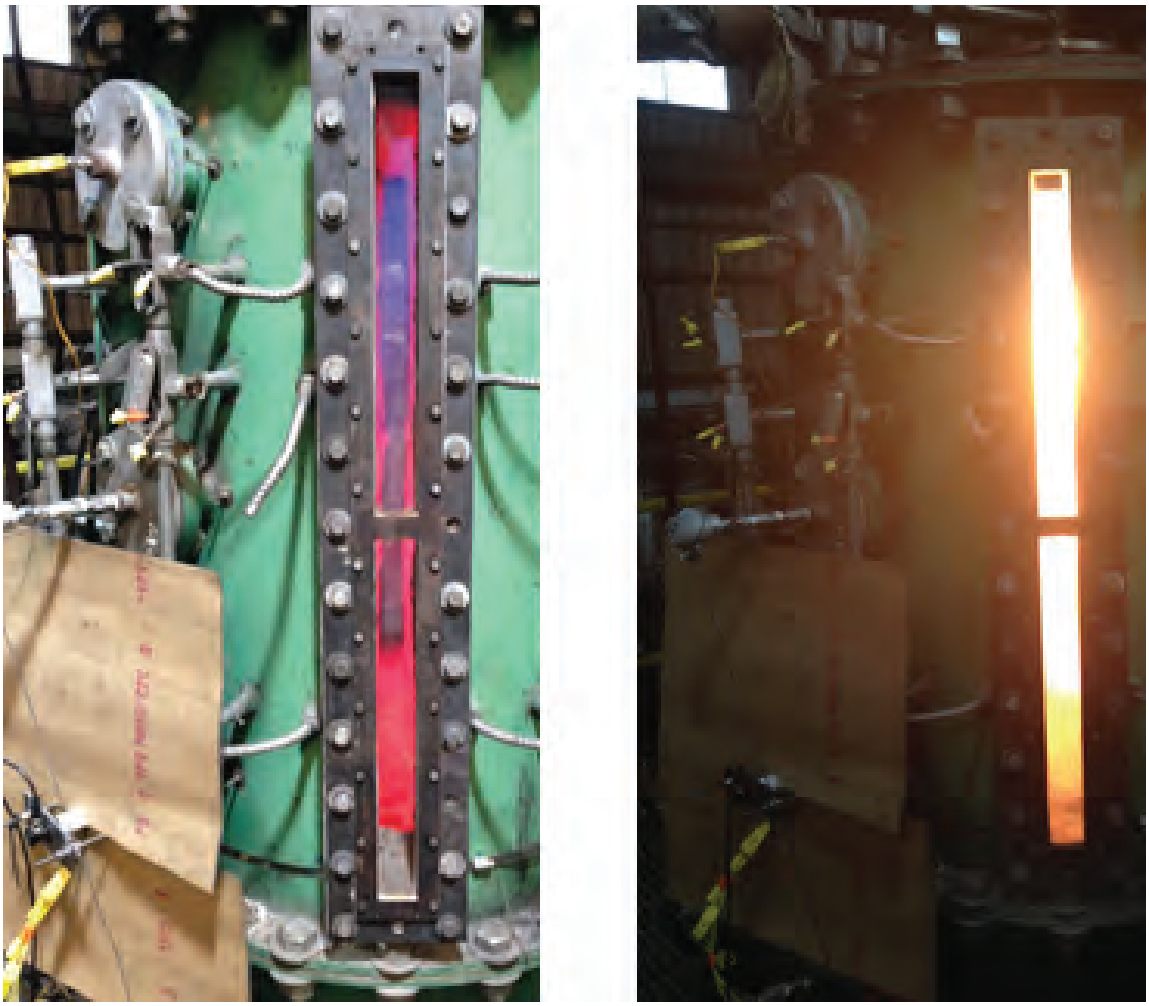

Figure 6.2: Flame imaged through a quartz window during NG (left) and coal combustion.

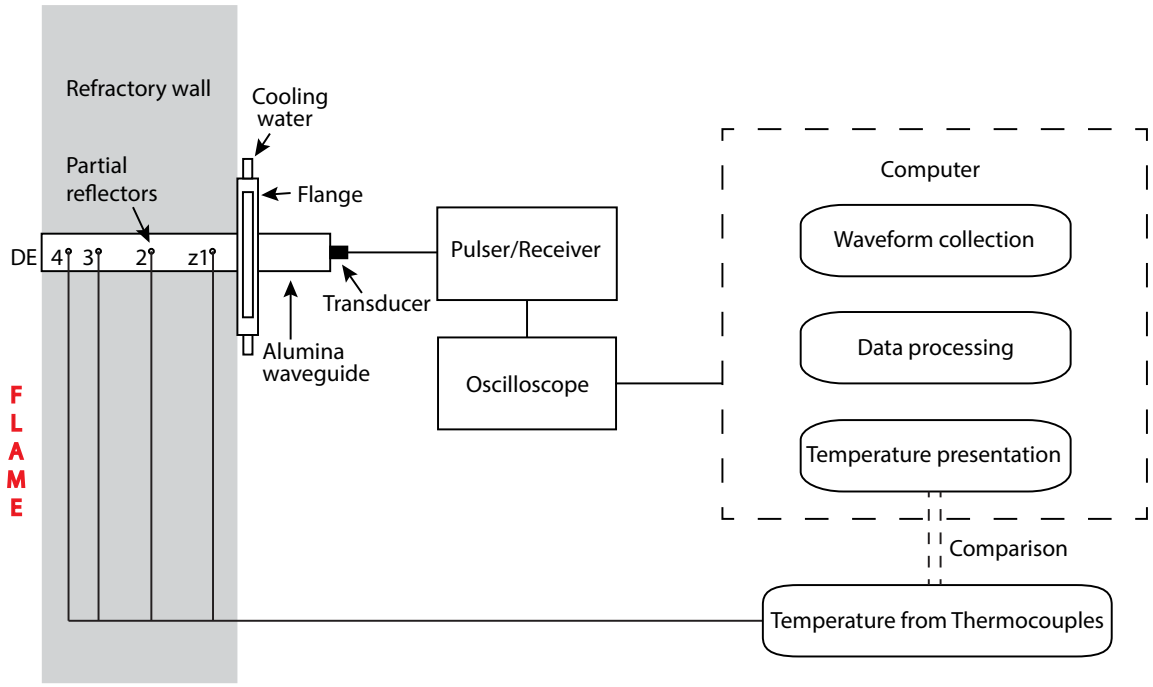

Figure 6.3: Schematic depiction of US-MSTD system designed and installed during the OFC pilot testing. Alumina waveguide was engineered with partial ultrasound reflectors located along the 1×12-inch alumina rod. Their locations, marked as z_1, z_2, z_3 and z_4, were 6, 4, 2 and 1 inches away from the hot distal end (DE) of the rod. The data acquisition and interpretation systems provided real time measurements and display of the temperature distribution across the waveguide and the comparison with the independent thermocouple measurements.

6.2 Components of the US-MSTD System: Design and Implementation

The overall US-MSTD system, that was designed to provide continuous real time temperature measurements, consists of an ultrasound waveguide engineered to provide multiple partial ultrasound reflection from known locations along its propagation length, ultrasound transducer/receiver, and the data acquisition, logging, interpretation, and the real-time display system. The schematic view of the US-MSTD system in Figure 6.3. An alumina rod was selected as the waveguide and the partial reflections were created by 4 small holes drilled along its length at 1", 2", 4" and 6" from the hot distal (relative to transducer location) end of the rod.

The overall design of the waveguide insertion system is shown in Figure 6.4. It was

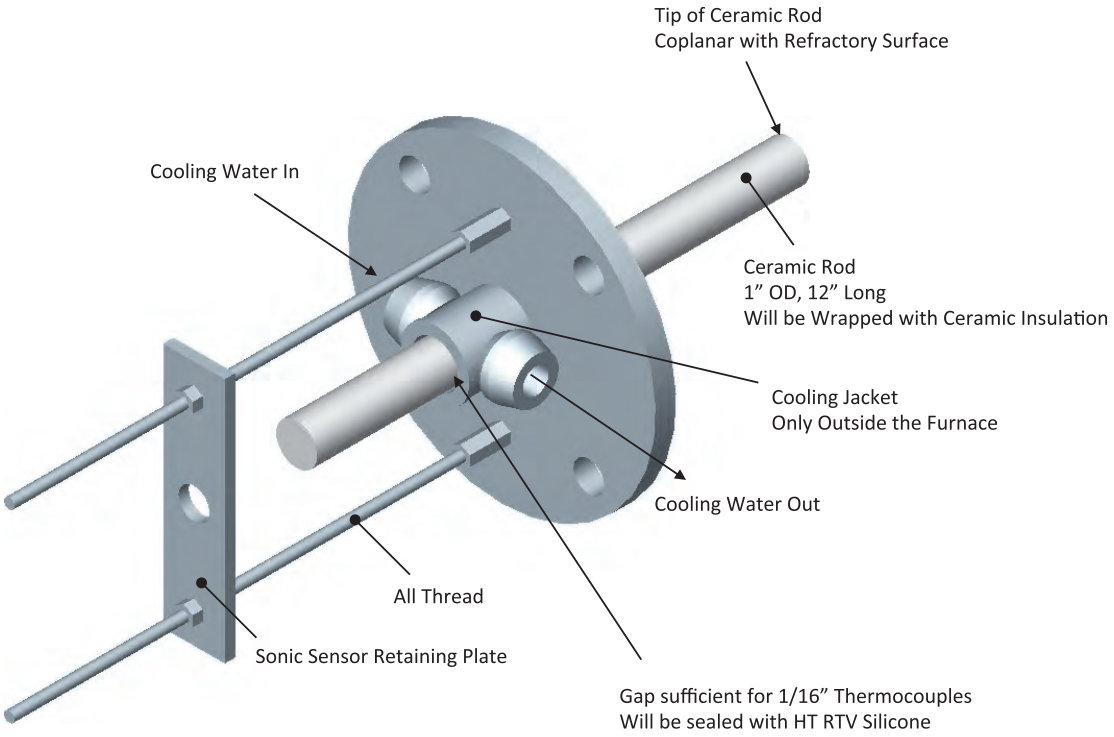

Figure 6.4: Port-mounted waveguide retention system.

designed to address several issues, including integrity of process containment, ultrasound coupling, and active cooling of the rod to insure that the temperature of its cold end is below the Curie temperature of the ultrasound (US) transducer. The photograph in Figure 6.5(B) shows the implementation of the insertion part of the system prior to its installation.

The alumina refractory rod with 5 segments was continuously used as the ultrasound waveguide during pilot scale tests. Its segment extending from transducer-waveguide interface to z_1 served as a delay line and its temperature distribution was not estimated. The combined thickness of the refractory and the steel shell of the OFC is 6-1/2 inches. The length of the inserted alumina waveguide was selected to place the distal end of the waveguide flush with the OFC refractory (Figure 6.5(G)). The diameter of Port 3 is 3 inches. The inserted waveguide was wrapped with fiber glass insulation to fill the gap between ultrasound waveguide and OFC refractory. Omega Super OMEGACLAD® type K thermocouples were bent at 90° and inserted into the holes drilled into the waveguide to provide ultrasound echoes. These thermocouples were used to acquire independent pointwise temperature measurements along the length of the waveguide. In the described arrangement, the thermocouple measurements at the location of the distal end of the

Figure 6.5: (A) Waveguide was mounted in P3 port. (B) Engineered alumina waveguide is shown mounted in the flange fixture. (C) Thermal insulation was wrapped around the waveguide. (D) The fixture is being inserted into P3 port. (E) The mounted waveguide is shown with the attached ultrasound transducer connected to the BNC cable leading to the US data acquisition system. Thermocouples are shown connected to DAQ. (F) Radiation shield is now installed. (G) Distal end of the transducer is shown to be mounted flush with the refractory surface. The picture was taken prior to the experiments with a camera inserted inside the ignition zone. (H) The system during the experiments. (I) Computer screen shows the ultrasound waveforms acquired in real time and the corresponding temperatures obtained with ultrasound measurements. (J) Components of the ultrasound data acquisition system. (K) The waveguide removed from the port at the completion of the experiments. (L) The waveguide after removing thermal insulation. Note thermocouple wires inserted into holes drilled to provide US echoes.

waveguide are not available. In order to obtain independent thermocouple measurements on the surface of the refractory, Omega Super OMEGACLAD ® type B thermocouple was inserted in Port 2 and its tip placed flush with the inside surface of the refractory. Note, however, that the temperature at the internal refractory surface at different elevations of ports P2 and P3 will generally be different.

Cooling water was run through the waveguide fixture to ensure that the temperature of the rod's cold side is within operating limits of the ultrasound transducer. Figure 6.5(E) shows the flange fixture with the attached cooling water, thermocouple leads, and the BNC connection to the ultrasound instrumentation and the data acquisition system located on the ground level within 20′ of P3 port. Figure 6.5(F) shows that we used a reflective shield to minimize the effect of radiative heat transport on the ultrasound transducer. The transducer was mounted using a retaining plate with threaded ring, which provided a secure and flexible way for its installation. The transducer was coupled to the waveguide using silicone grease. Figure 6.5(J) shows components of the ultrasound system and the data acquisition computer running custom Matlab software written to control data acquisition, and interpret and visualize ultrasound measurements, Figure 6.5(I).

In the described configuration, the sensitive electronic components are kept away from harsh gasification environments and it is only required that the US transducer be acoustically coupled to the cold side of the refractory, representing minimal modifications to the combustor.

The data acquisition system was kept the same as used during high-temperature laboratory testing. A custom Matlab software was developed for on line data acquisition, storage, interpretation and temperature profiling across the refectory. The real time visualization of the temperature distribution based on the measurements of the segmental time of flight used the combination of envelope cross-correlation method and anisotropic diffusion filtering, discussed in the previous Chapter. Using the segmental time of flight measurements obtained from the analysis of the acquired ultrasound echo waveforms, the real-time temperature distribution was obtained using the speed of sound vs. temperature relationship obtained during laboratory experiments.

In order to process the ultrasound measurements at a high sampling rate (every 5 seconds), a piecewise constant parametrization of the temperatures distribution in the four segments of the waveguide was used. The procedure for online estimation of the temperature profile in the alumina waveguide is given as Algorithm 6.1. The waveforms acquired during the pilot test have been stored and later reinterpreted using piecewise linear parametrization of the temperature distribution.

6.3 Experimental Conditions

During the coal combustion, the following conditions were used. Utah coal was fed at 8.4 lb/hr; Primary O_2 was maintained the flow of at 2.3 lb/hr; Primary flow of CO_2 was 11.9

Algorithm 6.1 Acquisition of Ultrasound Waveforms and estimation of the Temperature distribution along the Waveguide

$sig, t \Leftarrow invoke(readwaveform, channel)$
$sig \Leftarrow abs(hilbert(sig))$
$sig \Leftarrow anisodiff(sig, 100, 1/3, 20, 1)$
for $l = 1$ **to** n **do**
  $ls, lt \Leftarrow selectinterval(sig, t)$
  $m, loc \Leftarrow findpeaks(ls, NPEAKS, 1)$
  $peaks(l) \Leftarrow lt(loc)$
  if $l > 1$ **then**
    $TOF(l-1) \Leftarrow peaks(l) - peaks(l-1)$
  end if
end for
$\Sigma \Leftarrow c_{max} - c_{min}$
$\Phi \Leftarrow T_{max} - T_{min}$
$\alpha \Leftarrow \Sigma * a / c_{min}$
$\beta \Leftarrow \Sigma * R^{-T_{min}/\Phi - b} / c_{min}$
$Temp \Leftarrow log((1 + \alpha - 2 * L/(c_{min} * TOF))/\beta)\Phi / log(R)$

lb/hr; Secondary O_2 was fed at 16.5 lb/hr. The internal pressure was elevated by ~0.1" of water. During natural gas combustion, a flow rate between 6 and 6.5 lb/hr was maintained.

The US-MSTD system was used to monitor temperature distribution across the refectory during several distinct regimes of OFC operation, which included:

- Steady state combustion of natural gas and coal;
- Fuel transition from natural gas to coal; and
- Coal combustion at the different fuel flow rates.

6.4 Experiments and Results

6.4.1 Natural Gas Preheating

Figure 6.6 shows the measured temperature change along the waveguide based on piecewise constant assumption during initial preheating of the OFC by natural gas. About half an hour after the heating started, there was an unaccounted temperature drop in zone 4, which is the closest to the flame. The temperature in Zone 4 eventually increased above the temperature of Zone 3 and remained at higher at higher temperature for the duration of 5-day-long test. The electrical heaters, normally used at the startup of the unit, were not available during this experimental campaign. It is possible that we are

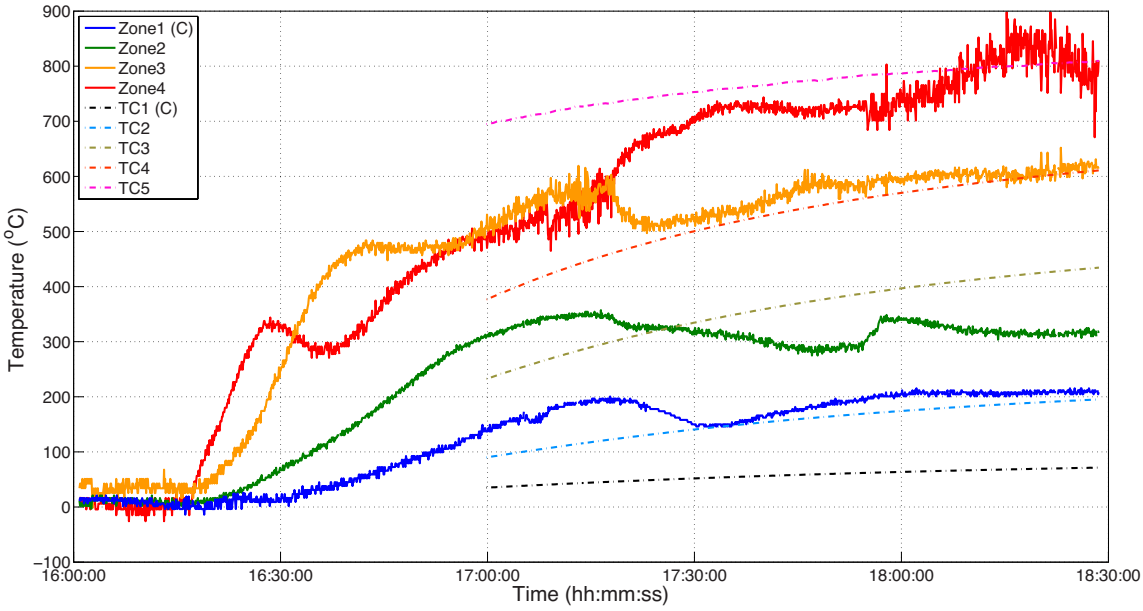

Figure 6.6: Ultrasound measurements of segmental temperature distribution across the refractory of the OFC under piecewise constant parametrization. The ultrasound results are compared with the pointwise temperature measurements provided by the thermocouples. Thermocouple measurements were not logged for the first hour of the experiment.

seeing a temperature change due to a combination of changing flow rates of natural gas and air, controlled manually and without the benefit of computer controlled refractory temperature. The acquisition of the thermocouple measurements did not start until 17:00. After 18:00, the drying of the ultrasound couplant caused the deterioration in the strength of the ultrasound echoes. The smallest SNR is for the last echo, which resulted in a higher variance in the estimated temperature of the hottest segment of the refractory, seen in Figure 6.6. The acquisition of the ultrasound signal was stopped at 18:30 and was not restarted until the next day.

6.4.2 Steady Natural Gas Combustion

Temperature measurements using piecewise constant parametrization based on the data acquired after the unit has reached steady operating conditions during natural gas combustion are shown in Figure 6.7. Figure 6.8 gives the estimation of the temperature distribution obtained using piecewise linear parametrization. The comparison of pointwise thermocouple measurements at the locations of the echogenic features z_2, z_3, z_4 with the ultrasound measurements in the corresponding spatial locations extracted from the estimated temperature distribution obtained under piecewise constant and piecewise lin-

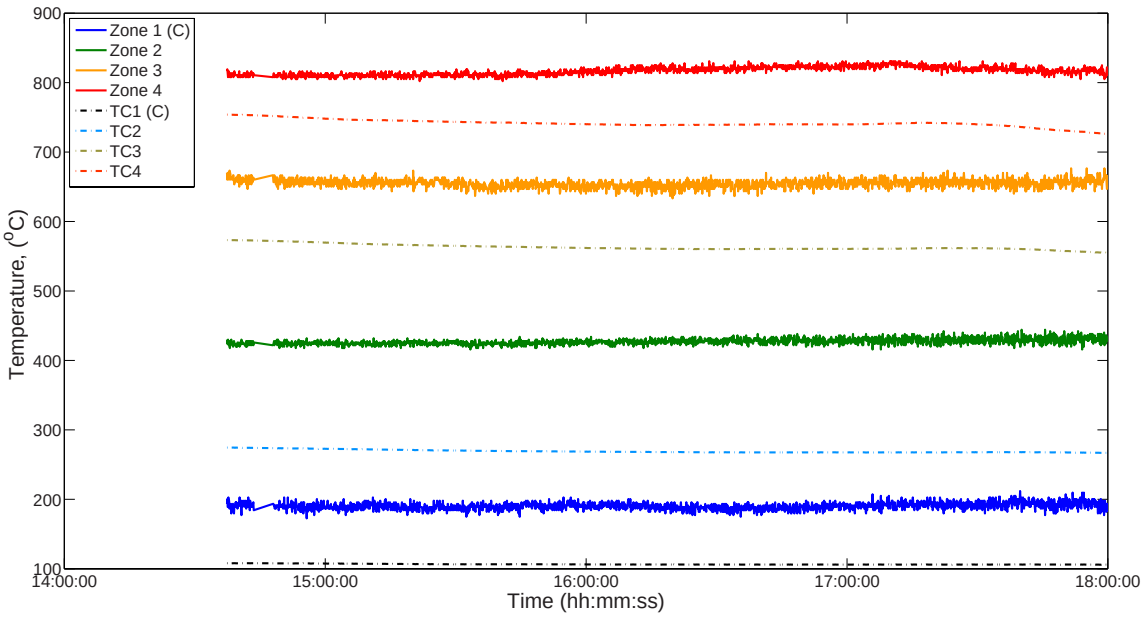

Figure 6.7: Ultrasound measurements of segmental temperature during stable natural gas combustion under piecewise constant parametrization. Thermocouple measurements are shown for comparison.

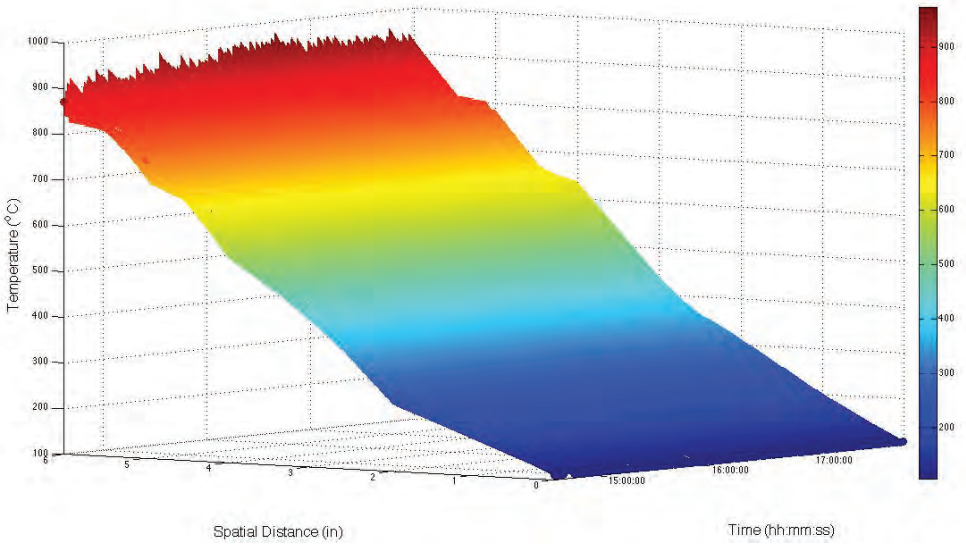

Figure 6.8: Temperature distribution across the refractory during stable natural gas combustion obtained based on piecewise linear parametrization.

ear parameterizations are shown in Figure 6.9. Because piecewise constant distribution is discontinuous at the location of the echogenic features, the result in Figure 6.9 for this parametrization is obtained by averaging temperature in the adjacent segments. For over 3 hours of continuous data, this figure shows that the ultrasound and the thermocouple measurements are consistent and for some locations (e.g., z_4) are very close to each other. Generally, the ultrasound measurements based on piecewise linear parametrization are closer to the thermocouple measurements. In general, the ultrasound measurements appear to be more sensitive to temperature changes. The variance in the ultrasound results based on piecewise linear parametrization is higher, reflecting higher sensitivity of the results to the estimated slope of the linear profile of the segmental temperature.

Several factors contribute to the difference in ultrasound and thermocouple measurements. While thermocouples provide pointwise measurements, the ultrasound measurements are sensitive to the temperature distribution, which we are estimating using different parameterizations. The second important difference is the sensitivity of the thermocouple measurements to, primarily, surface temperatures, while the US measurements depend on the temperature distribution inside the waveguide. Finally, the thermocouples were not potted inside the holes, thus creating an addition thermal resistance that contributes to the observed differences. In Figures 6.7 and 6.9, note straight line segments in the ultrasound data starting at 14:45. During this time, the ultrasound couplant was changed and no data were acquired.

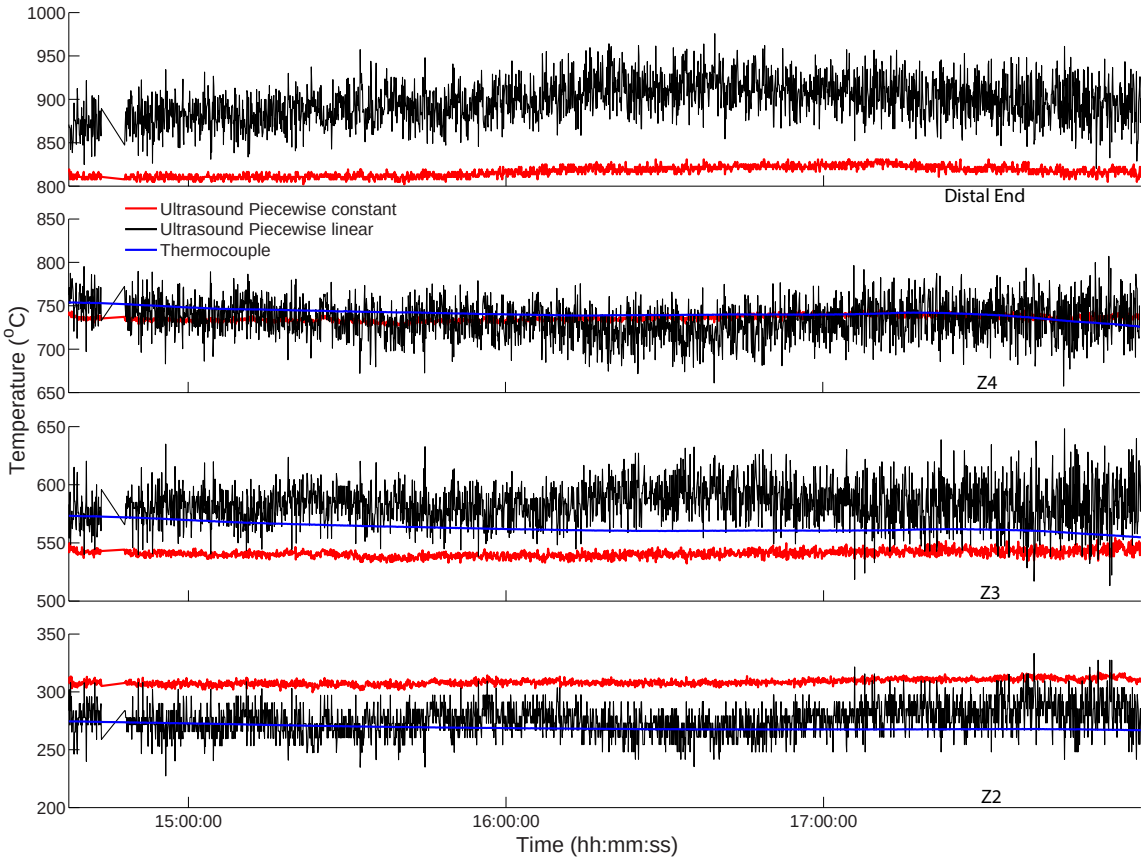

Figure 6.9: Temperature evolution at the distal end of the waveguide and feature locations z_i during stable natural gas combustion. Ultrasound results were obtained using piecewise constant and piecewise linear parametrization of the segmental temperature. The thermocouple measurements at the location of echogenic features are provided for comparison and show consistency with the ultrasound measurements.

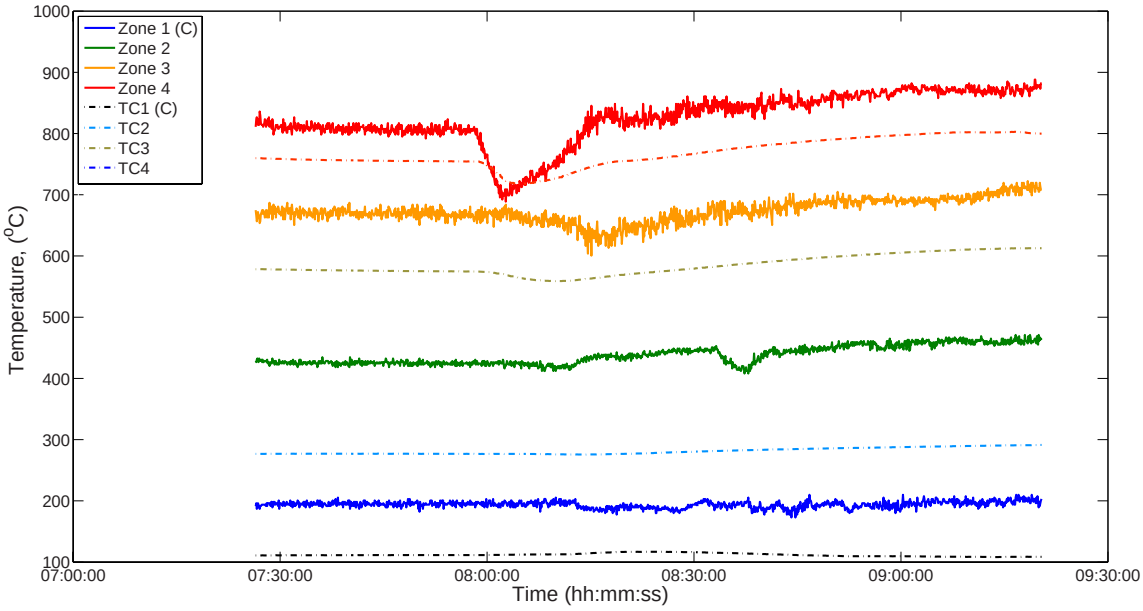

Figure 6.10: Ultrasound measurements of segmental temperature during transition from natural gas to coal combustion under piecewise constant parametrization. Thermocouple measurements are shown for comparison. Ultrasound and thermocouple measurements are in agrement, but the ultrasound response for temperature changes is faster.

6.4.3 Transition from Natural Gas to Coal

Figures 6.10 and 6.11 show the temperature change when the combustor was switched from natural gas to coal under piecewise constant and piecewise linear parameterizations, respectively. Thermocouple measurements are included for comparison. Initially, just before 8 AM the flow of natural gas was reduced, leading to the decrease in the temperature. Note that, because the ultrasound measurements are sensitive to the entire temperature distribution, they responded to this change before TC1 thermocouple did. The feeding of coal started just after 8 AM. Again, the ultrasound measurements promptly indicated that the change in fuel has occurred by showing the trend of rising temperatures before this change was registered with thermocouples.

The temperature distribution change along the waveguide indicates the heat conduction process from refractory hot face to vessel's shell. The comparisons of temperatures measured using two different parametrization in US-MSTD method and the thermocouple measurements at hot distal end of the waveguide and all echogenic features are shown in Figure 6.12. Compared to thermocouples, the US measurements give both faster and more pronounced indication that the operating conditions have changed.

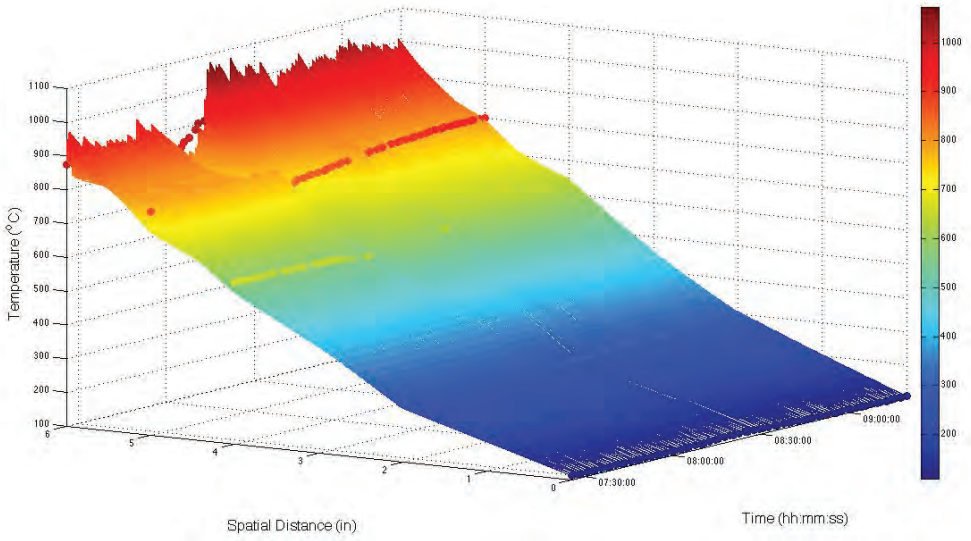

Figure 6.11: Temperature distribution across the refractory during transition from natural gas to coal combustion obtained based on piecewise linear parametrization.

6.4.4 Response to Decreased Feed Rate of Coal

Figure 6.13 shows an initial increase in temperature after switching from natural gas to coal on one of the test days. This transition occurred before 8 AM and was not captured due to miscommunication with operating personnel. After rising, the temperature stabilized, at which point, at approximately 9:20 AM, the flow rate of coal was reduced. The measured temperature decreased in response and stabilized in the lower range. The corresponding temperature distribution obtained using piecewise linear parametrization is shown in Figure 6.14. Compared to thermocouples, the US measurements give, both, faster and a more pronounced indication that the operating conditions have changed. Note that the temperature in segments 2 and 1 was only marginally affected.

The comparisons of temperatures measured using two different parametrization in US-MSTD method and the thermocouple measurements at hot distal end of the waveguide and all echogenic features are shown in Figure 6.15, and indicate an excellent agreement.

6.4.5 Stable Coal Combustion

The last captured process during this pilot testing campaign was the stable coal combustion. The temperature distribution estimated using US-MSTD method is shown in Figures 6.16 and 6.17 under piecewise constant and piecewise linear parameterizations, respectively. The comparisons of temperatures of obtained using both parameterizations and

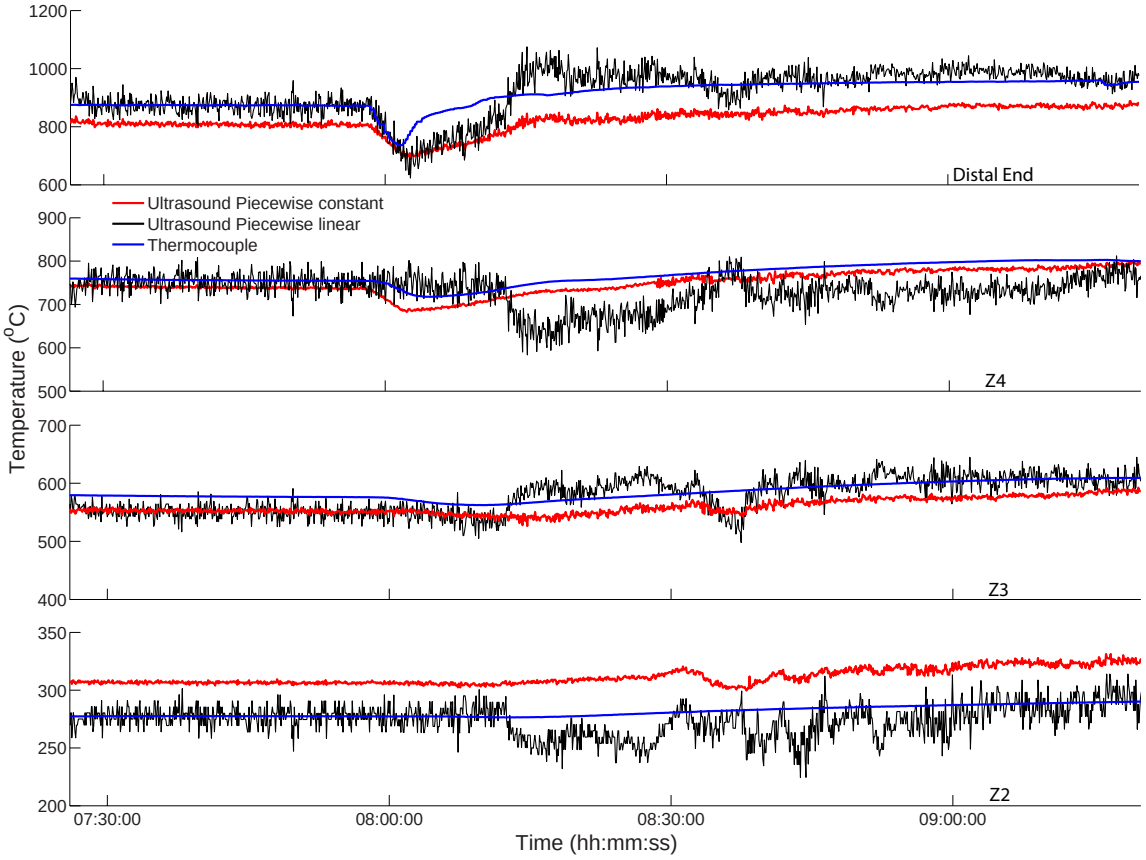

Figure 6.12: Temperature evolution at the distal end of the waveguide and feature locations z_i during transition from natural gas to coal combustion. Ultrasound results were obtained using piecewise constant and piecewise linear parametrization of the segmental temperature. The thermocouple measurements at the location of echogenic features are provided for comparison and show consistency with the ultrasound measurements.

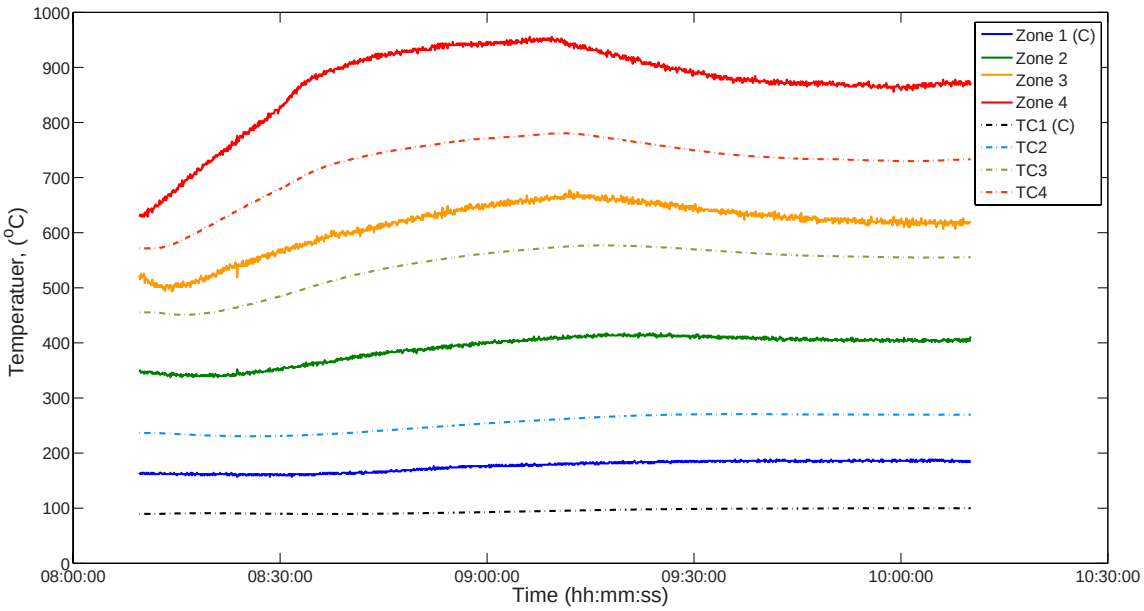

Figure 6.13: Ultrasound measurements of segmental temperature during the reduction in the feed rate of coal under piecewise constant parametrization. Thermocouple measurements are shown for comparison and indicate the same trend in temperature changes.

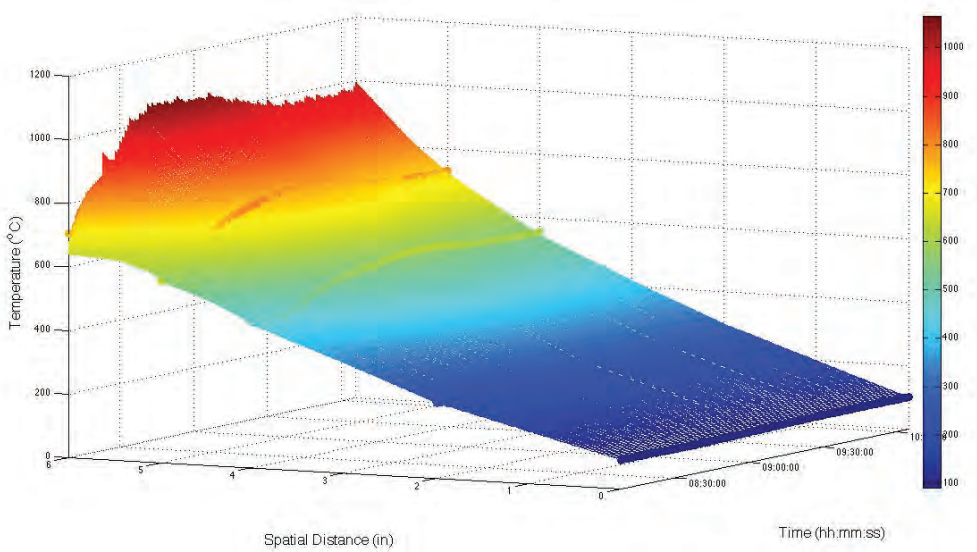

Figure 6.14: Temperature distribution across the refractory during the reduction in the feed rate of coal obtained based on piecewise linear parametrization.

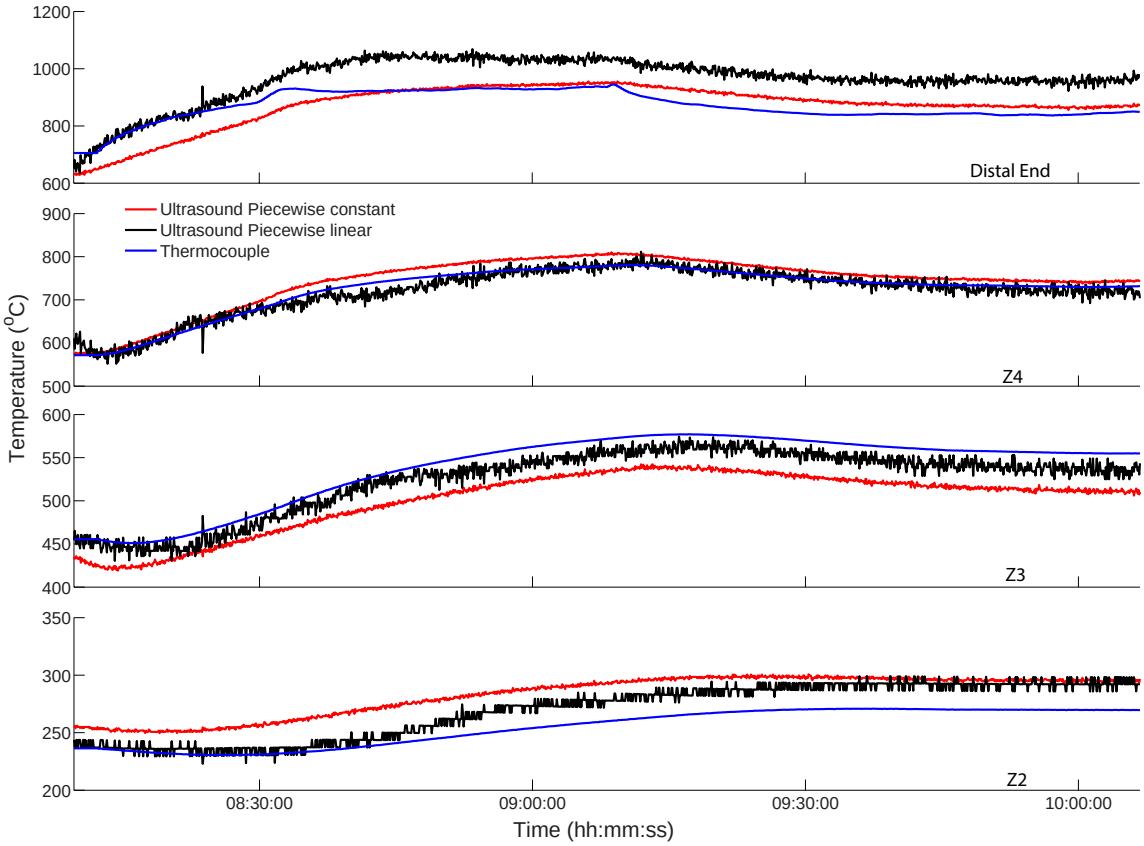

Figure 6.15: Temperature evolution at the distal end of the waveguide and feature locations z_i during the reduction in the feed rate of coal. Ultrasound results were obtained using piecewise constant and piecewise linear parametrization of the segmental temperature. The thermocouple measurements at the location of echogenic features are provided for comparison and show consistency with the ultrasound measurements.

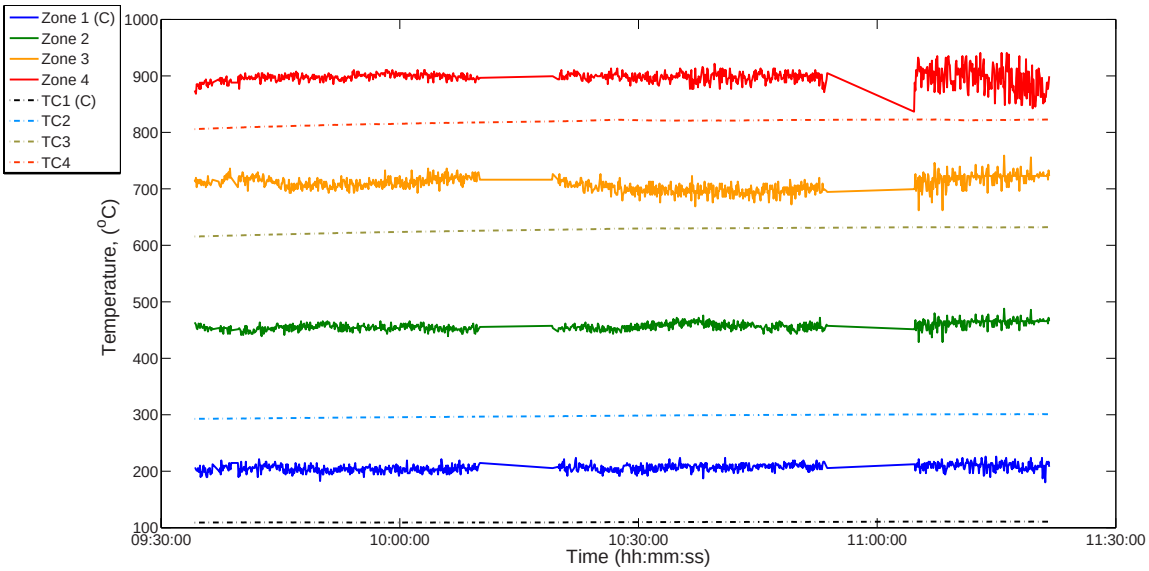

Figure 6.16: Ultrasound measurements of segmental temperature during stable coal combustion under piecewise constant parametrization. Thermocouple measurements are shown for comparison and indicate the same trend in temperature changes.

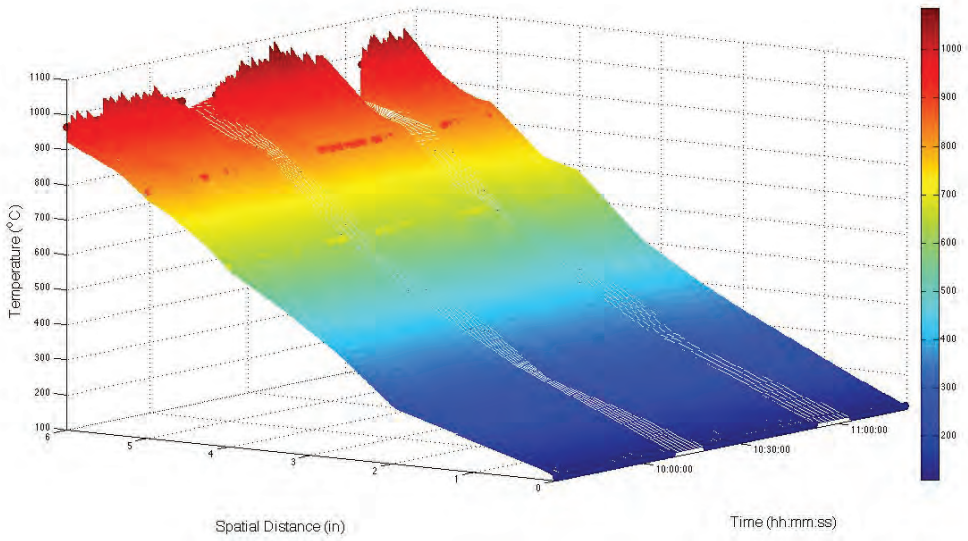

Figure 6.17: Temperature distribution across the refractory during stable coal combustion obtained based on piecewise linear parametrization.

the thermocouple measurements at hot distal end and all echogenic features are shown in Figure 6.18. The refractory temperatures during coal combustion are higher than during the natural gas combustion, especially in zone 3 and 4, closest to the flame. Significant reduction in the strength of the ultrasound echoes was observed as the pilot testing progressed, especially for the echo produced by the feature closest to the combustion zone (1 inch away from the distal end). Several intervals when ultrasound measurements flat lined correspond to times when the signal had deteriorated enough to motivate the application of fresh ultrasound couplant at the transducer-waveguide interface. Subsequent investigation of the the alumina waveguide revealed that a more likely reason for the deterioration of the ultrasound signals is the change in the material properties, mainly the growth of the grain boundaries, as discussed later in this chapter.

6.4.6 Surface Temperature of the Refractory

The distal end of the waveguide was aligned with the hot refractory surface. Therefore, the temperature of the distal end measured by US-MSTD method gives the direct characterization of the temperature on the surface of the refractory. Figure 6.19 shows the ultrasound measurements of the distal end temperature under two parametrizations of the temperature distribution obtained during the process transitions and different operating conditions described above. For comparison, this figure also shows the temperature measurements obtained with the thermocouple inserted into a different ports (port P2) and aligned with the surface of the refractory. For all operating conditions, the ultrasound measurements are consistent with the independent thermocouple measurements and capture similar temperature trends. This demonstrates on the pilot scale the capability of the developed US-MSTD method to measure surface temperature inside containments of extreme environments.

6.5 Discussion

The US-MSTD system was successfully tested on the pilot scale OFC oxy-fuel combustor during ~120 hours of continuous optation. Real time temperature distributions along the waveguide were captured during all relevant process changes. The comparison of temperature results based on US-MSTD method and thermocouple measurements exhibit excellent consistency. Several issues were revealed during the test.

6.5.1 Couplant

The continuous real-time temperature monitoring using US-MSTD method requires permanent coupling which is essential for providing the acoustic bond between the transducer and the waveguide. Couplants come in different forms, such as gels, oils, grease, pastes and others. After laboratory experimentations, for pilot scale studies we selected silicon

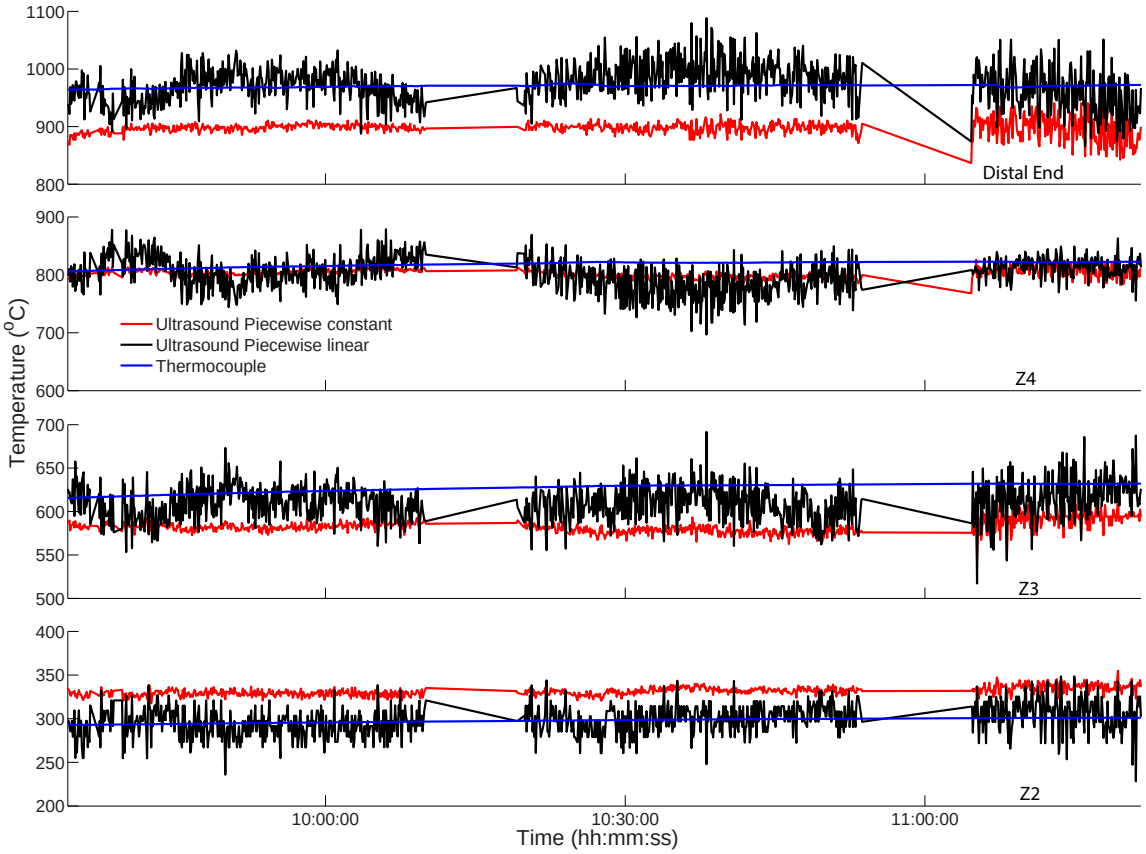

Figure 6.18: Temperature evolution at the distal end of the waveguide and feature locations z_i during stable coal combustion. Ultrasound results were obtained using piecewise constant and piecewise linear parametrization of the segmental temperature. The thermocouple measurements at the location of echogenic features are provided for comparison and show consistency with the ultrasound measurements.

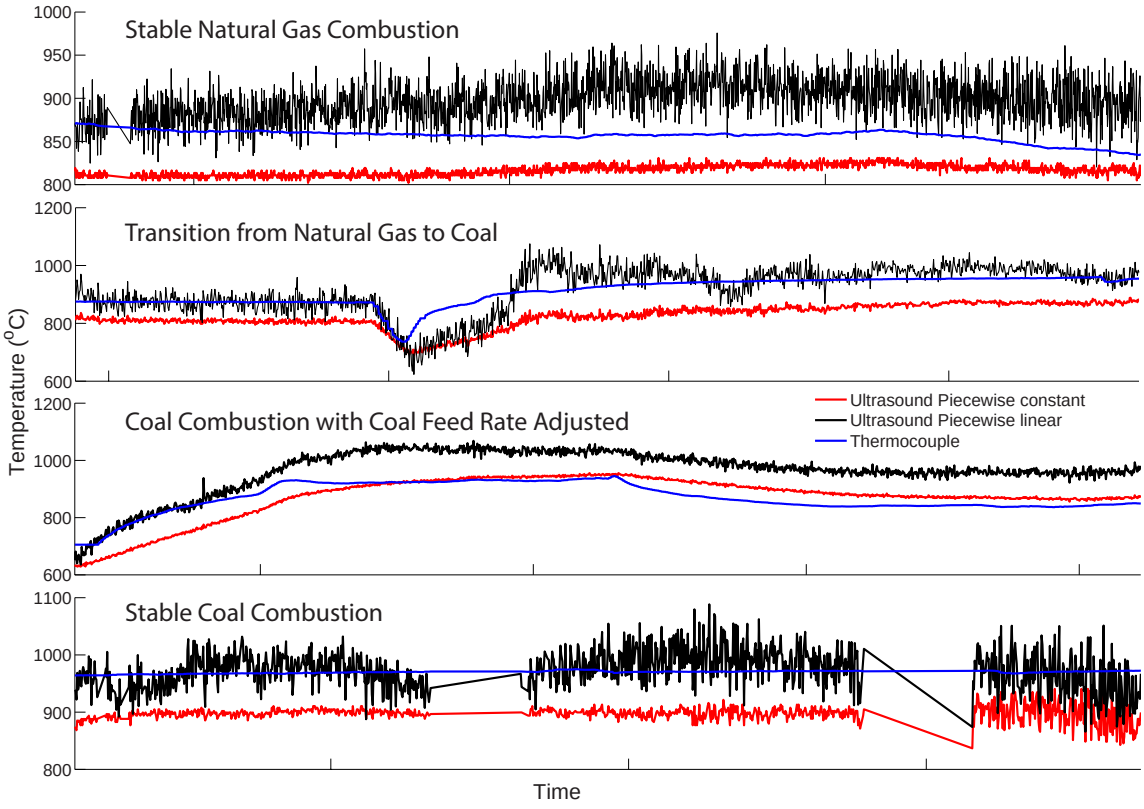

Figure 6.19: Temperature evolution at the distal end of the waveguide under different operating conditions. The thermocouple measurements were obtained at the different elevation inside the flame zone, in Port P2.

grease because of its close match of acoustic impedance to that of alumina, high viscosity, relatively slow drying/evaporation rate compared to other gels, and low sensitivity of its properties to environmental changes. Despite these attractive attributes, we found that it is still necessary to change our couplant every 2–3 hours during pilot-scale experiments. Flexible bonding agents, such as silicon rubber compounds, or rigid bonding with adhesives or epoxies, such as cyanoacrylates, may provide good ultrasound transmission (comparable with what we achieved with "wet" couplants) and a more permanent and a strong bond to the waveguide. Clearly, with all alternatives, it is important to insure that an adhesive layer does not contain voids nor air bubbles. Further studies are needed to characterize the ultrasound performance of the alternative coupling solutions and their long term stability in revelent applications.

6.5.2 Alumina Refractory Waveguide

The alumina waveguide had no visual damage after 5 days nonstop use in a high-temperature environment of OFC (Figure 6.5(K) and (L)). Only a limited ash deposit was found on its distal end and no surface corrosion was observed. At the same time, the thermocouple at the position z_4 (echogenic feature closest to the flame zone) has lost its functionality after the test. Its outer sheathing was burned, became brittle, and the inner wires were exposed with any subsequent handling.

Dispute the normal appearance of the alumina waveguide, a significant and irreversible deterioration in the strength of ultrasound echoes was revealed. This indicates that alumina experienced property changes caused by a prolonged exposure to high temperatures. We attribute this change to micro-structure changes, mainly the growth in alumina grains. Micro-structural changes due to an increase in size of grains (crystallites) in a material at high temperature is commonly seen in metals, minerals, and ceramics. This happens when recovery and recrystallization are complete and further reduction in the internal energy can only be achieved by reducing the total area of grain boundary [110].

Grain boundaries have associated macroscopic and microscopic degrees of freedom, which play an essential role in controlling the dynamic growth/depletion of grains under specific thermal conditions. Excess free energy of grain boundaries is a driving force towards the reduction in total area of grain boundaries, which drives the growth of grain sizes and the reduction of the number of grains per unit volume. Mullins [111] investigated the kinetics of the grain growth. The rate of change of the mean grain size, dr/dt, must be related to the migration rate of boundaries in the system. The mechanism for ideal grain growth and a quantitative relationship between the velocity of a grain boundary, v, and the size of the grains may be described as

$$v = \frac{dr}{dt} = M\zeta\kappa, \tag{6.1}$$

where M is grain boundary mobility, ζ is the grain boundary energy, and κ is the sum of

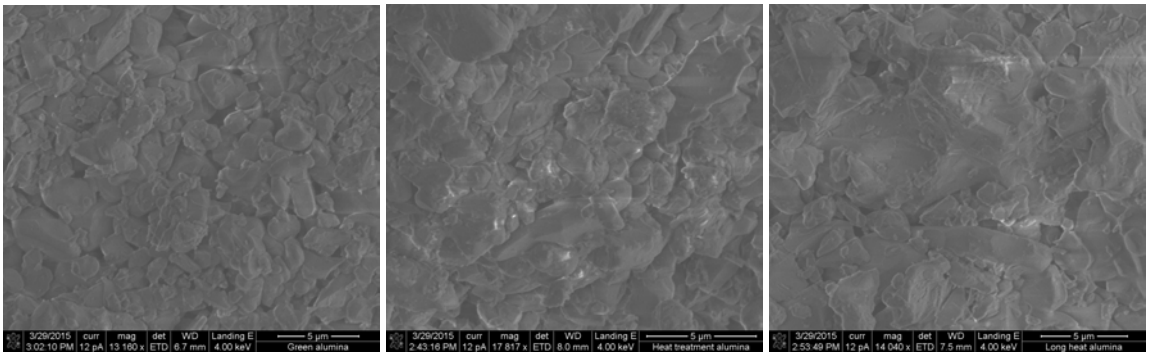

(A) No heat treatment (B) Short term heat treatment (C) Long term heat treatment

Figure 6.20: Alumina grain size distribution in the waveguide material as a function of thermal treatment is images with over 13000x magnification. (A) shows grains prior to heat treatment; the sample imaged in (B) was subjected to short term treatment; the effect of the long term exposure during pilot scale testing on the grain sizes is shown in (C).

the two principal surface curvatures of the grain. The integration of this equation gives:

$$r^2 - r_{t=0}^2 = M\zeta\kappa t, \tag{6.2}$$

where r is the final grain size and $r_{t=0}$ is the initial grain size. Grain growth is irreversible and strongly temperature dependent. High temperature environment accelerates the growth. To mitigate this process in the refractory martials that must operate at high temperature for a long time, different dopants, such as MgO, CaO, and SiO_2, are often added to stabilize the boundaries and inhibit the growth of grains.

The growth of grain sizes caused exposure to high temperature was characterized by conventional and electron microscopy. For example, SEM images shown in Figures 6.20 demonstrate the effect of the exposure to high temperatures on the grains of the alumina waveguide used by us. Figure 6.20(A) shows that green alumina (sample without thermal treatment) has a relative uniform particle size distribution, between 1 and 5 μm. After short term exposure to high temperatures of over 800 °C for less than 100 hours, the symptoms of the grain growth are observed in Figure 6.20(B), which shows a higher percentage of grains of larger sizes. Figure 6.20(C) reveals a substantial increase in grain sizes of the alumina sample heat treatment up to 1300 °C for over a thousand of hours to the point that a single grain has grown to the point of occupying almost the entire field of view.

When the mean grain diameter of our alumina ceramic waveguide increases, the inhomogeneity causes stronger scattering and absorption of ultrasonic energy and increases the attenuation of the ultrasound echoes significantly. This observation indicates that we can monitor certain mechanical properties of the refractory material and detect their changes prior to visible degradation and damage to the refractory.

Chapter 7

Conclusion

This Report summarizes the concept, the successful development, and the experimental validation of the method for ultrasound measurements of segmental temperature distribution in solids. This project solved a myriad of technical problems to make the proposed concept a reality and to successfully test the performance of this new method on a pilot scale. As a result of this project, this noninvasive method becomes a new alternative for solving a challenging problem of long-term temperature measurements in extreme environments, such as though encountered inside gasifiers, combustors, and other energy conversion processes.

Chapter 8

Products

8.1 Publications

1. Y. Jia and M. Skliar, "Ultrasound Measurements of Temperature Distribution and Heat Fluxes in Solids," submitted, 2015.

2. Y. Jia, V. Chernyshev, and M. Skliar, "Ultrasound Measurements of Segmental Temperature Distribution in Solids: Method and its High-Temperature Validation," submitted, 2015.

3. Y. Jia, A. Fry, and M. Skliar, "Pilot-Scale Demonstration of Real-Time Ultrasound Measurements of Temperature Distribution across Refractory of Oxy-Fuel Combustor," in preparation, 2015.

4. Y. Jia, "Noninvasive Ultrasound Measurments of Temperaure Distributions in Refracories of Coal and Biomass Gasifiers," PhD Thesis, Department of Chemical Engineering, University of Utah, May 2015.

5. Y. Jia and M. Skliar, "Anisotropic Diffusion Filter for Robust Timing of Ultrasound Echoes," *2014 IEEE International Ultrasonics Symposium (IUS)*, Chicago, Il, pp. 560–563, 3-6 Sept. 2014.

6. Y. Jia and M. Skliar, "Noninvasive ultrasonic measurements of temperature distribution and heat fluxes in nuclear systems," *Proc. Workshop Structural Materials for Innovative Nuclear Systems (SMINS-3)*, pp. 251–257, Idaho National Laboratory, Idaho Falls, ID, 7-10 October 2013.

7. Y. Jia, M. Puga, A. Butterfield, D. Christensen, K. Whitty, M. Skliar, "Ultrasound Measurements of Temperature Profile Across Gasifier Refractories: Method and Initial Validation," *Energy & Fuels*, **27**:4270ï£¡-4277, 2013.

8. I. Sarigul, "Model-Based Estimation of Adiabatic Flame Temperature During Coal Gasification," MS Thesis, Department of Chemical Engineering, University of Utah, September 2012.

8.2 Technology

The developed technology for noninvasive measurements of the temperature distribution in solids has a potential for a broad applicability beyond the application in gasification monitoring and control. The University of Utah has filed a patent application and was granted a patent to protect the intellectual property on the technology that has been under the development during this project. The University has also taken partial ownership in a start-up company - Clovis Point Innovations, LLC - formed to commercialize the results of our research. Other commercialization venues are also being pursued.

Bibliography

[1] C. Gault, M. Huger, J.M. Auvray, J. Soro, and E. Yeugo Fogaing. Contribution of high temperature ultrasonic measurements to investigations of thermomechanical behaviour of refractories. In *10th International Conference and Exhibition of the European Ceramic Society*, 2007.

[2] Daithí de Faoite, David J Browne, Franklin R Chang-Díaz, and Kenneth T Stanton. A review of the processing, composition, and temperature-dependent mechanical and thermal properties of dielectric technical ceramics. *Journal of Materials Science*, 47(10):4211–4235, 2012.

[3] A Wolfenden. Measurement and analysis of elastic and anelastic properties of alumina and silicon carbide. *Journal of materials science*, 32(9):2275–2282, 1997.

[4] Kyeising Kwong, Art Petty, James Bennett, Rick Krabbe, and Hugh Thomas. Wear mechanisms of chromia refractories in slagging gasifiers. *International Journal of Applied Ceramic Technology*, 4(6):503–513, 2007.

[5] Christopher Higman and Maarten van der Burgt. *Gasification*. Gulf Professional Publishing, Burlington, MA, 2nd edition, 2008.

[6] NETL Doe. Coal gasification systems, 2011.

[7] Andrew J Minchener. Coal gasification for advanced power generation. *Fuel*, 84(17):2222–2235, 2005.

[8] En-Sheng Chen. *Behavior of refractory linings for slagging gasifiers*. PhD thesis, Massachusetts Institute of Technology, 1984.

[9] Cynthia Powell Dogan, Kyei-Sing Kwong, James P Bennett, and Richard E Chinn. Improved refractories for slagging gasifiers in igcc power systems. *DOE Report*, 835687, 2003.

[10] S Chakraborty, S Sarkar, S Gupta, and A Ray. Damage monitoring of refractory wall in a generic entrained-bed slagging gasification system. *Proceedings of the Institution of Mechanical Engineers, Part A: Journal of Power and Energy*, 222(8):791–807, 2008.

[11] James P Bennett and Kyei-Sing Kwong. Failure mechanisms in high chrome oxide gasifier refractories. *Metallurgical and Materials Transactions A*, 42(4):888–904, 2011.

[12] MD Mann, WS Seames, D Shukla, X Hong, and JP Hurley. Dynamic testing of gasifier refractory, the university of north dakota. *US Department of Energy Grant*, 2005.

[13] James P Bennett, Rick Krabbe, Jasper Kwong, and Hugh Thomas. Improved temperature sensing in slagging gasifiers. In *23rd Annual Conference on Fossil Energy Materials*, May 12-14, 2009.

[14] RE Bentley. Thermocouple materials and their properties. *Theory and Practice of Thermoelectric Thermometry: Handbook of Temperature Measurement*, pages 25–81, 1998.

[15] Donald D Brooker, James S Falsetti, Allen J Pertuit, Dinh-Cuong Vuong, and James K Wolfenbarger. Gasifier monitoring apparatus, September 10 1996. US Patent 5,554,202.

[16] Qinfeng Liang, Xiaolei Guo, Zhenghua Dai, Haifeng Liu, and Xin Gong. An investigation on the heat transfer behavior and slag deposition of membrane wall in pilot-scale entrained-flow gasifier. *Fuel*, 102:491–498, 2012.

[17] BV Reddy. Fundamental heat transfer mechanism between bed-to-membrane waterwalls in circulating fluidized bed combustors. *International journal of energy research*, 27(9):813–824, 2003.

[18] Jan Taler, Piotr Duda, Bohdan Węglowski, Wiesław Zima, Sławomir Grądziel, Tomasz Sobota, and Dawid Taler. Identification of local heat flux to membrane water-walls in steam boilers. *Fuel*, 88(2):305–311, 2009.

[19] R. Guo, G. Cheng, and Y. Wang. Texaco coal gasification quality prediction by neural estimator based on dynamic pca. In *IEEE International Conference on Mechatronics and Automation*, pages 2241–2246, 2006.

[20] Ihsan Sarigul. Model-based estimation of adiabatic flame temperature during coal gasification. Master's thesis, University of Utah, 2012.

[21] J.P. Bennett and K. Kyei-Sing. Refractory liner materials used in slagging gasifiers. *Refractory Applications and News*, 9:20–25, 2004.

[22] Mark J. Hornick and John E. McDaniel. The tampa electric integrated gasification combined-cycle project, final technical report for project under cooperative agreement de-fc-21-91mc27363. Technical Report united2002tampa, United States. Department of Energy, The U.S. Department of Energy, Office of Sossil Energy, National Energy Technology Laboratory, Morganton, West Virginia, August 2002.

[23] Gregory B. Rieker, Jay B. Jeffries, and Ronald K. Hanson. Calibration-free wavelength-modulation spectroscopy for measurements of gas temperature and concentration in harsh environments. *Appl. Opt.*, 48(29):5546–5560, Oct 2009.

[24] RR Dils. High-temperature optical fiber thermometer. *Journal of Applied Physics*, 54(3):1198–1201, 1983.

[25] Byoungho Lee. Review of the present status of optical fiber sensors. *Optical Fiber Technology*, 9(2):57–79, 2003.

[26] Dan Grobnic, Christopher W Smelser, Stephen J Mihailov, and Robert B Walker. Long-term thermal stability tests at 1000 °C of silica fibre bragg gratings made with ultrafast laser radiation. *Measurement Science and Technology*, 17(5):1009, 2006.

[27] Dan Grobnic, Stephen J Mihailov, Christopher W Smelser, and Huimin Ding. Sapphire fiber bragg grating sensor made using femtosecond laser radiation for ultra-high temperature applications. *Photonics Technology Letters, IEEE*, 16(11):2505–2507, 2004.

[28] Anbo Wang, Sridhar Gollapudi, Russell G May, Kent A Murphy, and Richard O Claus. Sapphire optical fiber-based interferometer for high temperature environmental applications. *Smart Materials and Structures*, 4(2):147, 1995.

[29] Yonghang Shen, Limin Tong, Yanqi Wang, and Linhua Ye. Sapphire-fiber thermometer ranging from 20 to 1800 c. *Applied optics*, 38(7):1139–1143, 1999.

[30] Yibing Zhang, Gary R Pickrell, Bing Qi, Ahmad Safaai-Jazi, and Anbo Wang. Single-crystal sapphire-based optical high-temperature sensor for harsh environments. *Optical Engineering*, 43(1):157–164, 2004.

[31] G Pickrell, Y Zhang, and A Wang. Development of a temperature measure-ment system for use in coal gasifiers. In *19th Annual International Pittsburgh Coal Conference*, 2002.

[32] Daniel Ng and Gustave Fralick. Use of a multiwavelength pyrometer in several elevated temperature aerospace applications. *Review of Scientific Instruments*, 72(2):1522–1530, 2001.

[33] Tom Leininger. *Design, Fabrication and Testing of an Infrared Ratio Pyrometer System for the Measurement of Gasifier Reaction Chamber Temperature*. Mar 2005.

[34] Gang Lu, Yong Yan, Gerry Riley, and Harrish Chandr Bheemul. Concurrent measurement of temperature and soot concentration of pulverized coal flames. *Instrumentation and Measurement, IEEE Transactions on*, 51(5):990–995, 2002.

[35] M. Skliar, K. Whitty, and A. Butterfield. Ultrasonic temperature measurement device. *US Patent 8,801,277 B2, (2014)*, 2014.

[36] Yunlu Jia, Melissa Puga, Anthony E. Butterfield, Douglas A. Christensen, Kevin J. Whitty, and Mikhail Skliar. Ultrasound measurements of temperature profile across gasifier refractories: Method and initial validation. *Energy and Fuels*, 27(8):4270–4277, 2013.

[37] Yunlu Jia and Mikhail Skliar. Ultrasound measurements of temperature distribution and heat fluxes in solids. *submitted*, 2015.

[38] Yunlu Jia, Vasiliy Chernyshev, and Mikhail Skliar. Ultrasound measurements of segmental temperature distribution in solids: Method and its high-temperature validation. *submitted*, 2015.

[39] Yunlu Jia and Mikhail Skliar. Anisotropic diffusion filter for robust timing of ultrasound echoes. In *Ultrasonics Symposium (IUS), 2014 IEEE International*, pages 560–563. IEEE, 2014.

[40] Yunlu Jia, Andrew Fry, and Mikhail Skliar. Pilot-scale demonstration of real-time ultrasound measurements of temperature distribution across refractory of oxy-fuel combustor. *in perparation*, 2015.

[41] Moshe Rosen. Analytical ultrasonics for characterization of metallurgical microstructures and transformations. *Materials Analysis by Ultrasonics, ed. A. Vary, Noyes Data Corp., Park Ridge, New Jersey, USA*, pages 79–97, 1987.

[42] Robert E Green Jr. Ultrasonic nondestructive materials characterization. In *Analytical Ultrasonics in Materials Research and Testing*, pages 1–29. DTIC Document, 1984.

[43] Aladin Carovac, Fahrudin Smajlovic, and Dzelaludin Junuzovic. Application of ultrasound in medicine. *Acta Informatica Medica*, 19(3):168, 2011.

[44] Brian Michael Lempriere. *Ultrasound and elastic waves: frequently asked questions*. Academic Press, 2003.

[45] D. Arora, M. Skliar, and R. B. Roemer. Model-predictive control of hyperthermia treatments. *IEEE Trans. Biomed. Eng.*, 49:629–639, 2002.

[46] D. Arora, M. Skliar, and R. B. Roemer. Minimum time thermal dose control of thermal therapies. *IEEE Trans. Biomed. Eng.*, 2003, manuscript available at `http://implicit.che.utah.edu/~skliar/BME2004.pdf`. submitted.

[47] D. Arora, M. Skliar, and R.B. Roemer. Minimum-time thermal dose control of thermal therapies. *IEEE Trans. Biomed. Eng.*, 52:191–200, 2005.

[48] D. Arora, D. Cooley, T. Perry, M. Skliar, and R.B. Roemer. Direct thermal dose control of constrained focused ultrasound treatments: Phantom and *In-Vivo* evaluation. *Physics in Medicine and Biology*, 50:1919–1935, 2005.

[49] D. Arora, D. Cooley, T. Perry, J. Guo, A. Richardson, J. Moellmer, R. Hadley, D. Parker, M. Skliar, and R. B. Roemer. Mr thermometry-based feedback control of efficacy and safety in minimum-time thermal therapies: Phantom and in-vivo evaluations. *International Journal of Hyperthermia*, 22:29–42, 2006.

[50] D. Arora, M. Minor, M. Skliar, and R.B. Roemer. Control of thermal therapies with moving power deposition field. *Physics in Medicine and Biology*, 51:1201–1219, 2006.

[51] Kenneth R Erikson, Francis J Fry, and Joie P Jones. Ultrasound in medicine-a review. *Sonics and Ultrasonics, IEEE Transactions on*, 21(3):144–170, 1974.

[52] William D O'Brien. Ultrasound–biophysics mechanisms. *Progress in biophysics and molecular biology*, 93(1):212–255, 2007.

[53] Dale Ensminger. *Ultrasonics: Fundamentals, Technology, Applications, Revised and Expanded*. CRC Press, 1988.

[54] Paul A Tipler and Gene Mosca. *Physics for scientists and engineers*. Macmillan, 2008.

[55] Douglas Christensen. *Ultrasonic bioinstrumentation*. Wiley, 1988.

[56] Josef Krautkrämer and Herbert Krautkrämer. Ultrasonic testing of materials. 3. 1975.

[57] A Badidi Bouda, S Lebaili, and A Benchaala. Grain size influence on ultrasonic velocities and attenuation. *NDT & E International*, 36(1):1–5, 2003.

[58] Emmanuel P Papadakis. Grain-size distribution in metals and its influence on ultrasonic attenuation measurements. *The Journal of the Acoustical Society of America*, 33(11):1616–1621, 1961.

[59] Pascal Laugier and Guillaume Haïat. Introduction to the physics of ultrasound. In *Bone quantitative ultrasound*, pages 29–45. Springer, 2011.

[60] John William Strutt Baron Rayleigh. *The theory of sound*, volume 2. Macmillan, 1896.

[61] Jack Blitz and Geoff Simpson. *Ultrasonic methods of non-destructive testing*, volume 2. Springer Science & Business Media, 1996.

[62] Wayne R Hedrick, David L Hykes, and Dale E Starchman. *Ultrasound Physics and Instrumentation*. Elsevier Mosby, 2005.

[63] S. F. Green. An acoustic technique for rapid temperature distribution measurement. *Journal of the Acoustical Society of America*, 77(2):759 – 763, 1985.

[64] Y.J. Lee, B.T. Khuri-Yakub, and K. Saraswat. Temperature measurement in rapid thermal processing using the acoustic temperature sensor. *IEEE Trans. Semiconductor Manufacturing*, 9:115–121, 1996.

[65] RM Arthur, WL Straube, JW Trobaugh, and EG Moros. Non-invasive estimation of hyperthermia temperatures with ultrasound. *International journal of hyperthermia*, 21(6):589–600, 2005.

[66] Eugene V Malyarenko, Joseph S Heyman, H Heather Chen-Mayer, and Ronald E Tosh. High-resolution ultrasonic thermometer for radiation dosimetry. *The Journal of the Acoustical Society of America*, 124(6):3481–3490, 2008.

[67] S.F. Green. An acoustic technique for rapid temperature distribution measurements. *J. Acoustical Society of America*, 77:765–769, 1985.

[68] John Kleppe. Advances in acoustic pyrometry. *J. Acoust. Soc. Am.*, 99:2535–2574, 1996.

[69] M. Bramanti, A. Tonazzini, and A. Tonazzini. An acoustic pyrometer system for tomographic thermal imaging in power plant boilers. *Measurement Science and Technology*, 45:87–94, 1996.

[70] G. Kychakoff, A.F. Hollingshead, and S.P. Boyd. Use of acoustic temperature measurements in the cement manufacturing pyroprocess. In *Cement Industry Technical Conference*, pages 23–33, 2005.

[71] KJ Young, SN Ireland, MC Melendez-Cervates, and R Stones. On the systematic error associated with the measurement of temperature using acoustic pyrometry in combustion products of unknown mixture. *Measurement Science and Technology*, 9(1):1, 1998.

[72] S Takahashi J Lu, K Wakai and S Shimizu. Acoustic computer tomographic pyrometry for two-dimensional measurement of gases taking into account the effect of refraction of sound wave paths. *Measurement Science and Technology*, 11(6):692 – 697, 2000.

[73] Andrew Forbes. Acoustic monitoring of global ocean climate. *Sea Technology; (United States)*, 35(5), 1994.

[74] Krishnan Balasubramaniam, Vimal V Shah, R Daniel Costley, Gary Boudreaux, and Jagdish P Singh. High temperature ultrasonic sensor for the simultaneous measurement of viscosity and temperature of melts. *Review of scientific Instruments*, 70(12):4618–4623, 1999.

[75] R.M. Arthur, J.V. Trobaugh, W.L. Straube, and E.G. Moros. Temperature dependence of ultrasonic backscattered energy in motion compensated images. *IEEE Trans. Ultrasonics, Ferroelectric and Frequency Control*, 52:1644–1652, 2005.

[76] Claudio Simon, Philip VanBaren, and Emad S Ebbini. Two-dimensional temperature estimation using diagnostic ultrasound. *Ultrasonics, Ferroelectrics, and Frequency Control, IEEE Transactions on*, 45(4):1088–1099, 1998.

[77] Manabu Takahashi and Ikuo Ihara. Ultrasonic determination of temperature distribution in thick plates during single sided heating. *Modern Physics Letters B*, 22(11):971–976, 2008.

[78] P. L. Schmidt, D. G. Walker, D. J. Yuhas, and M. M. Mutton. Thermal measurements using ultrasonic acoustical pyrometry. *Ultrasonics*, 54(4):1029–1036, 2014.

[79] Bernhard Praher, Klaus Straka, and Georg Steinbichler. An ultrasound-based system for temperature distribution measurements in injection moulding: system design, simulations and off-line test measurements in water. *Measurement Science and Technology*, 24(8):084004, 2013.

[80] H. Zhang, M. Basin, and M. Skliar. Itó-volterra optimal state estimation with continuous, multirate, randomly sampled, and delayed measurements. *IEEE Trans. Automat. Control*, 52:401–416, 2007.

[81] R.K. Ramalingam and H. Neumann. Fiber bragg grating-based temperature distribution evaluation of multilayer insulations between 300 k-77 k. *Sensors Journal, IEEE*, 11(4):1095–1100, April 2011.

[82] Paul A Hanscombe and Paul N Richards. Distributed temperature sensor, February 15 1994. US Patent 5,286,109.

[83] DR Hull, HE Kautz, and A Vary. Measurement of ultrasonic velocity using phase-slope and cross-correlation methods. *Materials evaluation*, 43(11):1455–1460, 1985.

[84] C.L. de Korte, A.F.W. van der Steen, B.H.J. Dijkman, and C.T. LancÃľe. Performance of time delay estimation methods for small time shifts in ultrasonic signals. *Ultrasonics*, 35(4):263 – 274, 1997.

[85] G. Jacovitti and G. Scarano. Discrete time techniques for time delay estimation. *IEEE Transactions on Signal Processing*, 41(2):525–533, Feb 1993.

[86] M. Parrilla, J. J. Anaya, and C. Fritsch. Digital signal processing techniques for high accuracy ultrasonic range measurements. *IEEE Transactions on Instrumentation and Measurements*, 40(4):759–763, 1991.

[87] F. Viola and W.F. Walker. A comparison of the performance of time-delay estimators in medical ultrasound. *IEEE Transactions on Ultrasonics, Ferroelectrics, and Frequency Control*, 50(4):392–401, April 2003.

[88] B. Champagne, E. Eizenman, and S. Pasupathy. Exact maximum likelihood time delay estimation for short observation intervals. *IEEE Transactions on Signal Processing*, 39(6):1245–1257, Jun 1991.

[89] L H Le. An investigation of pulse-timing techniques for broadband ultrasonic velocity determination in cancellous bone: a simulation study. *Physics in Medicine and Biology*, 43(8):2295 – 2308, 1998.

[90] Raymond Edwin Brennan. *Ultrasonic nondestructive evaluation of armor ceramics*. ProQuest, 2007.

[91] Avadh Behari Bhatia. *Ultrasonic absorption*. Clarendon Press, 1967.

[92] Andrew Richard Portune. *Nondestructive ultrasonic characterization of armor grade silicon carbide*. 2011.

[93] H. Baudson, F. Debucquoy, M. Huger, C. Gault, and M. Rigaud. Ultrasonic measurement of young's modulus mgo/c refractories at high temperature. *IEEE Trans. Ultrasonics, Ferroelectric and Frequency Control*, 19:1895–1901, 1999.

[94] Joern Werner, Christos G Aneziris, and Steffen Dudczig. Young's modulus of elasticity of carbon-bonded alumina materials up to 1450 °C. *Journal of the American Ceramic Society*, 96(9):2958–2965, 2013.

[95] J Kováčik. Correlation between young's modulus and porosity in porous materials. *Journal of materials science letters*, 18(13):1007–1010, 1999.

[96] G. Baskaran, Krishnan Balasubramaniam, and C. Lakshmana Rao. Shear-wave time of flight diffraction (s-tofd) technique. *NDT & E International*, 39(6):458 – 467, 2006.

[97] Ajay Raghavan and Carlos ES Cesnik. Review of guided-wave structural health monitoring. *Shock and Vibration Digest*, 39(2):91–116, 2007.

[98] J.C. Jackson, R. Summan, G.I Dobie, S.M. Whiteley, S.G. Pierce, and G. Hayward. Time-of-flight measurement techniques for airborne ultrasonic ranging. *Ultrasonics, Ferroelectrics, and Frequency Control, IEEE Transactions on*, 60(2):343–355, February 2013.

[99] MarÃŋa JesÃžs MartÃŋnez Bueno, Ana AgÃijera, MarÃŋa JosÃľ GÃşmez, MarÃŋa Dolores Hernando, Juan Francisco GarcÃŋa-Reyes, and Amadeo R. FernÃąndez-Alba. Application of liquid chromatography/quadrupole-linear ion

trap mass spectrometry and time-of-flight mass spectrometry to the determination of pharmaceuticals and related contaminants in wastewater. *Analytical Chemistry*, 79(24):9372–9384, 2007.

[100] Cuiping Li, Lianjie Huang, Nebojsa Duric, Haijiang Zhang, and Charlotte Rowe. An improved automatic time-of-flight picker for medical ultrasound tomography. *Ultrasonics*, 49(1):61–72, 2009.

[101] SQ Van Veen, ECJ Claas, and Ed J Kuijper. High-throughput identification of bacteria and yeast by matrix-assisted laser desorption ionization-time of flight mass spectrometry in conventional medical microbiology laboratories. *Journal of clinical microbiology*, 48(3):900–907, 2010.

[102] Arminas Ragauskas, Gediminas Daubaris, Vytautas Ragaisis, and Vytautas Petkus. Implementation of non-invasive brain physiological monitoring concepts. *Medical Engineering & Physics*, 25(8):667 – 678, 2003. Cerebrovascular Modelling.

[103] R. El Guerjouma, A Mouchtachi, Y. Jayet, and J.C. Baboux. Nondestructive evaluation of graphite by ultrasonic velocity measurement using cross-correlation and hilbert transform methods. In *Proceedings of IEEE Ultrasonics Symposium*, pages 829–832 vol.2, Oct 1992.

[104] P. Perona and J. Malik. Scale-space and edge detection using anisotropic diffusion. *IEEE Transactions on Pattern Analysis and Machine Intelligence*, 12(7):629–639, Jul 1990.

[105] G.W. Wei. Generalized perona-malik equation for image restoration. *IEEE Signal Processing Letters*, 6(7):165–167, July 1999.

[106] M.J. Black, G. Sapiro, D.H. Marimont, and D. Heeger. Robust anisotropic diffusion. *IEEE Transactions on Image Processing*, 7(3):421–432, Mar 1998.

[107] Chourmouzios Tsiotsios and Maria Petrou. On the choice of the parameters for anisotropic diffusion in image processing. *Pattern recognition*, 46(5):1369–1381, 2013.

[108] Mohammad Arafat Hussain, S. Kaisar Alam, Soo Yeol Lee, and Md. Kamrul Hasan. Robust strain-estimation algorithm using combined radiofrequency and envelope cross-correlation with diffusion filtering. *Ultrasonic Imaging*, 34(2):93–109, 2012.

[109] G. Gerig, O. Kubler, R. Kikinis, and F.A Jolesz. Nonlinear anisotropic filtering of mri data. *IEEE Transactions on Medical Imaging*, 11(2):221–232, Jun 1992.

[110] Anthony Rollett, FJ Humphreys, Gregory S Rohrer, and M Hatherly. *Recrystallization and related annealing phenomena*. Elsevier, 2004.

[111] WW Mullins. The statistical self-similarity hypothesis in grain growth and particle coarsening. *Journal of Applied Physics*, 59(4):1341–1349, 1986.